

NANOMATERIALS: SYNTHESIS, CHARACTERIZATION, AND THEIR BIO-INTEGRATION

Name: Travis L. Jennings

Department: Department of Chemistry and Biochemistry

Major Professor: Geoffrey Strouse

Degree: Doctor of Philosophy

Term Degree Awarded: Spring, 2006

The purpose of this dissertation is to utilize the changing optical and electronic properties of metallic and semiconductor nanomaterials for applications to biotechnology. The dynamic optical properties of metals and semiconductors with size is discussed in regard to the ability of these materials to accept electronic excitation energy from classical molecular fluorescent dyes (Chap. 2). Absorption, photoluminescence, and time-resolved photoluminescence experiments are performed on metal nanoparticle-dye pairs at separation distances controlled via synthetic DNA spacers where the distance, dye, and nanoparticle size are varied (Chaps. 3 and 4). It is found that the efficiency of energy transfer to small metal nanoparticles is greater than expected for a $1/R^6$ Förster mechanism of energy transfer and the measurable separation distance is increased, following a $1/R^4$ dependence. The $1/R^4$ distance dependence is the theoretically established relationship of an excited molecule to a metallic surface. This tool, termed “Nanometal Surface Energy Transfer” (NSET) is then used in Chapters 5 and 6 to measure the kinetics and conformational changes associated with a hammerhead ribozyme as a model test subject for NSET methodology. Finally, ZnS-overcoated CdSe semiconductor

quantum dots, (Chap. 7) are synthesized controllably and characterized in terms of their potential for biological incorporation for detection or *in vitro* studies.

THE FLORIDA STATE UNIVERSITY

COLLEGE OF ARTS AND SCIENCES

NANOMATERIALS: SYNTHESIS, CHARACTERIZATION, AND THEIR
BIO-INTEGRATION

By

TRAVIS L. JENNINGS

A Dissertation submitted to the
Department of Chemistry and Biochemistry
in partial fulfillment of the
requirements for the degree of
Doctor of Philosophy

Degree Awarded:
Spring Semester, 2006

The members of the Committee approve the Dissertation of Travis L. Jennings defended on Jan. 18, 2006.

Geoffrey Strouse
Professor Directing Dissertation

Bryant Chase
Outside Committee Member

Michael Kasha
Committee Member

Harry W. Kroto
Committee Member

Approved:

Professor Naresh Dalal, Chair
Department of Chemistry and Biochemistry

Professor Joseph Travis, Dean, College of Arts and Sciences

The Office of Graduate Studies has verified and approved the above named committee members.

The members of the Committee approve the Dissertation of Travis L. Jennings defended on Jan. 18, 2006.

Geoffrey Strouse
Professor Directing Dissertation

Bryant Chase
Outside Committee Member

Michael Kasha
Committee Member

Harry W. Kroto
Committee Member

The Office of Graduate Studies has verified and approved the above named committee members.

To my beautiful, talented and sassy wife, Miki Watanabe Jennings.

ACKNOWLEDGEMENTS

I'd like to thank my research advisor, Geoff Strouse for all of the time, effort, grit (not to be confused with grits), and whiskey that he put into me. A lesser advisor may have given up, but his persistent pressure on me to break beyond my current abilities has made me the scientist that I am today. (That may not be saying much, but you should have seen me when I started...)

I would also like to thank the following people:

- My Mother, without whose support I would not have been able to finish even the first year of my graduate studies
- My wonderful wife who gave me good reason to leave the lab every night
- My entire family for all of their support: Mom, Dad, Shannon, Juan, Ashlyn, Kathleen, Sabir, and Trent
- Dr. Donna Speckman, Steve LaLumondiere, and Dr. Steve Moss from The Aerospace Corp. for investing so much time and energy in me
- My wonderful pets, Brian and Martini
- Donny Magaña for knowing everything and trying hard to diffuse that knowledge
- Jeff Gerbec, and Greg Khitrov for your sharp humor
- Mani Singh for working *very* hard and *very* diligently
- Gary Braun for teaching me graphics, web, and science
- Jörg Schlatterer for teaching me biochemistry, efficiency, and cleanliness

- Dr. Khalid Hanif for his help with XPS and pXRD
- Aaron Washington for replacing the void in my heart when Khalid left
- Dan Neuman for showing me around the big cities during various seminars
- Alan Alovus and Sine for juggling, good times, and excellent friendship
- Artjay Javier for all of your help
- and all those who helped me keep a sense of humor.

— Travis

TABLE OF CONTENTS

List of Tables	ix
List of Figures	x
List of Abbreviations	xiii
Abstract	xiv
1. GENERAL INTRODUCTION	1
2. THEORY OF ENERGY TRANSFER TO METALS	8
2.1 Introduction	8
2.2 Photophysical Nature of Organic Dyes	8
2.3 Electronic and Optical Properties of Metallic Nanocrystals	12
2.4 Energy Transfer to Metal Surfaces	21
3. NSET VS DISTANCE TO d=1.5 NANOPARTICLES	27
3.1 Introduction	27
3.2 Experimental	29
3.2.1 Nanoparticle Synthesis	29
3.2.2 dsDNA - Nanoparticle Coupling	29
3.2.3 Absorption/Photoluminescence	30
3.2.4 Lifetime Measurements	31
3.3 Results	31
3.3.1 Lifetimes of Dyes Near 1.5 nm NP's	33
3.3.2 Photoluminescence Characterization	33
3.3.3 Absorption Characterization	36
3.4 Discussion	37
3.4.1 Development of the Model	37
3.4.2 Monitoring k_r	43
3.5 Conclusion	44
4. NSET AS A FUNCTION OF NANOPARTICLE SIZE	46
4.1 Introduction	46
4.2 Experimental	48
4.2.1 Au ₆ Nanoparticle Synthesis	48

4.2.2	dsDNA - Nanoparticle Coupling:	52
4.2.3	Absorption/Photoluminescence:	53
4.2.4	Lifetime Measurements:	53
4.3	Results and Discussion	54
4.3.1	Degree of Labeling for DNA to Au ₆	54
4.3.2	Comparison to SERS	56
4.3.3	Monitoring Absorption of dyes near Au ₆	58
4.3.4	Photoluminescence and Lifetimes of Dyes Near Au ₆	60
4.4	Conclusion	72
5.	NSET ANALYSIS OF HAMMERHEAD CATALYSIS	73
5.1	Single-Dye Hammerhead Introduction	73
5.2	Experimental	75
5.2.1	Binding of NanoGold and Preparation of the Hammerhead Complex	75
5.2.2	PAGE Analysis of NG - Hammerhead Ribozyme	76
5.2.3	Correlated Optical / PAGE Analysis of NG-Rib	76
5.3	Results and Discussion	77
5.3.1	Formation of the Hammerhead Complex (NG-HHComp).	77
5.3.2	NSET-based Structural Characterization	80
5.3.3	Optical Tracking of Ribozyme Cleavage	83
5.3.4	Ribozyme-Substrate Binding and Cleavage: E-S Stability	86
5.4	Conclusions	94
6.	DUAL DYE HAMMERHEAD NSET TRIANGULATION	95
6.1	Introduction	95
6.2	Experimental	97
6.3	Results and Discussion	100
6.3.1	Analysis of Stems I and III	102
6.3.2	Analysis of Stems II and III	106
6.3.3	Analysis of Stems I and II	106
6.4	Discussion and Conclusions	109
7.	SEMICONDUCTOR NANOPARTICLES: SYNTHESIS AND CHARACTERIZATION	112
7.1	Introduction	112
7.2	Experimental	113
7.2.1	Synthesis of Core CdSe/HDA	113
7.2.2	ZnS-Capping of Core CdSe QD's	113
7.2.3	Water Solubilization: Thiocholine Ligand Exchange	117
7.2.4	Measurements and Characterization	117
7.3	Results and Discussion	118
7.3.1	Absorption, Photoluminescence, and Quantum Yields	118
7.3.2	Surface and Structural Analysis	121
7.3.3	Luminescence Lifetimes of CdSe/ZnS	125

7.3.4 Water-solubilization and Effects on Photoluminescence	127
7.4 Conclusions	129
A. Gold Absorption Calculations	130
B. CPS - Kuhn Model d_0 Calculations	134
C. J-Overlap Integral and FRET R_0 Calculations	137
D. Dye Laser Alignment	140
E. Streak Camera Operation	146
BIOGRAPHICAL SKETCH	160

LIST OF TABLES

3.1	Table of PL quenching, lifetime quenching, and both the calculated and theoretical radiative rates for FAM and Cy5	39
4.1	Efficiency of coupling for dsDNA-dye to Au ₆	56
4.2	Measured values for the lifetimes of FAM, TAMRA and Cy5 dyes at variable separation distances from a 6 nm gold NP surface.	67
5.1	Measured binding and cleavage rates for the single-dye Hammerhead Complex	93
6.1	Tabulated lifetimes, rates of energy transfer, quenching efficiencies, and distances for Cy3 and AF647	103

LIST OF FIGURES

1.1	Absorption spectra of CdSe QD's as a function of size	3
1.2	Various size gold nanoparticle TEM and absorption spectra	5
2.1	Description of energy splitting from atomic to band structures	13
2.2	Absorption data for d=1.4, 1.5, and 6nm gold NPs	16
2.3	Dielectric constants of Gold as a function of optical energy	19
2.4	Theoretically generated Gold extinction spectra	20
2.5	Orientation dependence of a molecular dipole above a conducting surface. . .	23
3.1	Scheme of DNA binding to a 1.5 nm Au Nanoparticle	32
3.2	Lifetimes for FAM and Cy5 near 1.5 nm NP's	34
3.3	cw-Photoluminescence quenching for FAM and Cy5 dyes	35
3.4	Absorption spectra for dye-DNA appended to 1.5 nm NP's	36
3.5	Illustration of a NP interacting with the electric field induced from a nearby dipole	38
3.6	Overlaid quenching data and theoretical plot for FAM and Cy5	40
3.7	Corrected and normalized absorption spectra for dye-DNA appended to NP's	45
4.1	Illustration of 45mer DNA appended to 1.5, 6.0, and 13 nm Gold NP's . . .	47
4.2	Effect of NP Size on Cone Angle swept out by a point dipole	49
4.3	TEM image of 6nm Au Nanoparticles	51
4.4	Experimental absorptions of dye-labeled dsDNA bound to 6 nm Au NP's . .	55
4.5	Subtracted and normalized absorption spectra for dye-dsDNA-Au ₆	59
4.6	Photoluminescence efficiency of dyes at discrete distance from Au ₆	62

4.7	Luminescent lifetimes of FAM at discrete separation distances from Au ₆ . . .	63
4.8	Luminescent lifetimes of Cy5 at discrete separation distances from Au ₆ . . .	64
4.9	Quenching efficiency curve for FAM and Cy5 as a function of distance to Au ₆	69
4.10	Illustration of distance effects from C ₆ -flexibility for 6 nm vs 1.5 nm NP. . .	71
5.1	3-Dimensional scheme of a single-dye NG-bound Hammerhead Ribozyme . .	74
5.2	Denaturing PAGE showing NG-coupling to Hammerhead ribozyme	78
5.3	Nondenaturing PAGE demonstrating NG-Rib complex formation and activity	79
5.4	Structural changes of single-dye Hammerhead ribozyme displayed by NSET molecular ruler	82
5.5	Scheme of NG-Rib cleavage reaction with a substrate strand of RNA	84
5.6	Hammerhead ribozyme kinetic reaction pathway	85
5.7	Denaturing PAGE and Photoluminescent data correlating NG-Rib cleavage activity to the molecular beacon approach	87
5.8	Binding Rate Constant for single-dye Hammerhead Ribozyme	89
5.9	Cleavage Rate constant fitting for single-dye Hammerhead Ribozyme	90
5.10	Native PAGE kinetics for a hammerhead ribozyme, discrimination of different conformations	92
6.1	Triangulation scheme of a 1.5 nm NP and two dyes appended to a hammerhead ribozyme	96
6.2	Donor emission and Acceptor absorption spectra for FRET-NSET hammer- head system	101
6.3	Alternate configuration scheme for ribozyme-substrate giving rise to a differ- ent separation distance	104
6.4	Scheme of Cy3-NSET with experimental lifetimes for a single-label hammer- head	105
6.5	Cy3 lifetimes being quenched by AF647 in a FRET mechanism	107
6.6	Quenched lifetimes and suggested model for AF647 energy transfer to NP on dual labeled hammerhead	108
6.7	Illustration of a dual dye-labeled hammerhead ribozyme with measured dis- tances between stems I, II, and III	110

7.1	Absorption spectra of 6 CdSe core samples grown identically in an Aluminum block.	114
7.2	TEM pictures of CdSe and CdSe/ZnS QD's with varying shell thickness. . .	116
7.3	Absorption, PL, QY's and Stokes shifts as a function of ZnS thickness	119
7.4	XPS analysis on different thickness CdSe/ZnS Nanomaterials	122
7.5	pXRD structure analysis of CdSe/ZnS capped QD's as a function of shell thickness	124
7.6	Luminescence lifetimes of CdSe QD's vs ZnS thickness	126
7.7	Absorption and Photoluminescence of H ₂ O-soluble thiocholine CdSe/ZnS . .	128

List of Abbreviations

· Au ₆	6 nm Gold Nanoparticle
· dsDNA	double-stranded DNA
· FWHM	Full-Width Half-Max
· GN	Gersten-Nitzan
· HDA	hexadecylamine
· ML	MonoLayers
· NG	NanoGold
· NG-Rib	NanoGold-Ribozyme
· NP	Nanoparticle
· PBS	Phosphate Buffer Saline
· PL	Photoluminescence
· pXRD	powder X-Ray Diffraction
· SERS	Surface Enhanced Raman Scattering
· STE	Self-Trapped Exciton
· SPR	Surface Plasmon Resonance
· TIR	Total Internal Reflection
· TEM	Transmission Electron Microscopy
· TOP	TriOctylPhosphine
· QD	Quantum Dot
· XPS	X-Ray Photoelectron Spectroscopy

ABSTRACT

The purpose of this dissertation is to utilize the changing optical and electronic properties of metallic and semiconductor nanomaterials for applications to biotechnology. The dynamic optical properties of metals and semiconductors with size is discussed in regard to the ability of these materials to accept electronic excitation energy from classical molecular fluorescent dyes (Chap. 2). Absorption, photoluminescence, and time-resolved photoluminescence experiments are performed on metal nanoparticle-dye pairs at separation distances controlled via synthetic DNA spacers where the distance, dye, and nanoparticle size are varied (Chaps. 3 and 4). It is found that the efficiency of energy transfer to small metal nanoparticles is greater than expected for a $1/R^6$ Förster mechanism of energy transfer and the measurable separation distance is increased, following a $1/R^4$ dependence. The $1/R^4$ distance dependence is the theoretically established relationship of an excited molecule to a metallic surface. This tool, termed “Nanometal Surface Energy Transfer” (NSET) is then used in Chapters 5 and 6 to measure the kinetics and conformational changes associated with a hammerhead ribozyme as a model test subject for NSET methodology. Finally, ZnS-overcoated CdSe semiconductor quantum dots, (Chap. 7) are synthesized controllably and characterized in terms of their potential for biological incorporation for detection or *in vitro* studies.

CHAPTER 1

GENERAL INTRODUCTION

The past couple of decades of materials research have seen an amplified interest in the nanoscience fields, rising to levels so loud that the outside world and even popular culture have begun to embrace these new initiatives in science. “Nano” is arguably a household word by this point in time, made popular by books such as “Prey” by Michael Crichton or “NANO” by John Robert Marlow or even the sleek new “Ipod Nano” mp3 music player recently released by Apple Computers. The word “nano” can be found on the lips of young and old, although it is doubtful that all who use it understand its meaning. “Nano”, of course, means 10^{-9} . It is an order of magnitude that apparently has the world and many fields of scientific research abuzz with excitement. What is the significance? Why would an order of magnitude, a number, cause the heart of a scientist to palpitate or the eyes of a businessman to turn green? The number has always been there, it is not a new number - but it must have attained some new meaning. The answer to this question is described in the word, “potential”.

Potential is defined as the inherent capacity for coming into being, which means the materialization of assets to the more business-inclined, or conserved energy in the mind of a scientist. In 1926, Erwin Schrödinger developed the famous “time-independent Schrödinger equation” and published his ideas on quantum mechanics via⁵ differential equations. Pictographically, placing a quantum mechanical particle in a confined box with infinite potential at the walls allows one to solve Schrödinger’s time-independent equation for the energy levels of the system. This “Particle-in-a-Box” model can be applied to certain well-behaved conjugated dye molecules like the cyanine dye series and is the best model to describe the observations of semiconductor nanomaterials (“quantum dots” - QD’s). Quantum dots are semiconductor materials on the scale of 10^{-9} m in diameter. They are the incarnation of

the particle-in-a-box model where, if the host-lattice boundaries are smaller than the Bohr radius of the bulk material bound-exciton, the wavefunction may be restricted physically inside a volume by the high-energy potential walls.

Louis Brus has solved the Schrödinger equation for the lowest excited state of a particle in a sphere, using the Wannier Hamiltonian for direct gap semiconductors to give the energy as a function of particle radius, R :[\(1\)](#)

$$E \approx \frac{\hbar^2 \pi^2}{2R^2} \left[\frac{1}{m_e} + \frac{1}{m_h} \right] - \frac{1.8e^2}{\epsilon_2 R} + \frac{e^2}{R} + \text{higher order terms} \quad (1.1)$$

where m_e is the mass of the electron, m_h is the mass of the hole, ϵ_2 is the dielectric coefficient for the semiconductor material. Equation [1.1](#) calculates the band gap energy required to create an exciton in a direct-gap semiconductor quantum dot as a function of QD radius. The band gap, by definition, is the energy required to create an electron and a hole at rest with respect to the host lattice, and so the energy calculated here should show an inverse relation to the lowest energy absorption state as the QD increases with size. Figure [1.1](#) shows absorption spectra and luminescence phenomena for a variety of sizes of CdSe QD's where the lowest energy absorbing state shifts to lower energy as the crystallite size increases. This is in direct support of Eqn. [1.1](#) and the Particle-in-a-Box model where the energy of the system increases as the length of the box decreases and vice versa.

These nanomaterials are not limited to the semiconductor variety, however, but indeed any material which can be synthesized on the nanometer scale may exhibit dynamic properties that depend on size such as magnetic materials,[\(2; 3\)](#) metal nanoparticles, and SiO₂.[\(4; 5\)](#) The surfaces of nanoparticles may be functionalized to render them soluble in almost any reasonable solvent as well as confer upon them affinity for a specific biological interaction. For this very reason, many researchers have become greatly interested in applying the unique properties inherent with nanomaterials to medical diagnostics, cancer targeting,[\(6; 7\)](#) or “magnetofection” (delivery of genetic vectors to cells by association with magnetic nanoparticles.)[\(8\)](#) But these last statements beg the question: “Why does anyone care to integrate nanomaterials with biology or medicine? What possible good can come of such a twisting of nature?!” A recent article in Science suggests that:[\(9\)](#)

“Nanotechnology’s ability to shape matter on the scale of molecules is opening the door to a new generation of diagnostics, imaging agents, and drugs for

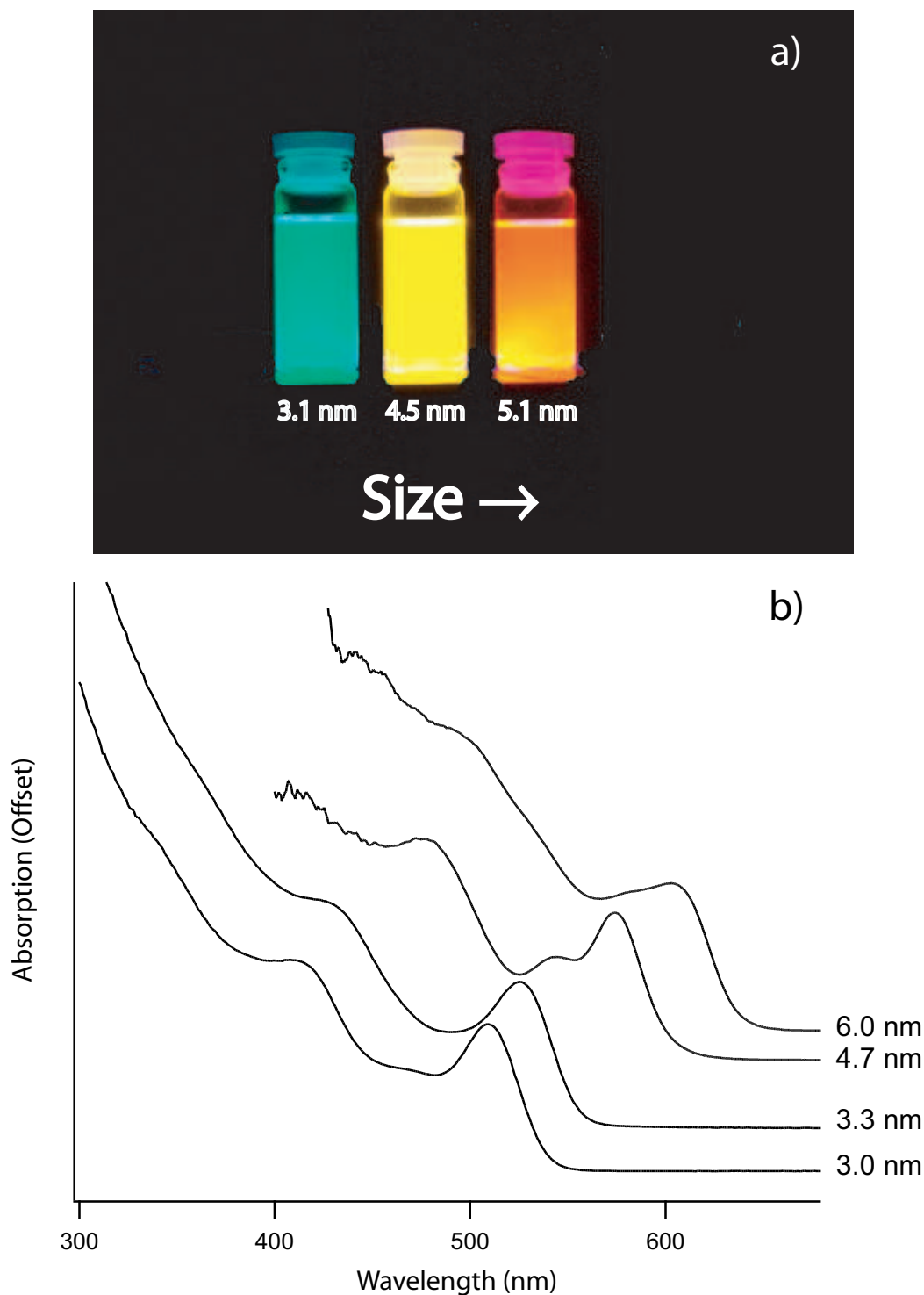


Figure 1.1: a) Luminescence of three different sizes of CdSe QD's under UV excitation showing the affect of quantum dot size upon optical emission. b) Absorption spectra for a variety of CdSe semiconductor quantum dots where the lowest energy absorptive state depends upon the size of the crystallite. The smallest sizes (3.0 nm shown above) absorb the highest in energy, and the larger sizes decrease the energy of the first excitonic state.

detecting and treating cancer at its earliest stages. But perhaps more important, it is enabling researchers to combine advances, creating nanosized particles that contain drugs designed to kill tumors, targeting compounds designed to home in on malignancies, and imaging agents designed to light up even the earliest stage cancers.”

These sentiments imply the optimistic view held by many that nanomaterials could hold enormous potential for the detection and treatment of different diseases. However, just as abundant as this hope, is a great fear of the unknown. Because nanoparticles are novel, and new varieties with different heavy metals are being synthesized every day, there is a well-founded concern that many nanoparticles may be too toxic to ever be injected into a human body. Indeed, the toxicity of certain nanoparticles is of deep concern to the advancement of most semiconductor nanoparticles into live organisms for *in vivo* diagnostics and has become a very real obstacle(9; 10; 11) for advancement in the medicinal fields. This is a “golden” opportunity for metallic nanoparticles to step up and demonstrate their advantages.

Elemental gold is non-toxic due to its low reactivity but is also (mostly) non-luminescent, which means that fluorescence marker applications are out of the question. However, gold particles may be embedded with magnetic ions such as Co, Ni, or Fe to give them magnetic properties and the potential for such uses as “magnetofection” or contrast agents for MRI scanning. This said, by functionalizing the nanoparticle surface with molecules meant for specific binding interactions, single-stranded nucleotides searching for a complement or an antibody searching for an antigen for example, the nanoparticle may be site-specifically directed within the system under study. The nanoparticle could then act as a probe or beacon to the outside world, confessing the position of some offending organ or cancerous tumor within the body. This is the ultimate goal of much nano-biomedical science as it stands today, however basic science must come first as we build toward the more complex issues.

The most basic question we can ask when appending a nanoparticle to a bio-molecule bound for a specific destination is, will that molecule still look and behave like the native molecule? Will it take my nanoparticle along with it and perform its duty, all the while ignoring the fact that it is carrying extra baggage? Also, what property of the nanoparticle can I use to detect a binding event to the appended bio-molecule? As described for

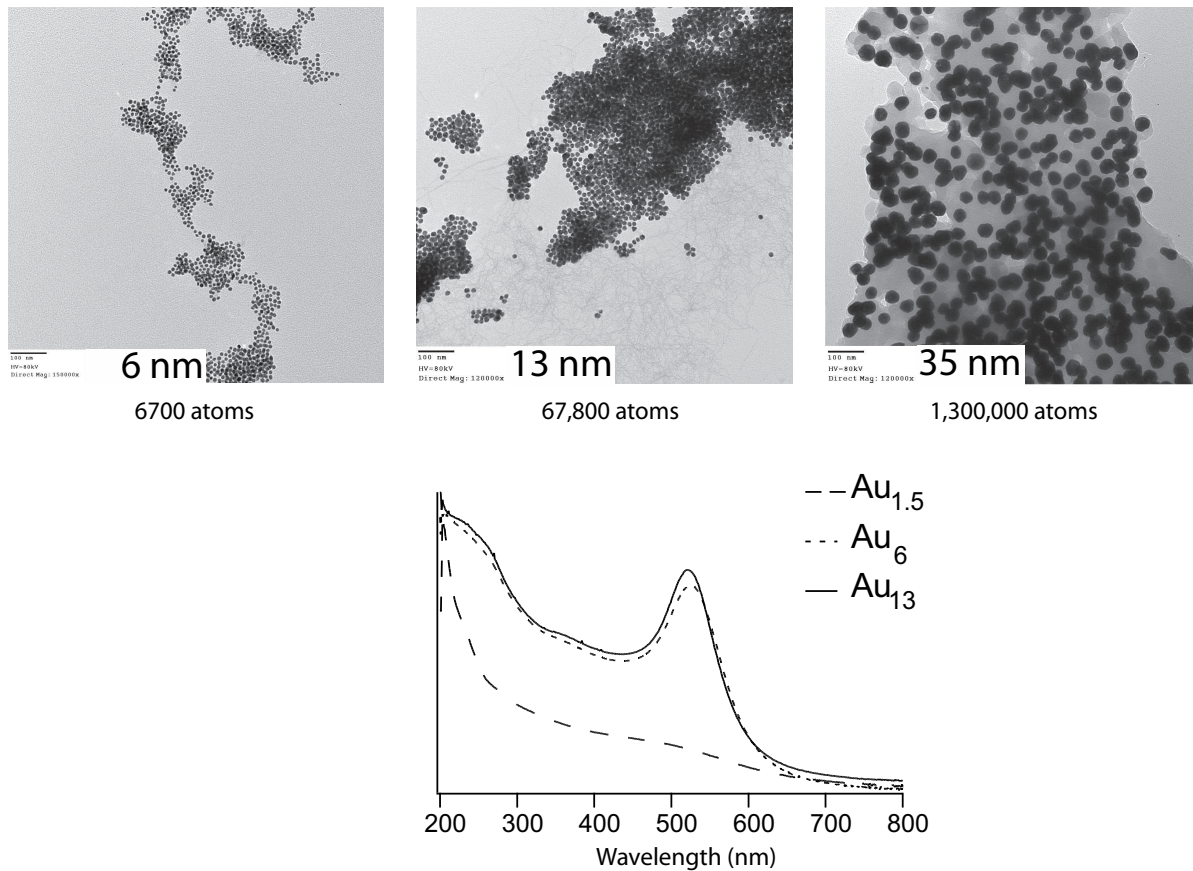


Figure 1.2: *TOP*: TEM images of various sized gold nanoparticles grown by citrate / tannic acid reduction of auric acid. The particles are spherical with good monodispersity. The number of atoms within the volume of a sphere increases with the particle radius r^3 and has a pronounced effect on the electronic and optical properties of the ensemble in solution. The absorption spectra (*BOTTOM*) shows that there is relatively little difference in the absorption properties (besides extinction coefficient) between the 6 nm and 13 nm particles, but that a drop from 6 to 1.5 nm yields a drastic change in the optical properties. This change is a result of dynamic dielectric constants of gold as a function of size.

semiconductor materials earlier, the optical and electronic properties of metal nanoparticles also demonstrate a size dependence, this time due to a decreasing density of free electrons at smaller sizes.^(12; 13) Figure 1.2 shows three separate transmission electron microscope (TEM) images of 6 nm, 13 nm, and 35 nm gold particles. All of these particles have similar absorption behavior throughout the visible, where the absorption spectra of the 6 and 13 nm particles are shown below. The absorption of spectrum of a solution containing dispersed 1.5 nm diameter particles, however, suggests a drastically changed relationship for these small sizes. The disappearance of the absorption band centered at ~ 525 nm is indicative of one size effect for metal nanoparticles, where the changing absorption may be explained by a reduced density of free electrons as the particles begin to approach the cluster regime.

Depending upon the property of the nanomaterial being utilized in a certain method (magnetic, optical, conductive), a well-controlled nanoparticle size may be conducive to the success of such a study. To this end, it is the purpose of this dissertation, and of the research I've conducted, to focus on the integration of nanoparticles with biological molecules in the hopes of standardizing a method for optical characterization of simple molecule-molecule interactions and conformational changes. I attempt to take advantage of the controlled synthesis of 1.5 nm diameter gold nanoparticles for their minimally-invasive integration into different nucleic acid systems and their electronic properties when interacting with a nearby excited-state electronic dipole. In a Förster resonance energy transfer (FRET) - style manner, the pairing of a fluorescent molecule with a metal nanoparticle can be used as either a molecular beacon or as a ruler to calculate separation distances. However, this technique may have many advantages over the FRET predecessor. The chapters of this dissertation are organized to move logically from the basic properties of non-interacting molecules and metals to their controlled assembly using biology as a template. The questions I ask and attempt to answer are those of distance, energy, and nanoparticle size dependence of the energy transfer efficiency of dye molecules to nanometal surfaces. Also, we query the effect that a 1.5 nm diameter nanoparticle will have on the activity of small ribozyme systems.

This dissertation is organized into the following chapters: Chapter 2 attempts to describe the fundamental photophysics of organic dyes necessary to understanding energy transfer to metal surfaces. Chapter 3 applies the theory discussed in Chap. 2 as organic dyes of different energies are separated from 1.5 nm gold particles at discrete distances using DNA as a spacer. Chapter 4 asks questions regarding the efficiency of energy transfer to a metal nanoparticle

as the nanoparticle increases in size. Chapters 5 and 6 apply the information learned with respect to the distance dependence of energy transfer to understand cleavage and folding kinetics of hammerhead RNA ribozymes as well as conformational changes in the ribozyme structure. Finally, Chap. 7 changes gears and probes the potential use of ZnS-overcoated CdSe QD's for applications to biology by combined synthetic, structural, and photophysical characterization of a series of controlled crystallite structures.

CHAPTER 2

THEORY OF ENERGY TRANSFER TO METALS

2.1 Introduction

This chapter will examine the optical and electronic properties of metals in an attempt to understand how the existence of a metal in the close proximity of an electronic dipole, such as exists in an organic dye molecule, will perturb the photophysical properties of the electronic state. In particular, we are interested in studying the physical meaning of energy transfer from an electronic molecular dipole to a metal acceptor of that energy. The understanding of such a process will be facilitated by a deep understanding of the interactions possible between an excited dye molecule and a nearby metal surface, ie. the basic optical and electronic properties of the individual components involved in this process.

This chapter will be organized by first examining in section 2.2 the optical properties of organic dyes in terms of absorption and spontaneous emission of light, and the different means of perturbing these processes. The next section (2.3) will examine the electronic properties of metals, and how the electronic structure of a metal will dictate its interaction with an electromagnetic field. Section 2.4 is a review of the literature and the underlying theories of energy transfer to metals.

2.2 Photophysical Nature of Organic Dyes

Organic dyes are an integral part of biological research, especially for their usefulness in cellular imaging or distance measurements via FRET based studies. Understanding the mechanisms by which intensity or fluorescent lifetimes of a dye may be correlated to distance requires an understanding of the basic photophysics which govern the behavior of that dye. The interactions with light of most dyes can be related through the basic properties of

oscillator strength (f), dipole moment (μ), extinction coefficient (ε), radiative rate (k_r), observed lifetime (τ_{obs}), and quantum yield (Φ).

The absorption or emission of light for a certain molecular transition depends upon the density of states of the upper and lower levels as well as the transition probability between those states. In general, the transition probability is given by

$$P = \langle \Psi_i | \hat{\mu} | \Psi_k \rangle^2 \quad (2.1)$$

where Ψ_i and Ψ_k are the wavefunctions of the initial and final states, respectively, and $\vec{\mu}_{ik}$ is the transition dipole matrix element coupling states $|i\rangle$ and $|k\rangle$. Light induced absorption by a molecule is determined by the ability of an electron in the nuclear framework to interact with an incident electromagnetic field of the radiation, and the intensity of this process is determined by the transition probability. The oscillator strength, f is a classical concept which relates the transition probability between states to a normalized value, where $f=1$ is a perfect oscillator. The line strength of that absorption, commonly referred to as the extinction coefficient ε , is a measure of the probability for the molecule to undergo an absorption process and is an experimentally useful way of determining the oscillator strength. For an optical transition, the oscillator strength is defined by the following equation:(14)

$$f_{ik} = \frac{1}{g_i} \frac{8\pi^2 m_e \nu}{e^2 h} |D_{ik}|^2 \quad (2.2)$$

where g_i is the degeneracy of the ground state and $|D_{ik}|^2$ is the sum over all dipole-allowed transitions for the states $|i\rangle$, $|k\rangle$, also known as the line strength of transition. The concept of oscillator strength is especially important because it can be shown to be directly related to the radiative rate of a molecule.(15; 16; 14) Einstein's A_{ki} and B_{ik} coefficients, which determine the transition probability for spontaneous emission and light induced absorption, respectively, are related by:(17)

$$A_{ki} = \frac{8\pi h \nu_{ik}^3}{c^3} B_{ik} \quad (2.3a)$$

where:(14)

$$B_{ik} = \frac{2\pi^2}{3\varepsilon_0 h^2} |\vec{\mu}_{ik}|^2 \quad (2.3b)$$

and by placing eqn. 2.3b into eqn. 2.3a we solve for the spontaneous emission rate, A_{ki} :

$$A_{ki} = k_r = \frac{16\pi^3 \nu_{ik}^3}{3\varepsilon_0 h c^3} |\vec{\mu}_{ik}|^2 \quad (2.4a)$$

$$= \left(\frac{2}{3}\right) \frac{8\pi^2\nu^3}{\varepsilon_0 h c^3} \frac{\pi^2}{\pi^2} |\vec{\mu}_{ik}|^2 \quad (2.4b)$$

$$= \frac{\omega^3}{3\varepsilon_0 \hbar \pi c^3} |\vec{\mu}_{ik}|^2 \quad (2.4c)$$

where ε_0 is the permittivity of free space, $\vec{\mu}_{ik}$ is the dipole moment, and ω is the angular frequency ($2\pi\nu$) of the transition. This form of Einstein's A_{21} coefficient is the same as published by Craig(17) and can be shown to be identical with that published by Demtröder.(14) Later, Lewis and Kasha(15) corrected this equation to account for the index of refraction, also described by Strickler and Berg(16) when the molecule exists in absorbing media, bringing it to the form:

$$A_{ki} = \frac{\eta^3 \omega^3}{9\varepsilon_0 \hbar \pi c^3} |\vec{\mu}_{ik}|^2 \quad (2.5)$$

The significance of Einstein's A_{ki} coefficient is that an understanding of the dipole moment is the main ingredient for calculating the radiative rate for a molecule, and the dipole moment is related to line strength via: $S_{ik}=|\vec{\mu}_{ik}|^2$, where S_{ik} is the line strength for the transition $|i\rangle \rightarrow |k\rangle$. By this statement the argument comes back full circle in relating the strength of an absorptive transition to the radiative rate of the molecule.

The (theoretical) radiative rate of a molecule may be determined by a controlled absorption spectrum in which a known concentration of analyte is present at a known pathlength for interaction with an incident beam of light. After converting absorption to extinction ($\epsilon_{max} \frac{Abs(\lambda)}{Abs_{max}}$) and scaling in terms of energy (cm^{-1}), then by using eqn. 2.2, integration over the entire region of interest gives the line strength of all dipole-allowed transitions between states $|i\rangle$ and $|k\rangle$. Because the radiative rate is determined by the oscillator strength and the surrounding dielectric medium, the radiative rate may be calculated using the following:(16)

$$A_{ki} = k_r = 2.880 \times 10^{-9} \eta^2 \nu_{ki}^{-3} f \quad (2.6)$$

If the spontaneous emission rate of a molecule is determined by the dipole moment and the index of refraction, then a typical calculated radiative rate is on the order of 10^8s^{-1} . Why then do many very strongly absorbing molecules exhibit lifetimes of only a couple nanoseconds, (Fluorescein, Cyanine Dyes, Alexa Fluor dyes)? The reason for this observation is simple, arising from the fact that the spontaneous emission rate is the longest *possible* process the molecule can exhibit if no other processes were present. However, the

oscillations of an excited state molecule are accompanied by molecular vibrations as charge moves across the conjugated framework. If the energy of these vibrations is damped by the surrounding bath, then the energy is lost as heat and not as a photon of light. This gives rise to a rate of de-excitation, k_{vib} which is in direct competition with k_r . Other rates may also be in direct competition with k_r such as the rate of intersystem crossing k_{isc} , if spin-orbit coupling is significant, and the rate of photo-product formation k_p if a light-induced chemical product formation is possible. All of these rates are responsible for the observed rate of decay for an excited state molecule and may be written as:

$$k_{obs} = k_r + k_{vib} + k_{isc} + k_p \quad (2.7)$$

where for a given set of unchanging conditions, all rates not leading to the emission of a photon may be placed into a single non-radiative rate, k_{nr} :

$$k_{obs} = k_r + k_{nr} \quad (2.8)$$

There are two common methods for measuring the radiative rate experimentally. The first, and perhaps most accurate method involves measuring the luminescent lifetime of the dye at very low temperature where the non-radiative pathways to ground have effectively been eliminated. The second method may be done at room temperature and involves measuring both the luminescent quantum yield and the luminescent lifetime for the molecule. In this case, the radiative rate may be extracted from the following relation:

$$\Phi = k_r \tau_{obs} \quad (2.9)$$

where τ_{obs} is the observed lifetime of the molecule in question, and is equal to $1/k_{obs}$.

Under special conditions, an energy transfer event given by k_{et} may take place if an acceptor transition dipole of the correct orientation, energy and spatial separation is present. In this case the observed rate takes the form:

$$k_{obs} = k_r + k_{nr} + k_{et} \quad (2.10)$$

Extracting the rate of energy transfer k_{et} from a system in which an acceptor is present can be garnered from the difference in two separate luminescence lifetime experiments in which the acceptor is present in the first, and absent in the second. The difference in k_{obs} between the two experiments is then due to the rate of de-excitation via energy transfer.

$$k_{et} = k'_{obs} - k^{\circ}_{obs} \quad (2.11)$$

Note that this process does not require the measurement of a quantum yield, but still gives the quenching efficiency of the acceptor through the relation: $Q_{Eff} = 1 - \frac{\tau'}{\tau_o}$ where τ' is the observed quenched lifetime and τ_o is the natural observed lifetime in the absence of an energy acceptor.

The relations that were just made between k_{obs} and k_{et} assume that a single energy-transfer process is giving rise to the quenching. This assumption should be verified while performing the experiment by the observation of a single-exponential observed lifetime in the case of energy transfer. If the presence of a second rate, or a distributed lifetime were the better fit to the observed decay, then Eqn. 2.11 will be the sum of all quenching rates, but not the rate for a single process.

2.3 Electronic and Optical Properties of Metallic Nanocrystals

A metal is defined as a material which is malleable, has luster, and displays high thermal and electrical conductivity. The properties of bulk solids can often be described through an inspection of the evolution of electronic states from atoms to clusters to bulk solids, and metals are no different. Based upon Fermi-Dirac statistics, electrons are fermions with half-integer spins containing unique quantum numbers which, following the Pauli exclusion principle, means that each quantum state may contain only a single particle. The ramification of these theories into band structures of matter can be illustrated with a simple state-splitting model, (Fig. 2.1.) As more and more atoms are added to a system, that system will go from atomic-like electronic energy levels to having more complex, yet still discrete energy splitting in the cluster form, until the difference between neighboring energy levels becomes indistinguishable from the next. In this case, the energy levels are considered to be a continuous “band” of energy, and no longer discrete. Although all matter types exhibit this behavior, band structure is most commonly split into 3 relativistic categories: Insulators, Semi-Conductors, and Metals. The difference between each of these categories relies upon the relative energy difference between the bottom of the conduction band and the top of the valence band. For metals, the Fermi energy, E_F , (defined as the highest energy level achieved for all fermions at absolute zero), overlaps with the conduction band, allowing the free movement of energetic electrons within the solid. This property of electronic states for metals gives rise to their conduction properties and influences the optical properties.

Atomic \longrightarrow Clusters \longrightarrow Bulk

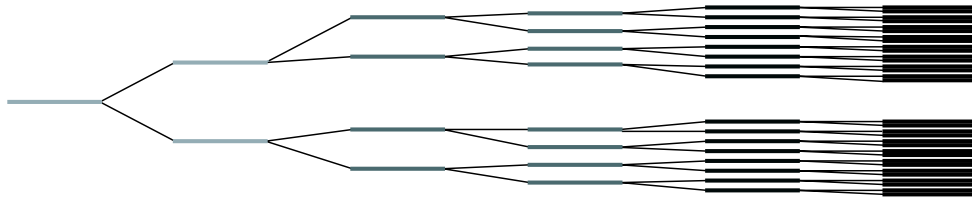


Figure 2.1: Scheme of energy splitting from the atomic level up to bulk solid. Electrons follow Fermi-Dirac statistics and therefore split levels as more atomic states are added. Eventually there are enough states that the energy splitting between states becomes indistinguishable and is considered to be a continuous band of energy. This demonstrates band formation for a semiconductor where there is an energy gap between the valence and conduction bands. For a bulk metal system, these bands form one continuum.

In the past couple of decades, research has shown an intensified interest in the electronic and optical properties of materials as their dimensions are reduced to the nanometer scale. This is an interesting question because the electronic properties are changed drastically as the density of states decreases and the spatial dimensions of electronic motion become confined. These changes in properties are also translated into dynamic optical properties because the interactions of a material with light are primarily electronic in nature. One of the most interesting properties of metals as dimensions become confined is the observation of surface plasmon resonance, (SPR).

SPR resonances have fascinated scientists and artists alike for centuries, where colloidal metal nanoparticles (NPs) were used for their vibrant colors in stained-glass artwork. The physical origins of SPR bands come from the coherent interaction of conduction electrons with an incident light wave. The interaction of light can be described classically by considering the conduction electrons as a spring perturbed by an oscillating external electric field and a restoring force provided by the heavy ionic core of a metal surface. When the frequency of the external electric field (incoming light frequency) becomes resonant with the coherent electronic motion, the glancing light ray is strongly absorbed by the metal electrons. In general, a passing electromagnetic field may interact with the conduction electrons in any metal as described by absorption features, however the interaction is greatly enhanced within the bandwidth of surface plasmon modes. In the planar metal case, the metal film must be illuminated through a material of higher dielectric for the observation of surface plasmons.⁽¹⁸⁾ However, for metal NPs this condition is relaxed and there are no special requirements for the generation of SPR.^(19; 20) This is the reason that colloidal noble metal NPs display vivid colors in solution under ambient conditions.

When Mie solved for the optical extinction of colloidal metal particles, he performed his calculations under the Drude model. This assumes the positive atom cores are immobile while the conduction electrons are treated as a gas, characterized by similar properties such as the relationship between pressure and the mean-free path of a particle. Pressure for a gas is determined by the density of particles and the average kinetic motion for the system. The mean-free path of a particle in such a system is therefore directly affected by these parameters, where an increase in density or temperature inversely affects the mean-free path of a particle. The Fermi function gives the probability that a particular energy state, E , will

be occupied at a given temperature. The function has the form:

$$f(E) = \frac{1}{e^{(E-E_F)/kT} + 1} \quad (2.12)$$

where E_F is the Fermi energy of the metal, k is Boltzmann's constant, and T is the temperature. The total population of conduction electrons per unit volume is obtained by integrating the expression:

$$n = \frac{8\sqrt{2}\pi m^{3/2}}{h^3} \int_0^\infty \frac{\sqrt{E}}{e^{(E-E_F)/kT} + 1} dE \quad (2.13)$$

which is an integral over the electron density of states multiplied by the Fermi-Dirac distribution function.

Metals have within some volume (considered to be finite but inconsequential for the bulk system), a certain density of free-electrons above the Fermi level for a given temperature. Equation 2.13 relates the number of free electrons to the temperature of the system where it can be seen that increasing temperature increases the number of free electrons in the same volume. This increased density of electrons at higher temperature will decrease the electron mean-free path (as well as conductivity). Although this relation between temperature and decreased conductivity has been understood for a long time, physical scientists have begun to ask questions regarding the optical and electronic properties when the dimensions of a metal fall below the mean-free electron path.(21; 13; 20; 22) Figure 2.2 demonstrates the difference in absorption features that occur as the diameter of the NP moves from very small ($d = 1.4$ nm) to the larger sizes where SPR behavior begins to dominate the region from 450 - 650 nm, (2.8 - 1.9 eV).

While for metallic NPs larger than 20 nm it is assumed that the particle is much smaller than the wavelength of interacting light and the absorption of a colloidal system was solved for theoretically by Mie in 1908(23) giving a combination of absorption and scattering terms. When NPs are synthesized much smaller than the interacting light, (<20 nm) then under the dipole approximation, only the dipole induced by the electromagnetic wave contributes significantly to the absorption cross-section. Mie's theory can then be reduced to the form:(20)

$$\sigma = \frac{9 \cdot V \cdot \varepsilon_m^{3/2}}{c} \cdot \frac{\omega \cdot \varepsilon_2(\omega)}{[\varepsilon_1(\omega) + 2\varepsilon_m]^2 + \varepsilon(\omega)^2} \quad (2.14)$$

where V is the particle volume, ω is the angular frequency of the exciting light ($2\pi\nu$), c is the speed of light, ε_m is the dielectric of the surrounding medium, and $\varepsilon(\omega) = \varepsilon_1(\omega) + i\varepsilon_2(\omega)$

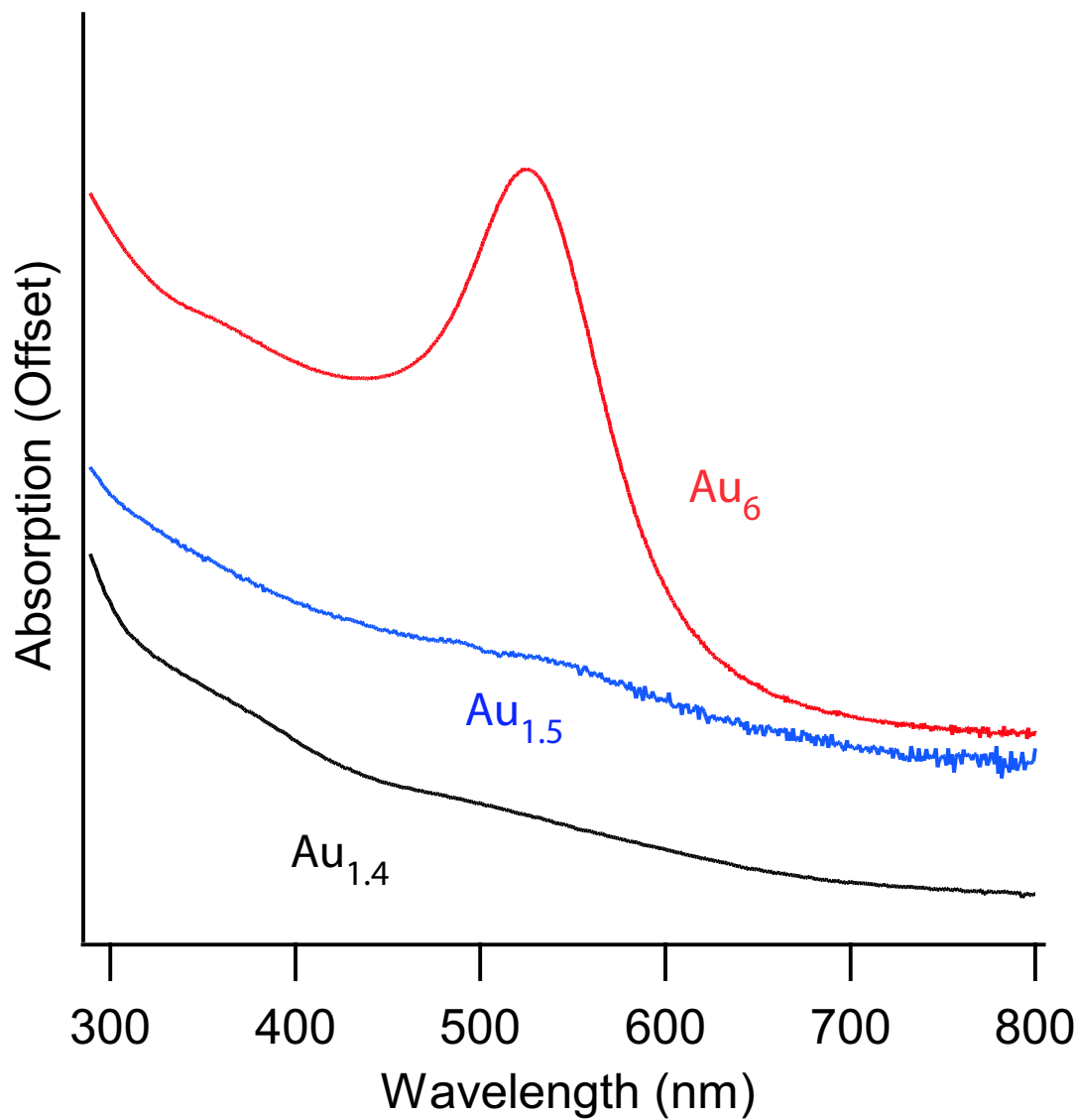


Figure 2.2: Colloidal gold absorption data for $d = 1.4$ nm (black), 1.5 nm (blue), and 6 nm (red) NPs in 20 mM phosphate buffer saline. Below ≈ 2 nm diameter, gold NPs exhibit mostly featureless absorption data with an onset beginning at 1.7 eV (730 nm) due to interband absorption and rising to the UV. When $d > 2.0$ nm the NP displays SPR behavior, giving rise to the large absorption band centered at 525 nm.

is the dielectric of the metal. The use of bulk parameters to describe the dielectric of a metal NP at this size regime is a subject not free of controversy for the reasons stated above. The mean-free path of bulk gold has been measured and is reported as 430Å(24), which begs the question: What happens to the optical properties and electronic states of a gold NP as its dimensions drop below 43 nm? Kriebig began advancing the theory that as the dimensions are reduced beyond the mean-free path the surface scattering of electrons may begin to dominate the optical response.(12) Kriebig *et al.* and Alvarez *et al.* have both applied experimental results based for the small gold NPs to theoretical dielectric functions as an attempt to model the absorption of such metallic particles.(13; 12)

For metals, the dielectric constant ϵ_m is a combination of real and complex values, which take into account the lagging response of conduction electrons in an accelerating field due to a smeared positive background (ionic core atoms). The Drude model takes the form:

$$\epsilon_{1D}(\omega) = 1 - \frac{\omega_p^2}{\omega^2 + \omega_0^2} + \frac{i\omega_p^2\omega_0^2}{\omega(\omega^2 + \omega_0^2)} \quad (2.15)$$

where $\omega_p^2 = [ne^2/(\epsilon_0 m_{eff})]$ is the bulk plasmon frequency (8.89 eV for Au) in terms of the free-electron density n , the fundamental electron charge e , the permittivity of a vacuum ϵ_0 , and the electron effective mass m_{eff} . The frequency of inelastic collisions, ω_0 from electron-electron, electron-phonon, electron-defect, etc. is usually very small, however can become a dominant term for very small NPs. The interband transitions account for the response of the 5d electrons and is nearly constant, but response of the Drude free-electrons can be greatly affected by the decreased size and electron-surface scattering. Therefore, the use of a surface damping (γ) term for the small sizes has been suggested in place of ω_0 :(25; 13)

$$\gamma(r) = \gamma_0 + \frac{A\nu_F}{R} \quad (2.16)$$

where A is called the proportionality factor which includes details of the scattering process.(12; 25) Its value ranges from 1 if isotropic, to 3/4 if diffusive, and zero if elastic. ν_F is the Fermi velocity of an electron in the metal, (gold = 1.4×10^8 cm/s) Using Eqn. 2.16 as the dominant scattering term in Eqns. 2.15 yields a full expression for the size dependent (R) dielectric constant.

$$\epsilon(\omega, R) = 1 - \frac{\omega_p^2}{\omega^2 + (\gamma_0 + A\nu_F/R)^2} + \frac{\omega_p^2(\gamma_0 + A\nu_F/R)}{\omega^2 + (\gamma_0 + A\nu_F/R)^2} \quad (2.17)$$

The inclusion of this surface damping term gave good agreement between experimental and theoretical results for Kriebig(25) for particle sizes down to 3.1 nm but the smaller NP sizes required further terms for Alvarez *et al.*

Alvarez *et al.* compared the optical absorption spectra for a series of gold NPs from $d = 1.7$ nm to 2.5 nm by separating out the interband and Drude components from the total dielectric function:(13)

$$\epsilon_1(\omega) = \epsilon_{1IB}(\omega) + \epsilon_{1D}(\omega) \quad (2.18a)$$

$$\epsilon_2(\omega) = \epsilon_{2IB}(\omega) + \epsilon_{2D}(\omega) \quad (2.18b)$$

where the Drude-like terms may be calculated by:

$$\epsilon_{1D}(\omega) = 1 - \frac{\omega_p^2}{\omega^2 + \omega_0^2} \quad (2.19a)$$

$$\epsilon_{2D}(\omega) = \frac{\omega_p^2 \cdot \omega_0}{\omega(\omega^2 + \omega_0^2)} \quad (2.19b)$$

These equations have size-dependence built into them, exactly the same as Kriebig has done, by substituting Eqn. 2.16 in for the damping term, ω_0 . Figure 2.3 demonstrates behavior of each dielectric as a function of optical energy. The dielectrics were calculated using the values for optical constants of gold published by Johnson and Christy(24) together with the relationships: $\epsilon_1 = n^2 - k^2$ and $\epsilon_2 = 2nk$. The separation of the interband and Drude terms from each other was accomplished by fitting the Drude segments to spline graphs, analogous to the efforts of Alvarez. Doing this allows us to re-calculate the Drude contributions, which should be strongly affected by size, using Eqns. 2.19a,2.19b. Because the interband contributions are constant, even at the smallest sizes measured at 1.4 nm, only the Drude terms need to be re-calculated.

The extinction spectrum can be calculated, therefore, using these new size-dependent dielectric functions together with Eqn. 2.14. Figure 2.4 shows three calculated extinction spectra for bulk gold, a 6 nm NP, and a 1.5 nm NP, (details of the calculations may be found in Appendix A). The disappearance of the plasmon absorption is obvious at smaller sizes, which is consistent with a lower density of free electrons. Although the density of electrons is dropping at these smaller sizes, Alvarez *et al.* realized some very interesting results when trying to fit the theoretical results to the experimentally measured values.

The original attempts by Alvarez *et al.* to fit the experimentally measured optical absorption spectra for small gold NP's resulted in poor agreement with the theory. What they

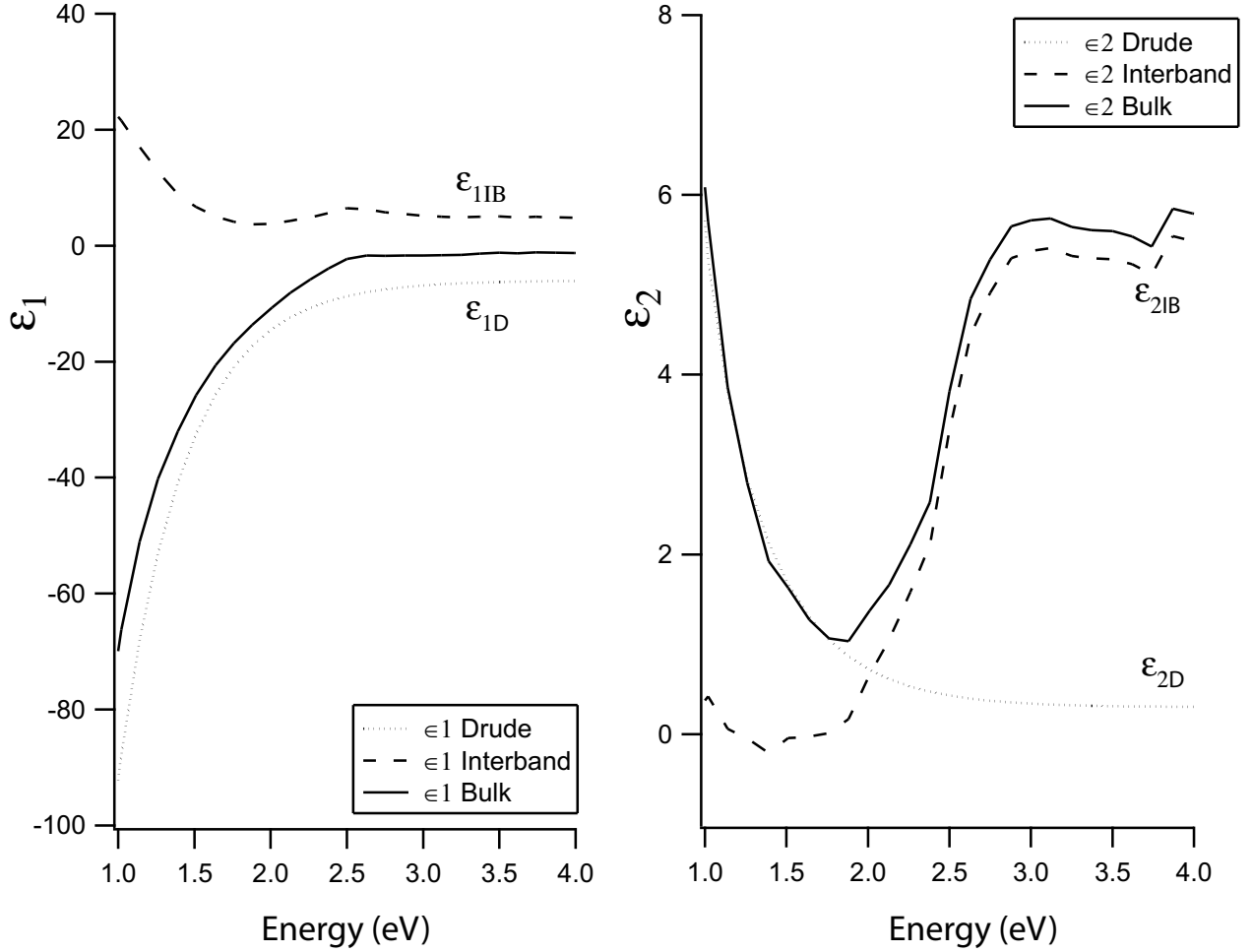


Figure 2.3: *Left:* Real part of the dielectric constant for gold as a function of optical energy. *Right:* Imaginary part of the dielectric. The bulk values represented by the solid line (—) have been extracted and plotted from the published values of Johnson and Christy(24). The Drude contributions (\cdots) have been spline fit and subtracted to isolate the interband contributions (- - -).

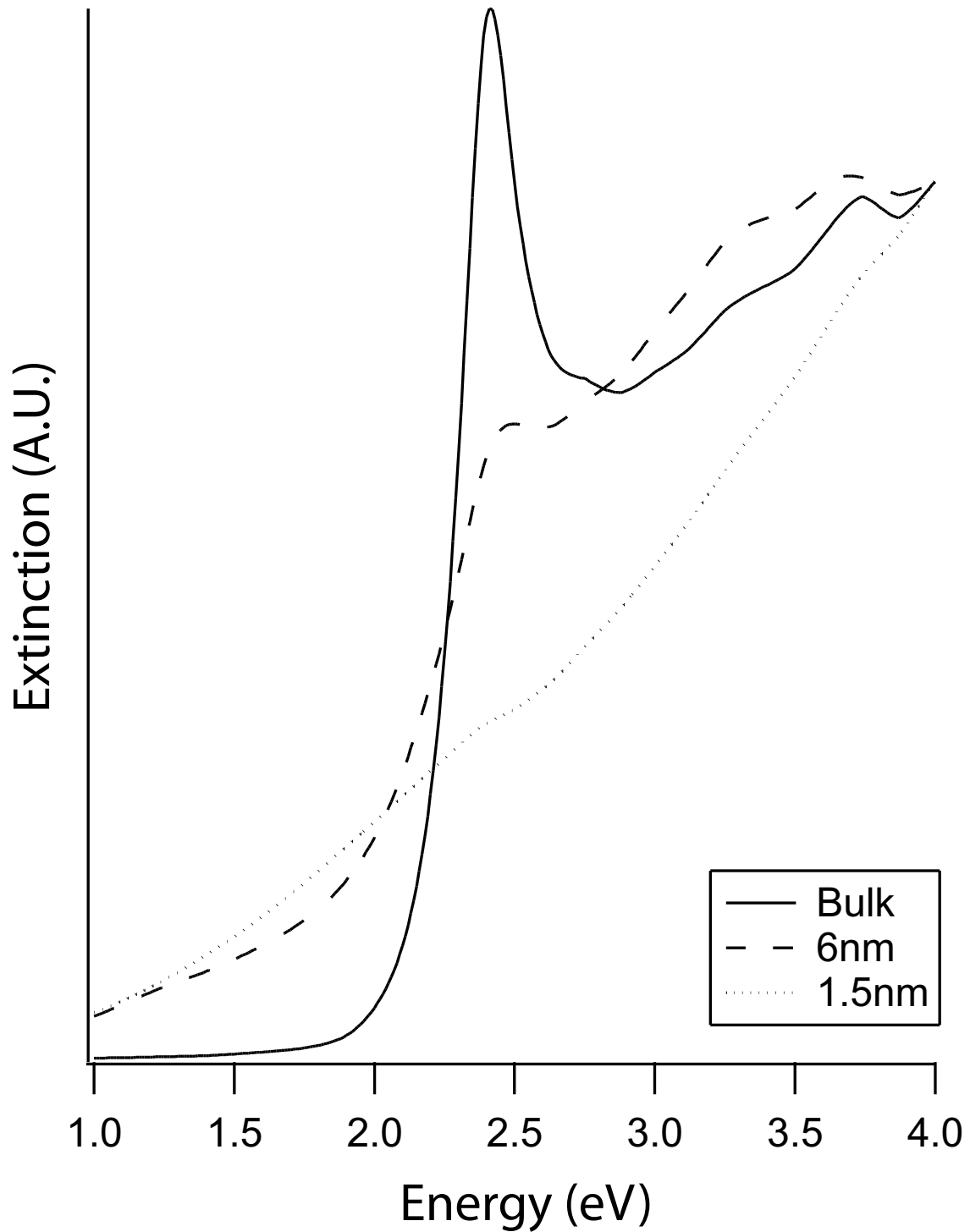


Figure 2.4: Theoretically generated gold extinction spectra using the dielectric terms calculated exactly analogous to Alvarez *et al.* The solid line (—) is the spectrum for bulk gold calculated using exactly the values published by Johnson and Christy. Also calculated are extinction spectra for a 6 nm gold NP (- - -) and for a 1.5 nm NP (\cdots). All spectra were normalized at 4.0 eV.

realized is that by allowing the volume of the particle to float in their extinction calculations (Eqn. 2.14) resulted in greatly improved fits to experimental data. Essentially, this has the effect of changing the electron density and, if chemisorption effects are considered, this has the physical meaning that the surface thiol ligands behaved as electron donors into the NP, where each ligand is donating exactly one electron into the metal. This means gold NPs from 1.7 - 2.5 nm in diameter may have free electron densities higher than would normally be predicted and the theoretical extinction within the dipole approximation is best obtained when electron density (particle volume) is allowed to float. The significance of Alvarez' findings may be seen in section 2.4 where gold NPs near 1.5 nm in diameter are used as dipole acceptors for energy transfer from molecular dyes. The increased electron density of small NPs may help explain the somewhat unexpected efficiency of energy transfer to these particles. These calculations also find relevance in calculating theoretical distances of energy transfer in Chap. 4 to slightly larger particles where the electron density is much higher, but the size-dependent dielectric constants still need to be considered.

2.4 Energy Transfer to Metal Surfaces

Questions regarding the physical behavior of a dye placed at various distances in front of a reflecting surface, (planar metal), have been the focus of much research and experimentation for the last few decades. As technology advances to smaller and smaller, more compact systems, the behavior of similar dipole emitters in the proximity of nanometal surfaces becomes an intriguing question. The purpose of this section, therefore, is to give a brief explanation for the accepted behavior of molecular dyes near metal surfaces.

Beginning with the experiments of Drexhage(26; 27; 28) in the 1960's the behavior of an oscillating electronic dipole in front of a metal surface has been intriguing to theoreticians and experimentalists alike. Drexhage showed that the oscillating electric field of a dipole may be reflected back by a planar reflecting surface to the point of origin, however a phase-shift may be induced by the round trip, depending upon the distance between dipole and mirror. The reflected field will perturb the electric dipole by forcing an external driving term for its oscillations and, in the end, both resonate at the same frequency:(29)

$$\mu = \mu_o e^{i(\omega + \Delta\omega)t} e^{-bt/2} \quad (2.20)$$

where:

$$E_R = E_o e^{-i(\omega+\Delta\omega)t} e^{-bt/2} \quad (2.21)$$

In this case, the unperturbed dipole (μ_o) and the local electric field E_o are being self-modulated by the frequency shift and the lifetime ($\Delta\omega$ and b) in the presence of the mirror. The effect of such a reflected electric field is to modulate the radiative rate of the molecule by either enhancing radiative decay when the reflected field is in phase with the molecular dipole, or through damping when out of phase.

Numerous theoreticians have calculated the perturbed emission rate of single dipole emitters when in the presence of small metallic spheres.(30; 31; 18; 32; 33; 34) Typically the rate of energy transfer into a metal is calculated assuming electron-hole pair formation(35) (and eventually Joule-heating) which becomes the primary source of non-radiative pathways to ground for a nearby excited state molecule. The Gersten-Nitzan model (GN-model) was one of the first theoretical treatments for a molecular dipole in the presence of either a metallic sphere or spheroid. The GN-model is primarily concerned with the lifetime and fluorescence yield of a molecule as a function of both the size and shape of the metallic sphere/spheroid. They take into account the aspect ratio of the NP and the reflected electric field from the surface to calculate the new radiative rate due to enhanced electric field, and non-radiative rate due to energy transfer into the NP. The GN-model is applicable to systems in which the NP is describable by large polarizability (SPR behavior). Although the GN-model has been popular for describing the quenching of dipole emitters to moderately sized gold particles, (6-30 nm), it seems to have fallen short in the prediction of both rates of energy transfer and of the dependence upon distance between emitter and NP surface. (36; 37) Ruppini has approached the theory of energy transfer into metallic spheres also through electromagnetic theory where the process for non-radiative energy dissipation is calculated by considering the Ohmic losses inside the NP. Toward this end, the rate at which energy is absorbed into a sphere is related directly to the response of free electrons (conductivity) of the sphere, or the complex part of $\epsilon(\omega)$. Coupling of the dipole oscillations to the conduction electrons will show enhanced energy transfer at the frequencies corresponding to the $l=1,2$, etc. modes of the metal. Although Ruppini's model is concerned primarily with the $l=1$ plasmon modes at moderate to large distances, it takes into account the dipolar coupling to any conduction electron through the use of ϵ_m in his calculations of wavevector formations.

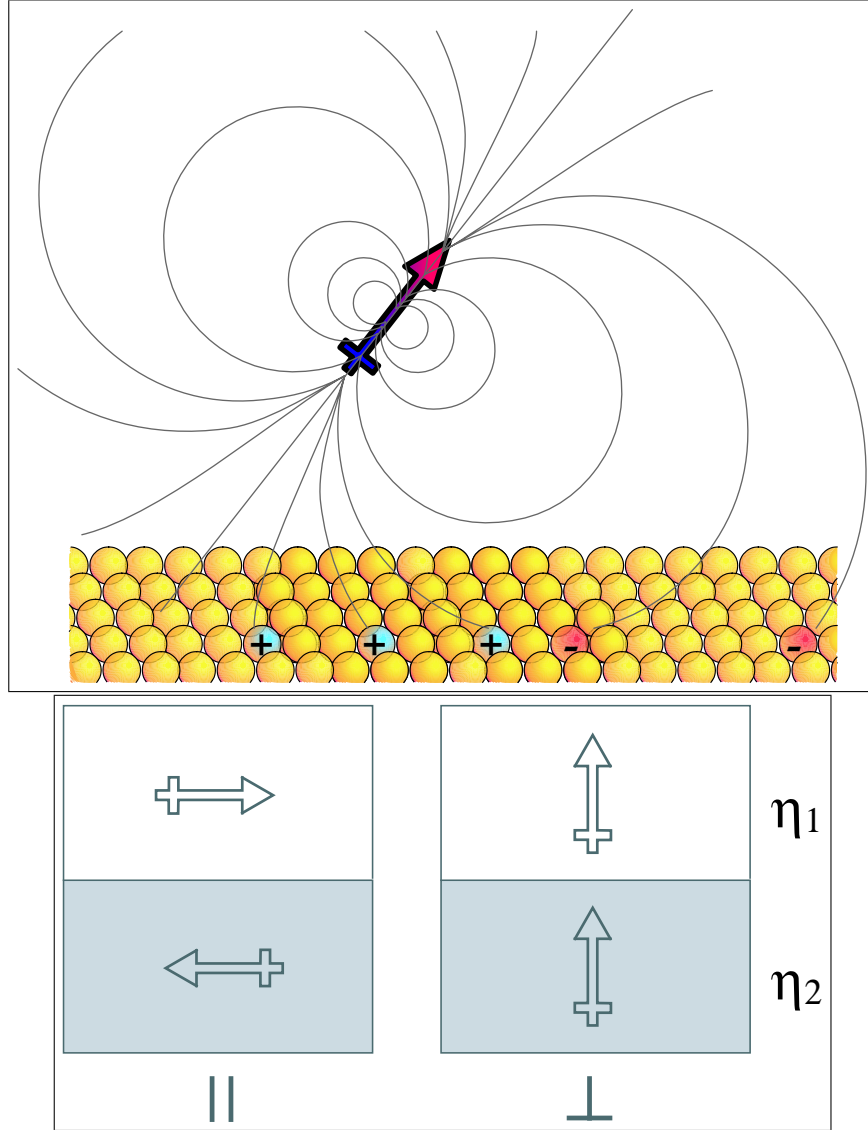


Figure 2.5: *TOP*: Cartoon illustration of a point dipole suspended a discrete distance above a metal surface. The dipolar field lines show the excitation of electron-hole pairs or plasmons on the surface of the metal. *BOTTOM*: Illustration of the orientation dependence of a dipole relative to the surface of a metal. In the parallel orientation (\parallel) the dipole creates an image on the conducting surface, which tends to damp the oscillations. The perpendicular orientation (\perp) results in a dipole image which may enhance the local electric field of the dipole through a driven resonance.

Most significant in Ruppin's model is his conclusion that the most pronounced difference between the interactions of a molecule in the planar and spherical cases is the lack of lifetime oscillations in the spherical orientation at large distances. Spheres would not be expected to reflect the electric field as efficiently as a mirror plane and so the reduced reflectivity will not modulate the local field of the dipole as the molecule increases its distance from the surface.

Persson has been a leader in advancing theories of molecular de-excitation by metal surfaces.(38; 35; 39) The primary focus of Persson's work is the conservation of momentum during electron-hole pair formation via the near field of an electric dipole. Essentially, the electric field of a dipole alone will not provide the required momentum for direct exciton formation, and therefore the process must occur simultaneous with an electron scattering process. Persson recognizes two main sources of scattering: bulk scattering from electron-electron, electron-phonon, electron-defect etc. or the scattering of an electron from the surface potential. The former process involves an interaction over the integrated volume of the crystal, giving rise to a d^{-3} distance dependence. Scattering from a surface potential, however, involves the integration over a plane and yields a d^{-4} distance dependence.

A nanoparticle on the 1 - 6 nm size regime (and possibly as large as 20 - 30 nm) is almost undoubtedly better approximated as a surface due to the high surface-to-volume ratio at these sizes. To this end, the use of Persson's surface damping model(35) applied to molecular dipole quenching is a logical choice of theories. Under this model the metal is treated within the jellium approximation and assumed that conduction electrons may respond instantaneously to the varying external electric field induced by the nearby dipole. The jellium model gets its name from its basic assumption that the atomic framework looks like a smeared positive jelly to the interactions of conduction electrons. This allows a simplification of the electron-electron coupling energies. Their model insists that $\omega_{dye} \ll \omega_p$ which is assumed for dyes ~ 500 nm and lower in energy. They conclude that for a noble metal, the rate of energy transfer may be calculated by:

$$k_{ET} = \frac{\mu_{ik}^2}{4d^3\hbar} F \quad (2.22)$$

where:

$$F_{surface} = 1.2 \frac{\omega_{dye}}{\omega_F k_F d} \quad (2.23)$$

F is the damping factor, the source of which is energy transfer into the metal, and depends upon the metal characteristics, ie. Fermi frequency, electron density, mean-free electron path,

and importantly upon the thickness of metal. Energy transfer to a small metal nanoparticle, ignoring the excitation of bulk plasmons, may be estimated by assuming Persson and Lang's model with excitations of electron-hole pairs simultaneous with the scattering of an electron to a state above the Fermi level. In this model the conservation of momentum is considered to be most important in this scattering process where the total momentum needed for the scattering to take place comes from two sources: a) excitation from the molecular dipole and b) scattering of a free electron against the surface potential. This suggests that in order for a conduction electron to accept energy and damp an external molecular dipole it must undergo a surface potential scattering within a very short time of being excited.(40) For a nanoparticle in which the size of the metal lattice is much smaller than the mean-free electron path ($\sim 430\text{\AA}$ for Au)(24) it is expected that free electrons spend the majority of their time scattering from the surface potential which may increase the probability of molecular de-excitation. Adding eqns. 2.22 and 2.23 together, we achieve the rate of energy transfer to a metal surface:

$$k_{ET} = 0.3 \frac{\mu_{ik}^2}{\hbar} \frac{\omega_{dye}}{\omega_F k_F d^4} \quad (2.24)$$

Equation 2.24 may be expressed in a more useable form by replacing the dipole moment with measureable dye properties, recalling that dipole moment is an integral part of the spontaneous emission rate shown in eqn. 2.4. Therefore, solving eqn. 2.4c for $\frac{|\mu_{ik}^2|}{\hbar}$ and substituting into eqn. 2.24 we achieve:

$$k_{ET} = 0.9 \frac{\varepsilon_o \pi c^3}{\omega_{dye}^2} \frac{1}{\omega_F k_F d^4} k_r \quad (2.25)$$

Finally, in obeying Coulomb's law, the force exerted from one charge upon another through space must be multiplied by the proportionality constant(41) (Coulomb's constant), $\frac{1}{4\pi\varepsilon_o}$. Also noting that $k_r = \Phi/\tau$, this brings eqn. 2.25 to its final useable form:

$$k_{ET} = 0.225 \frac{c^3}{\omega_{dye}^2 \omega_F k_F d^4} \frac{\Phi_{dye}}{\tau_{dye}} \quad (2.26)$$

From equation 2.26 the d_o value may be easily calculated. The significance of d_o is that it represents the distance at which energy transfer probability equals the probability of spontaneous emission.

As mentioned in section 2.3, NPs below a diameter of ≈ 2 nm do not exhibit SPR behavior. This provides a certain justification for the use of the Persson model to explain dipole

quenching to NPs in the range of 1.5 nm because the model does not rely upon the creation of plasmons. Instead, the model relies upon the frequency of the emitter (which must be lower than the plasmon frequency to ensure adiabatic response from conduction electrons) and scattering events at the metal surface. In fact, the use of such small NPs may actually increase the efficiency of energy transfer as a direct result of the *increased* electron density(13) and surface scattering(12; 25) at these small sizes.

CHAPTER 3

NSET VS DISTANCE TO d=1.5 NANOPARTICLES

3.1 Introduction

Application of optical molecular rulers to questions in biochemistry, bio-diagnostics, and bimolecular imaging allows routine measurement of dynamic distance changes in molecules. We recently demonstrated the applicability of a long range molecular ruler consisting of an organic dye donating energy to a small (1.4 - 1.5 nm diameter) gold nanoparticle, termed nanosurface energy transfer (NSET).⁽⁴²⁾ This technique allowed changes in conformational distances between 1 - 20 nm to be probed for protein-nucleic acid interactions on double stranded DNA (dsDNA) using optical methods. NSET is similar to Förster resonance energy transfer (FRET), however the measurable distances are extended nearly 2-times for optical molecular rulers by following a $1/d^4$ distance dependence. The intensity quenching mechanism via coupling of the oscillating electronic dipole of a dye to a metal surface with loss of energy via heat analogous to the theoretical treatment developed by Chance, Prock and Silbey⁽²⁹⁾ and Persson and Lang⁽³⁵⁾ for bulk metals.

This theoretical treatment can explain the oscillator coupling to a metallic nanoparticle (NP) with surprisingly good agreement to experimental data,⁽⁴²⁾ which is unexpected because a 1.5 nm Au NP has neither a significant core, nor displays strong surface plasmon resonance (SPR) character. The observation of quenching behavior that follows the theoretical treatment of Persson and Lang for a bulk metal is surprising due to the poorly developed surface in materials below 2 nm. While these systems are above the limit where the crystal field levels split, they are not large enough to express a coherent surface plasmon resonance. This may not be critical if the logic of Ruppin is applied, where he has theorized that the primary difference between the rates of energy transfer to a plane and to a sphere is manifest in the loss of lifetime oscillations at large distance in the spherical case,

due to reduced reflectivity.(32) This implies that an energy transfer mechanism may not be drastically affected by moving from a plane to the spherical acceptor case.

Although the experimental results are consistent with NSET behavior, seemingly contradictory findings for the optical response of molecular dyes interacting with metal NP's have been reported in the literature with both radiative rate enhancement and energy transfer quenching at moderate distances.(37; 19; 43) A common theme for most theories relies upon the existence of a surface plasmon resonance (SPR) band in the metal particle. The lower quantum efficiency of fluorophores near or on metal surfaces have been interpreted in terms of lossy surface waves,(44; 45) or by suppression of the radiative rate.(37) Under certain conditions, photoluminescence enhancement has been reported and is described as resulting from wavevector matching and coupling to a plasmon for far-field emission via a classical description of light.(19) An interesting question presents itself, therefore, when inquiring about the behavior of a dipole-emitter when the metal does not exhibit an SPR band, such as occurs when the metal particle is very small, ≤ 2 nm.(22) Because 1.5 nm diameter gold NP's do not display surface plasmon character, the only means by which dye quenching will be observed is limited to either a change in the radiative rate (k_r) of the dye or the introduction of an energy transfer rate (k_{et}) to the metal NP. The details of the mechanism can be probed by correlating the photoluminescence (PL) and lifetime (τ) behavior for a set of dyes, spaced at controlled distances

The relationship between photoluminescence (PL) intensity and lifetimes is easily shown by considering that:

$$\tau_{obs} = \frac{1}{k_{obs}} = \frac{1}{k_r + k_{nr} + k_{et}} \quad (3.1)$$

and,

$$\Phi_{em} = \frac{k_r}{k_r + k_{nr} + k_{et}} = k_r \tau_{obs} \quad (3.2)$$

where Eqn. 3.1 states that the observed lifetime, τ_{obs} is the inverse of all rates of decay, k_{obs} ; where k_{obs} is the sum of the radiative rate, k_r , the non-radiative rate, k_{nr} , and the rate of energy transfer, k_{et} . The radiative and non-radiative rates are normally considered constants for a dye under defined conditions, leaving k_{et} as the major contributor to the shortening of an observed lifetime. The quantum yield (Eqn. 3.2) is a convenient measurement relating PL intensity to k_r and the observed lifetime, τ_{obs} . For a high quantum efficiency dye, k_{nr} is very small and one predicts that a change in k_r will lead to a corresponding change in the

observed lifetime of a dye, affecting the measured Φ_{em} . Conversely, energy transfer should lead to a correlated loss in lifetime and intensity for the NP-dye combination. A dilemma is presented by these statements because both a changing k_r and the introduction of an energy transfer pathway (k_{et}) could lead to the observation of quenched PL and a decreased lifetime. How then can one distinguish the true origin of the decreased PL intensity? The purpose of this paper is to demonstrate that the mechanism of PL quenching for an organic dye near a small 1.5 nm NP is almost entirely via energy transfer to the metal surface and that the quenching efficiency is defined by a $1/d^4$ distance dependence, consistent with the predictions of Persson and Lang in an NSET model.

3.2 Experimental

3.2.1 Nanoparticle Synthesis

Gold nanoparticles were synthesized as described by literature techniques,⁽⁴⁶⁾ using the rapid reduction of hydrogen tetrachloroaurate ($\text{AuCl}_4 \cdot 3 \text{H}_2\text{O}$) in the presence of tetraoctylammonium bromide by sodium borohydride in an argon-sparged water/toluene mixture. TEM measurements displayed particles with an average diameter of 1.5 ± 0.5 nm. The particles were washed thoroughly with a variety of solvents including hexanes, sodium nitrite solution, and MeOH- H_2O . Ligand exchange was accomplished using ~ 400 mg Bis(p-sulfonatophenyl)phenylphosphine dihydrate (SPP) in 30 mL nanopure H_2O to 32 mg purified nanocrystal in 32 mL methylene chloride. The two phases were stirred overnight resulting in extraction of the organically-soluble NP to the aqueous phase through ligand exchange. Aqueous NP was lyophilized into small aliquots of ~ 2 nmol/vial and stored at 4°C .

3.2.2 dsDNA - Nanoparticle Coupling

Complementary DNA strands were purchased with either 5'- C_6 -dye or 5'- C_6 -SH already HPLC-purified from IDT DNA Technologies. All strands¹ were engineered to minimize

¹15dye: 5' Dye- C_6 -CGT GTG AAT TCG TGC-3'
15-thiol: 5' C_6 S-S- C_6 -GCA CGA ATT CAC ACG-3'
30dye: 5' Dye- C_6 -CGC CTA CTA CCG AAT TCG ATA GTC ATC AGC-3'
30-thiol: 5' C_6 S-S- C_6 -GCT GAT GAC TAT CGA ATT CGG TAG TAG GCG-3'
45dye: 5' Dye- C_6 -CGT TCC GTG TGC ATA CTG AAT TCC GTG TTA CTC TTG CCA ACC TCG-3'
45-thiol: 5' C_6 S-S- C_6 -CGA GGT TGG CAA GAG TAA CAC GGA ATT CAG TAT GCA CAC GGA ACG-3'

secondary structures using mFold. Purity for Cy5-labeled DNA was verified via HPLC analysis (C-4, 300Å, 10-80% acetonitrile in 45 minutes). Purity for FAM and thiol-labeled DNA was verified on FPLC, (30-90% 1M NaCl in 0.1M NaOH over 30 minutes (≤ 30 mer) or 60 minutes (> 30 mer)). A standard assembly of double-stranded DNA (dsDNA) with the NP was accomplished by first deprotecting 800 pmol of the single-stranded 5'-SH DNA with 50 mM Tris(2-carboxyethyl)phosphine hydrochloride (TCEP) in 20 mM PBS buffer pH 7.5 at RT for 30 minutes. The freshly deprotected DNA-thiol was desalted with a NAP-5 column, collecting the first 500 μ L eluted which contained 75% (600 pmol) of the total DNA loaded onto the column. The dye-containing complementary strand (590 pmol) was immediately added and the strands were annealed at 95°C for 2 minutes, cooled to RT for 2 minutes and then added to 4 nmol of dry H₂O-soluble NP (NOTE: this is 1:6.7 stoichiometry dsDNA:NP to ensure predominately 1:1 binding). The mixture was vortexed and placed at 4°C in the dark for conjugation > 24 hours. Successive (≥ 2) ethanol precipitations were performed to purify unbound NP from the dsDNA-NP conjugate. The purified dsDNA-NP conjugate was reconstituted in 20 mM PBS pH 7.5 buffer and stored at 4° C in the dark.

3.2.3 Absorption/Photoluminescence

Absorption measurements were acquired on a Varian Cary 50 UV-vis spectrophotometer and photoluminescence measurements were acquired on a Varian Cary Eclipse Fluorescence spectrophotometer using Z-matched 50 μ L quartz cuvettes. A typical quantum yield was calculated by measuring the absorption over the 200-800 nm range for both the sample described above and a control (dsDNA-dye without NP), keeping the peak of the dye absorption ≤ 0.1 A.U. Concentrations were kept very dilute (~ 300 nM) to minimize effects due to self-absorption or Stern-Vollmer quenching. Continuous-wave photoluminescence (cw-PL) was first measured on the control strand, adjusting the sensitivity to maximize the PL signal. *Under identical settings* the PL intensity of the dsDNA-NP sample was then measured. Quantum efficiencies of quenching were determined via the following calculation:

$$\Phi_{QEff} = 1 - \frac{I_{sample}}{I_{control}} \cdot \frac{A_{control}}{A_{sample}} \quad (3.3)$$

where Φ_{QEff} is the quantum efficiency of energy transfer, $I_{sample,control}$ is the integrated intensity under the curve for the PL peak in energy, $A_{control}$ is the absorption of the sample

at its absorption peak, and A_{sample} is the corrected absorption of the dye after subtracting out the contribution absorbed by the NP.

3.2.4 Lifetime Measurements

Lifetimes are acquired on dilute (~ 300 nM) samples using the output of a Nd:VO₄-pumped (Spectra-Physics Vanguard, 2 W, 532 nm, 76 MHz, 10 ps) R6G dye laser (Coherent 702-1). Cavity dumping of the dye laser to 1.9 MHz drops the pulse train to 1 pulse every $2 \mu\text{s}$. In the case of FAM the laser is frequency doubled for $\lambda_{ex}=300$ nm, and used as is at $\lambda_{ex}=600$ nm for Cy5. Samples were excited with $<1 \mu\text{W}$ at a right angle geometry relative to a Chromex 500is 0.5 m imaging monochromator with 50 g/mm grating, 0.5 nm resolution. Output of the monochromator is focused into a Hamamatsu C5680 streak camera operating at 20 ns window (FAM) or 10 ns window (Cy5). Lifetimes are measured by binning intensity vs time for a 20 nm spectral range about the λ_{em} maximum for the dye. Lifetime quenching calculated by:

$$Q_{eff} = 1 - \frac{\tau'}{\tau_0} \quad (3.4)$$

was determined by comparing the measured decay rate for a NP-dsDNA-dye system (τ') vs the observed decay rate for the identical dsDNA-dye in the absence of NP (τ_0).

3.3 Results

Figure 3.1 demonstrates the scheme of separating a donor fluorophore from the surface of a NP using three different lengths of dsDNA as a spacer, hereafter referred to as NP-dsDNA-dye. The distance from the center of the molecule to the metal surface is estimated by taking into account the C₆ linkers and the size of the fluorescent dye. The C₆ linkers on either 5' end contribute flexibility to the system, but due to the persistence length of dsDNA, ~ 90

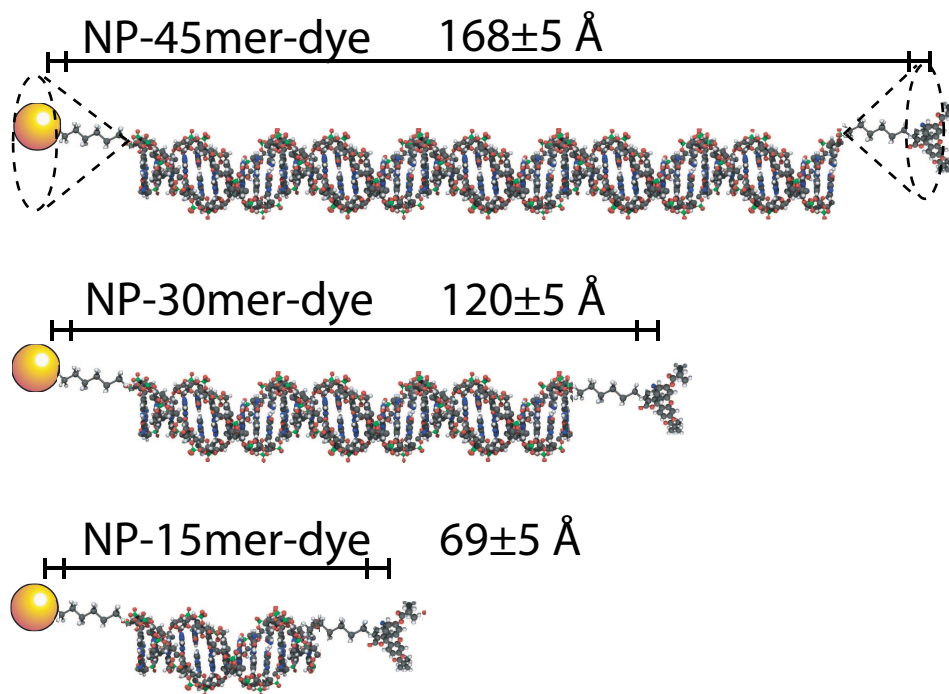


Figure 3.1: Scheme of DNA-binding to a 1.5nm Au nanoparticle, (NP). By varying the length of the DNA strand, the terminal dye fluorophore is separated from the Au NP by discrete distances, (168\AA , 120\AA , and 69\AA .)

nm,(47) and the fact that a d=1.5 nm NP is smaller than the 2 nm footprint of dsDNA it is very unlikely that the lengths of dsDNA used here would have the ability wrap around or interact with the gold NP. The C₆ chain on the dye will produce a cone of probability for the separation distance due to chain flexibility and tend to randomize the dipole vector relative to the nanometal surface so that the primary effect of the C₆ linker is insuring an isotropic distribution of electronic dipoles.

3.3.1 Lifetimes of Dyes Near 1.5 nm NP's

Figure 3.2 compares the lifetimes for both fluorescein (FAM - 3.2a) and Cy5 (3.2b) at all three dsDNA spacer distances from the NP surface. The intensities have all been normalized at the peak and are displayed on a logarithmic graph vertically offset for comparison. The lifetime for each dye clearly decreases with decreasing distance to the surface of the metal sphere, displaying single-exponential decay kinetics fit using a Levenberg-Marquardt algorithm to minimize the residuals about the form: $I(t) = y_0 + I_0 e^{-kt}$. This is the first order rate law where y_0 is a linear offset, I_0 is the intensity at t=0, and k is the rate of decay where $1/k = \tau_{obs}$. These observations suggest that not only is the sample purified from free-dye but also that any variation in length caused by the C₆-spacer is not measurable for this system. All samples are compared to the appropriate dsDNA-dye strand in the absence of the NP (ie. FAM-15mer-NP is compared to FAM-15mer) however only a single dsDNA-dye strand is shown (top - blue) for comparison in Fig. 3.2a,b. Using Eqn. 4.6 the quenching efficiencies as measured by lifetime are listed in Table 3.1 along with the extracted (Eqn. 3.1) and theoretical (Eqn. 3.6) rates of energy transfer.

3.3.2 Photoluminescence Characterization

In Figure 3.3, the cw-PL quenching of FAM (Fig. 3.3a) and Cy5 (Fig. 3.3b) as a function of dsDNA spacer length are compared. The quantum efficiency of quenching for each sample was measured by comparison against a control dsDNA-dye in the absence of NP, using Eqn. 3.3. Quenching efficiencies based on PL studies are tabulated in Table 3.1 vs different spacer lengths.

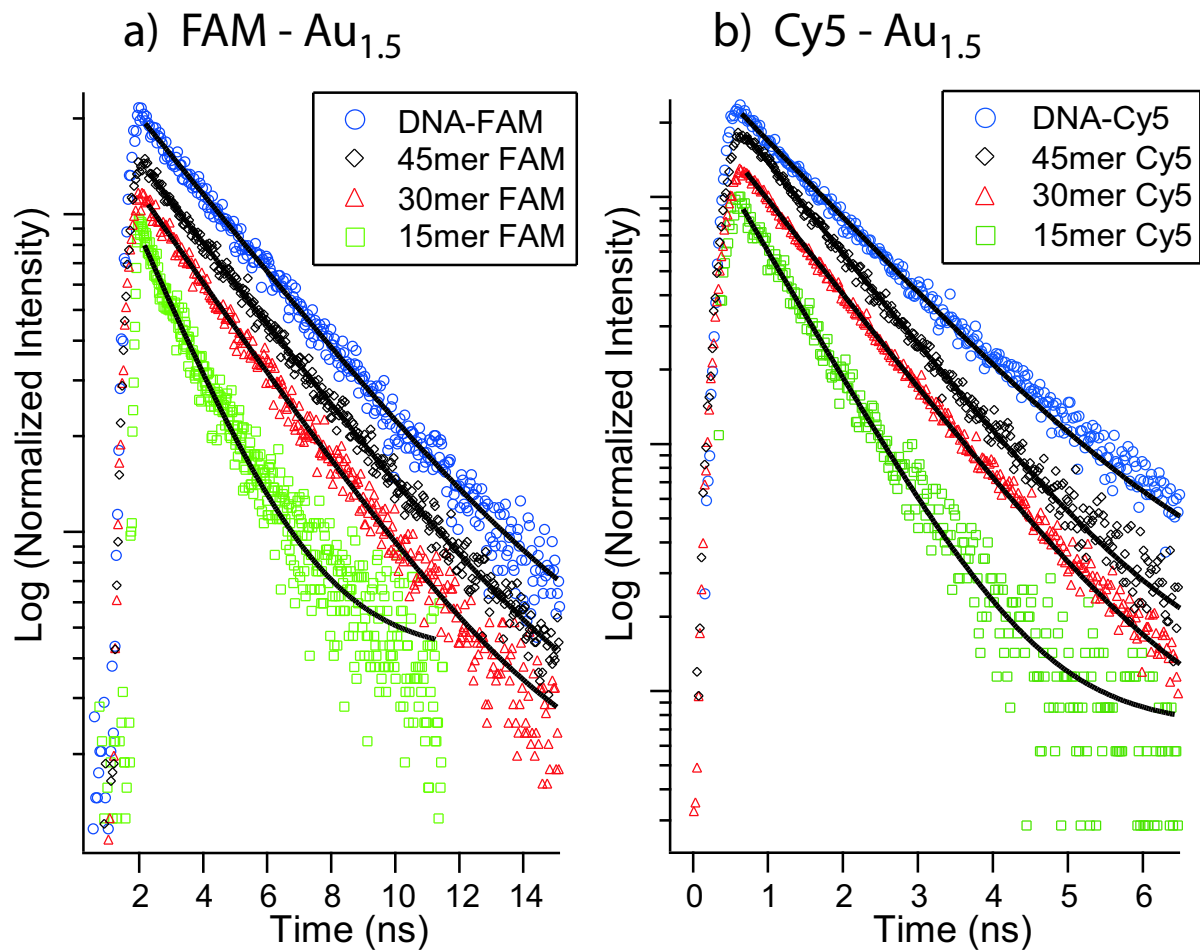


Figure 3.2: Lifetimes of the 15bp (green), 30bp (red), and 45bp (black) NP-dsDNA-dye assemblies for FAM (a) and for Cy5 (b) relative to dsDNA-dye controls (blue - top). The data have been normalized and offset vertically for viewing. Single exponential fits through the data are shown (—).

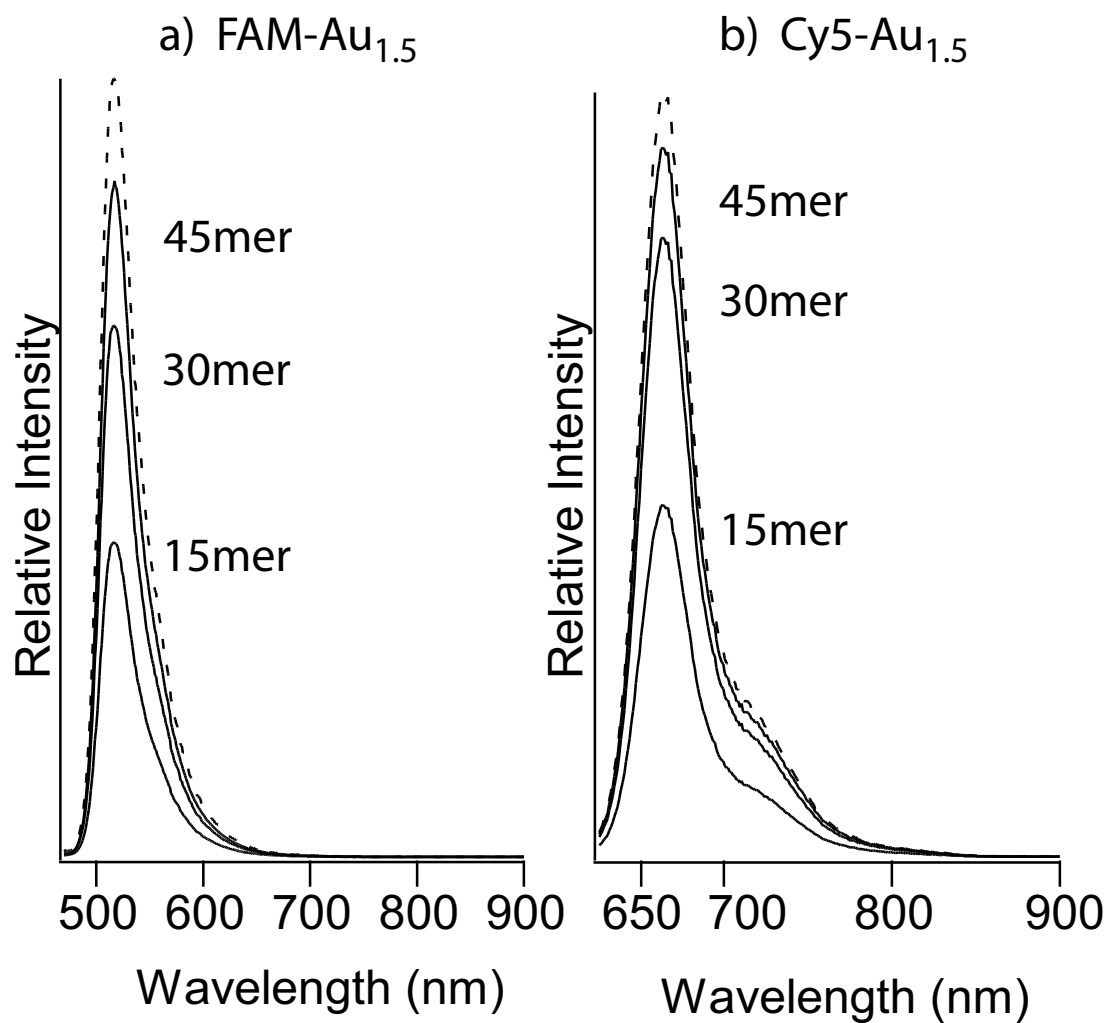


Figure 3.3: a) Photoluminescence quenching of FAM PL intensity as a function of dsDNA spacer length. b) Photoluminescence quenching of Cy5 dye as a function of spacer length. The top curve in both a) and b) (- -) is a normalized control intensity.

3.3.3 Absorption Characterization

Figure 3.4a shows absorption spectra for NP-15mer dsDNA-dye (black, - - -, offset vertically), 15mer dsDNA-dye without NP (\cdots), and the NP-15mer dsDNA-dye (—) after subtracting the absorption arising from the NP. The absorption for the difference spectra is not well resolved at the higher wavelengths, probably a result of unsatisfactorily corrected scattering.

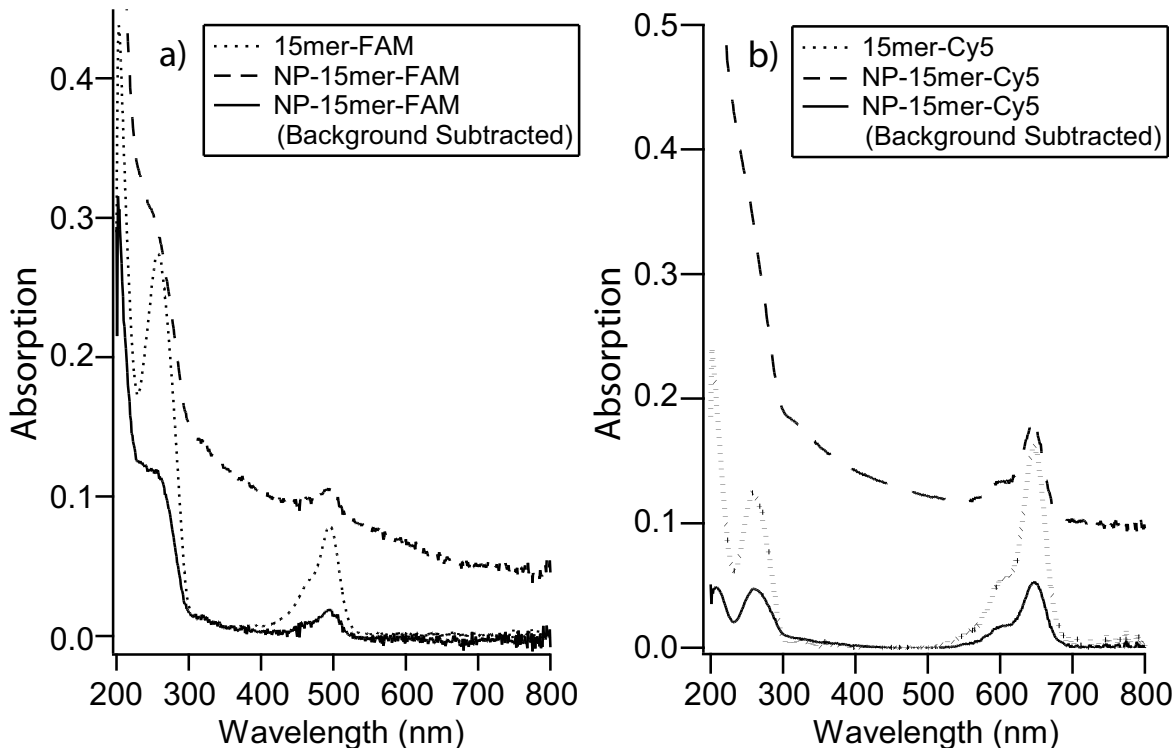


Figure 3.4: a) Absorption and corrected spectra for the FAM-dsDNA-NP system and b) Absorption spectra and corrections for Cy5-dsDNA-NP. These spectra compare purified dye-dsDNA-NP (black - offset 0.05 A.U.-FAM: 0.10 A.U.-Cy5), dye-dsDNA in buffer (\cdots), and the background subtracted absorption spectrum of the dye-dsDNA-NP to correct for NP absorption (—).

3.4 Discussion

3.4.1 Development of the Model

A great deal of theoretical modeling(38; 39; 32; 48; 33; 34; 31; 29) (this list is far from complete) has probed the behavior of a dye in which the molecular dipole is damped by the response of a nearby metal surface. The quenching of the fluorophore intensity must be related to a through-space mechanism involving only the dipole of the donor and some electronic property of the gold NP, likely interactions with free electrons. The lack of an SPR band at the nanometal size used in this study suggests that the coherent behavior of electrons is diminished, negating the resonantly enhanced energy transfer suggested over the plasmon bandwidth,(32; 30) but not the ability of a metal to accept energy. This is an important point because, although a larger sized NP may accept energy more efficiently, the smallest NP possible is the least intrusive for use of NSET as a molecular ruler or beacon in biological assays.

Figure 3.5 illustrates the dipole projections for free-electron scattering at the surface of a gold NP in the presence of an dipole-induced electric field. The high curvature of a 1.5 nm gold NP suggests that all scattering events should be normal to the surface, which relaxes the dependence upon the overlap of projected dipoles.

The Gersten-Nitzan models(30; 49; 50) which have been used for modeling dipole-dipole interactions with the plasmon of gold NP's seem to have fallen short in describing both the distance dependence and efficiency of dye-quenching.(36; 37) The model of Persson and Lang, however, concerns itself primarily with momentum and energy conservation in the dipole-induced formation of electron-hole pairs and is useful for modeling this system. According to this model, the rate of energy transfer is calculated by performing a Fermi golden rule calculation for an excited state molecule depopulating with the simultaneous scattering of an electron in the nearby metal to above the Fermi level. However, in considering the conservation of momentum, the excitation of an electron-hole pair must coincide with an electron-electron, electron-phonon, or electron-surface potential scattering event.

The Persson model(35) states that the damping rate to a *surface* of a noble metal may be calculated by:

$$k_{ET} = 0.3 \frac{\mu^2}{\hbar} \frac{\omega_{dye}}{\omega_F k_F d^4} \quad (3.5)$$

which can be expressed in more measurable parameters through the use of the Einstein A_{21}

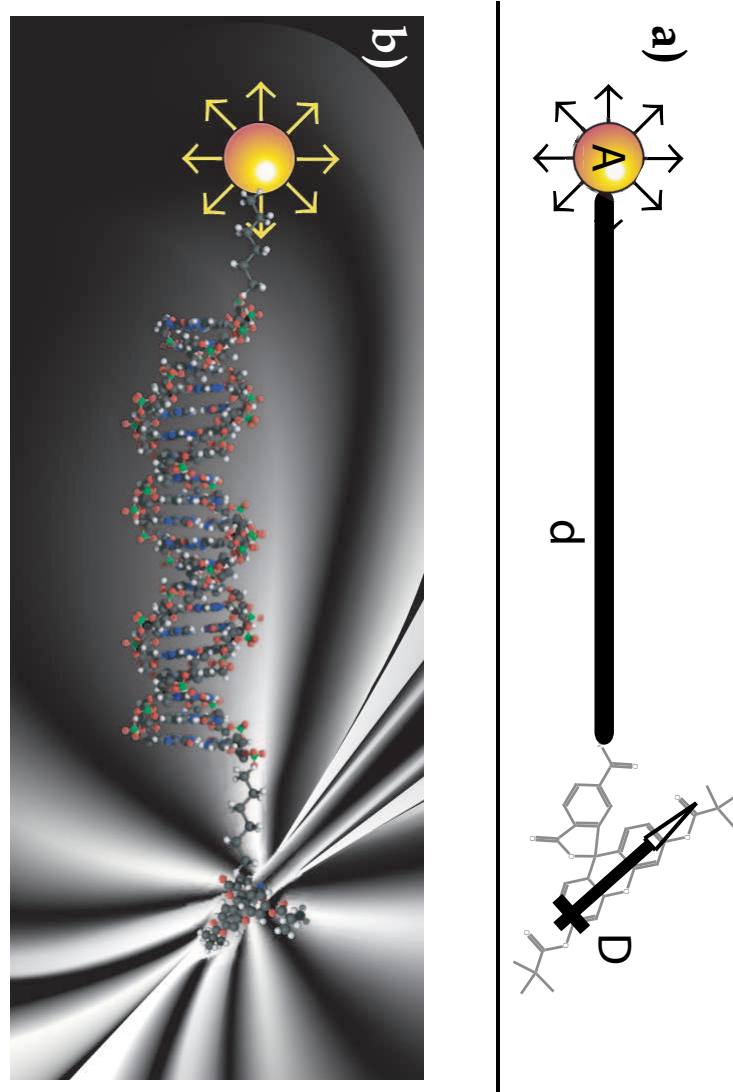


Figure 3.5: a) Graphic representation of a dipole free in space separated by some distance from a metallic NP. b) Illustration of a gold NP in the electric field of a nearby molecular dipole. All scattering events associated with the free electrons of the gold are shown perpendicular to the surface.

Table 3.1: Measured values for the quantum yield of quenching efficiency for the 3 strands of dsDNA based on cw-PL spectra, ($\text{PL } Q_{Eff}$), based on lifetime quenching, (τQ_{Eff}) and both the calculated and theoretical rates of energy transfer to the metal surface, (k_{ET}).

	FAM			Cy5		
dsDNA Strand: Distance ($\pm 5 \text{ \AA}$):	15bp 69 \AA	30bp 120 \AA	45bp 167 \AA	15bp 69 \AA	30bp 120 \AA	45bp 167 \AA
$\text{PL } Q_{Eff}$	0.69 ± 0.07	0.27 ± 0.06	0.22 ± 0.04	0.54 ± 0.06	0.19 ± 0.04	0.07 ± 0.03
τQ_{Eff}	0.47 ± 0.04	0.13 ± 0.03	0.04 ± 0.02	0.41 ± 0.05	0.10 ± 0.04	0.02 ± 0.04
Calculated $k_{ET} \text{ (s}^{-1}\text{)}$	2.55×10^8	4.9×10^7	1.3×10^7	4.87×10^8	8.5×10^7	9.72×10^6
Theoretical $k_{ET} \text{ (s}^{-1}\text{)}$	4.3×10^8	4.7×10^7	1.2×10^7	3.3×10^8	3.6×10^7	8.6×10^6

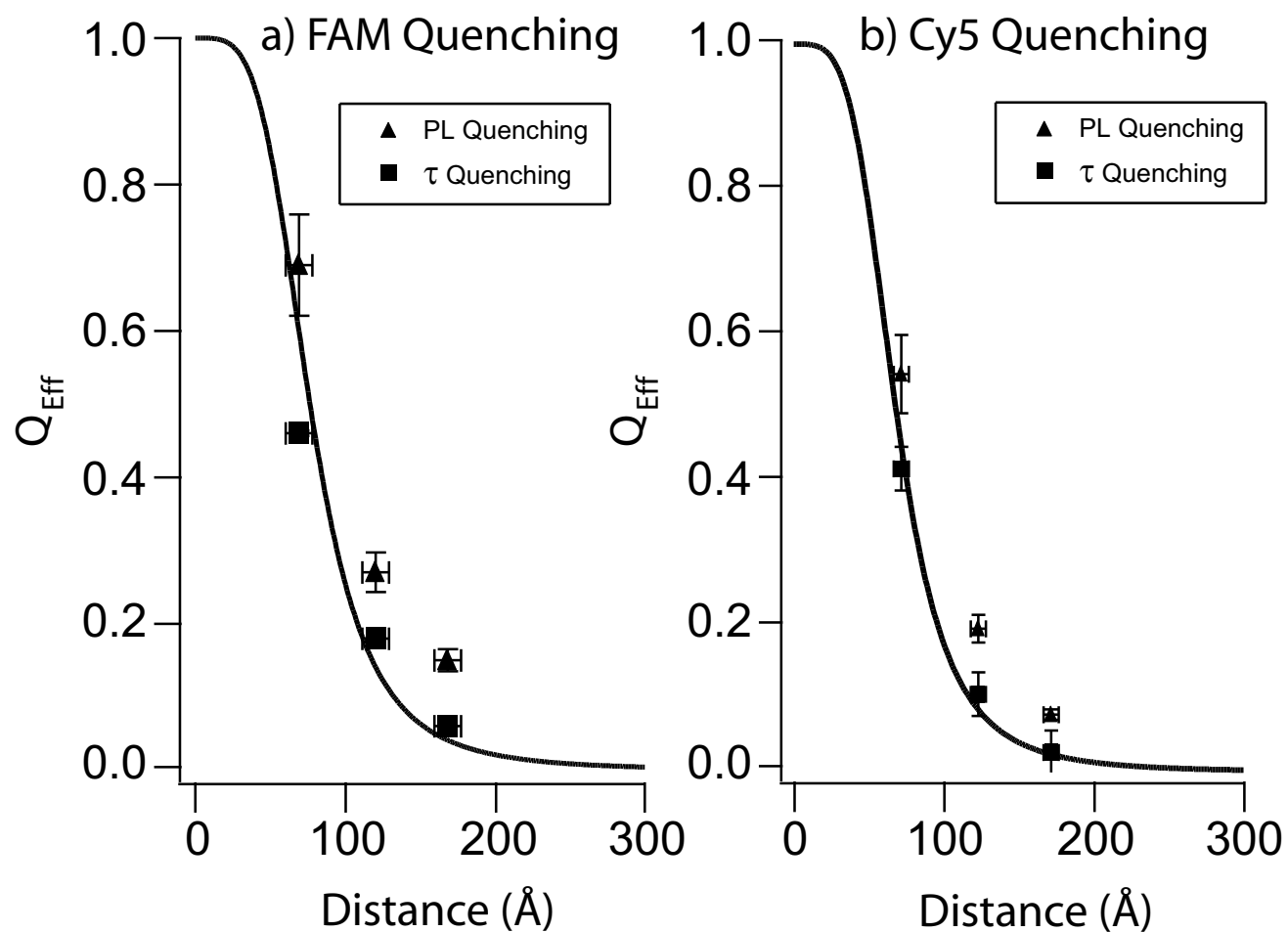


Figure 3.6: Quenching data for FAM (a) and Cy5 (b) based upon Photoluminescence (▲) and Lifetimes (■) overlaid on top of a theoretical curve generated using Eqn. 3.8.

coefficient:(17)

$$A_{21} = \frac{\omega_{dye}^3}{3\epsilon_0 \hbar \pi c^3} |\mu|^2$$

to give the following rate of energy transfer, in accordance with Coulomb's law ($\frac{1}{4\pi\epsilon_0}$):

$$k_{ET} = 0.225 \frac{c^3}{\omega_{dye}^2 \omega_F k_F d^4} \frac{\Phi_{dye}}{\tau_{dye}} \quad (3.6)$$

where c is the speed of light, Φ_D is the quantum yield of the donor (FAM=0.8, Cy5=0.4), ω_D is the angular frequency for the donor (FAM=3.8x10¹⁵ s⁻¹, Cy5=2.91x10⁻¹⁵s⁻¹), ω_f is the angular frequency for bulk gold (8.4x10¹⁵ s⁻¹), and k_f is the Fermi wavevector for bulk gold (1.2x10⁸ cm⁻¹). The d_0 value is a convenient value to calculate for a dye-metal system, yielding the distance at which a dye will display equal probabilities for energy transfer and spontaneous emission. For the Persson model, the d_0 value may be calculated by:²

$$d_0 = \left(0.225 \frac{c^3 \Phi_{dye}}{\omega_{dye}^2 \omega_F k_F d^4} \right)^{1/4} \quad (3.7)$$

We calculate d_0 values of 76.3 Å and 73.0 Å for FAM and Cy5 dyes, respectively. The theoretical plot overlay of the data in Figs. 3.6a,b is shown for comparison and is generated from the expression,

$$Q_{Eff}(d) = 1 - \frac{1}{1 - \left(\frac{d}{d_0}\right)^4} \quad (3.8)$$

It is important to note that this model does not concern itself with the reflected field from the surface, which makes it convenient for the case of a metal NP where, in accordance with Ruppin's model,(32) it is assumed that the reflected field is negligible and does not interfere with the dipole field. For the validity of this model, we assume that the dipole is a point dipole separated from a metal sphere by a rigid distance and that every fluorophore has an acceptor NP associated with it. This assumption is made practical in the material conjugation by saturating the dsDNA with acceptor NP and using less than a stoichiometric amount of donor-labeled strand. Monoexponential lifetimes support the assumption that every donor is located at a rigid distance from the acceptor.

Alivisatos was successful in adapting the Persson model to describe energy transfer from biacetyl donors to a Ag(111) surface with good agreement to experimental data.(40) For their

²This equation is stated as a correction to a previous manuscript (Strouse, *JACS*, **2005**, *127*, 3115.) in which it was calculated in error to be 0.525.

system, it was concluded that the dipole damping as a result of both bulk and surface electron scattering were important. However, a metal particle on the scale of 1.5 nm, being well below the electron mean-free path (~ 430 Å for gold⁽²⁴⁾), will not show bulk electron scattering effects. Instead it is expected that the overwhelming majority of electron scattering events are associated with the surface potential.

Figure 3.6 compares the experimentally observed quenching efficiencies of a 1.5 nm NP as measured by PL and calculated using Eqn. 3.3 and also as measured by luminescence lifetime using Eqn. 4.6. A theoretical curve calculated using Eqn. 3.8 is overlaid for comparison to theory.

Although Eqns. 3.6 and 3.7 use bulk gold parameters, the model fits surprisingly well with the experimentally measured values, and particularly with the rates of energy transfer reported in Table 3.1. The photoluminescence characterization seems to overestimate slightly the theoretical quenching values, whereas the lifetimes are in excellent agreement with the model. Because the measurement of relative quantum efficiencies via PL spectra is prone to error in the form of fluctuations in lamp intensity or the ability to accurately measure absorption, the PL quenching efficiencies are considered less reliable than lifetime measurements. Fluorescence lifetimes avoid the accumulated error associated with the use of multiple instruments, which increases our confidence in their measurement. Lifetimes are very sensitive to the presence of quenching processes and give insight into the number of quenching processes taking place. The lifetimes measured here not only suggest that quenching is occurring due to a single energy transfer event, (decreased single-exponential lifetime), but also suggest that the *slope* of the theoretical curve may be correct.

The absorption characteristics of gold NP's have been studied extensively and attempts to fit theory with experimental data have furnished a rich description of the electronic and optical properties of metal NP's. Attempts to model the absorption for gold NP's below 20 nm diameter, in particular the bandwidth and position of the SPR band, requires the incorporation of an enhanced surface potential scattering term in the Drude dipole approximation.^(12; 25) Whetten was successful in adapting this model to calculate the absorption spectra of gold NP's from $d = 1.4 - 3.2$ nm where they advance the theory that thiol ligands donate electron density into the NP.⁽¹³⁾ In this regard, the use of NP's as energy acceptors may actually enhance the quenching efficiency of a metal surface and explain the somewhat unexpected efficiency of quenching by a 1.5 nm NP. The increased

electron density and surface scattering enhances the probability of energy transfer via the Persson model, accounting for the good agreement between the data shown here and the theoretical model.

3.4.2 Monitoring k_r

The observed quenching behavior of a molecular dye at a specified distance above a metal surface has been explained previously by a perturbed radiative rate.⁽³⁷⁾ Neither lifetime nor PL data alone will give evidence toward the true origin of the observed quenching because both can be explained by either the radiative rate or energy transfer models. An absorption experiment, however, will give insight toward the origins of this quenching phenomenon.

Exclusion of the possibility of radiative rate (k_r) changes is garnered by considering the changes in the absorption intensity or oscillator strength (f) for the dye molecule upon binding the gold NP, since $k_r \propto f$.⁽⁵¹⁾ The transition probability between states by the Einstein A_{21} and B_{12} coefficients relates the experimental absorption of an electronic transition to the oscillator strength and radiative rate for that molecule.⁽¹⁵⁾ Oscillator strength, f is directly related to the radiative rate, k_r through the relation:⁽⁵¹⁾

$$k_r^o = 3 \times 10^{-9} \bar{\nu}_o^2 \int \varepsilon d\bar{\nu} \cong \bar{\nu}_o^2 f \quad (3.9)$$

where $\bar{\nu}_o$ is the energy in wavenumbers corresponding to the maximum absorption, and ε is the experimental extinction coefficient. A controlled absorption experiment, therefore, gives the oscillator strength (f) for the dye upon appending the gold NP and is an independent measure of a changing radiative rate. Figure 3.7 shows the absorption for the 15 bp system where the sample absorption (—) has been corrected for scattering at higher wavelengths and the absorptions of dsDNA-dye normalized at A_{260} . Normalization of the difference spectra at 260 nm, which arises predominately from the DNA absorption, allows direct comparison of the oscillator strengths for the FAM and Cy5 dyes at 490 nm and 650 nm, respectively in the absence and the presence of a NP.

If the quenching efficiency shown in Fig. 3.6 were related to changes in the radiative rate, then the experimental oscillator strength would be directly affected. However, changes in the oscillator strength were calculated to be 5-10% which does not account for the observed 50-70% drop in PL intensity, suggesting that the reduced quantum efficiency must be related

to an energy transfer mechanism from the dye to the gold NP and not due to a changing radiative rate for this system.

3.5 Conclusion

In conclusion, three different lengths of dsDNA-dye, using two dyes of different energies were appended to 1.5 nm gold NP's as a means of measuring quenching efficiency of the fluorophore at discrete distances. Absorption data on the fluorophore is forthcoming in proving a mechanism which does not rely upon a changing radiative rate for this system. The quenching was measured by cw-PL and by picosecond lifetime spectroscopy to determine that the process of quenching is an energy transfer event and that it follows a $1/d^4$ distance dependence. The significance of a $1/d^4$ dependence upon energy transfer is realized when using NSET as a molecular ruler, because this means the measureable distance, (≈ 20 nm) via this technique has been extended over 2x further than traditional FRET, (≈ 10 nm.) The discrepancy between quenching efficiencies as measured by PL and lifetimes is most likely error due to instrumental inaccuracy in absorption/photoluminescence measurements.

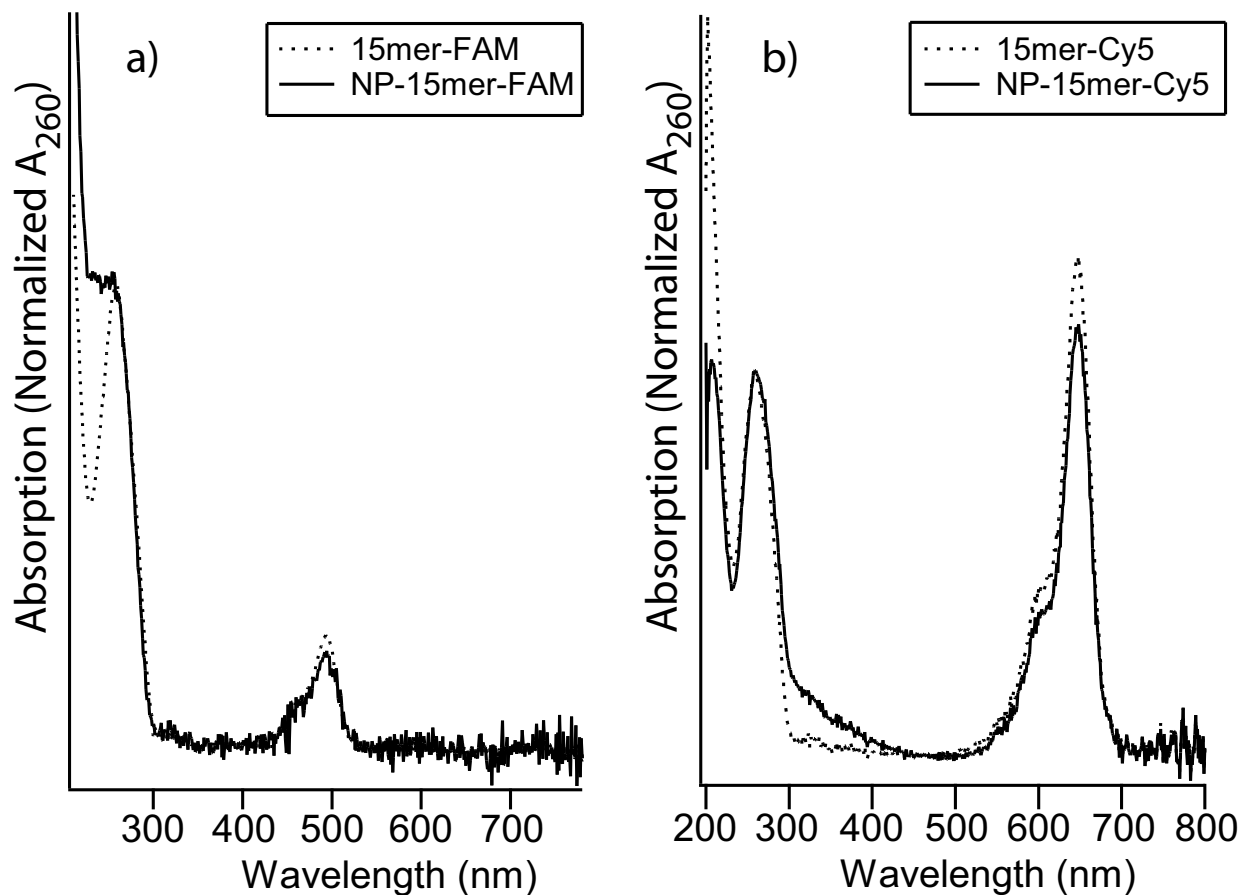


Figure 3.7: Absorption comparison of the dye-15mer (w/o NP, \cdots) to the dye-15mer-NP absorption, after subtracting gold absorption and correcting for scattering ($-$). All absorbances have been normalized at the DNA absorption wavelength, 260 nm. A small scattering correction has been applied to the NP-15mer-FAM absorption to correct the baseline from the 200-450 nm range. Absorption comparison for both FAM-15mer-NP (a) and Cy5-15mer-NP (b) allows direct monitoring of the oscillator strength for the dye at the closest proximity to the gold NP measured here.

CHAPTER 4

NSET AS A FUNCTION OF NANOPARTICLE SIZE

4.1 Introduction

Chapter 3 probed questions relating to the ability of energy to transfer from a molecular dye into a metal surface. The debate over whether or not it is accurate to refer to a NP at 1.5 nm diameter as a “metal” is ongoing(52; 21; 13; 25), however the effect of bringing such a particle into the proximity of an excited dye molecule is clear: the NP affects the quantum efficiency of emission by introducing a competitive rate of energy transfer into the NP. Because the quenching process is most likely a direct result of free electron interactions with the dipole field of the emitter, we realize immediately that by changing various parameters of either the dye or the NP we should be able to “fine tune” the efficiency of NSET. As shown from the NSET rate equation:

$$k_{ET} = 0.225 \frac{c^3}{\omega_{dye}^2 \omega_F k_F d^4} \frac{\Phi_{dye}}{\tau_{dye}} \quad (4.1)$$

the rate of energy transfer is dependent upon properties of the metal (ω_F, k_F) and upon the frequency, quantum yield, and lifetime of the donor dye. Chapter 3 demonstrates that dyes of different energy are still quenched by the same NP with a slight drop in efficiency at the longer wavelengths, as predicted by Eqn. 4.1. We may anticipate that, aside from varying properties associated with the dye, changes to the NP acceptor in terms of metal type, NP shape, or especially size should also have a drastic effect upon the behavior of the system. Figure 4.1 demonstrates the size scale of differently sized gold nanoparticles as compared to DNA. The smallest particle at 1.5 nm, is minimally invasive when considering integration with biological systems, containing ≈ 105 atoms and a Molar Mass of 20,500 g/mol. A 6 nm gold particle, however, is four times larger with ≈ 6700 atoms and a Molar Mass of 1.3×10^6 g/mol. At a diameter of 6 nm, a particle has become the size and mass of a medium

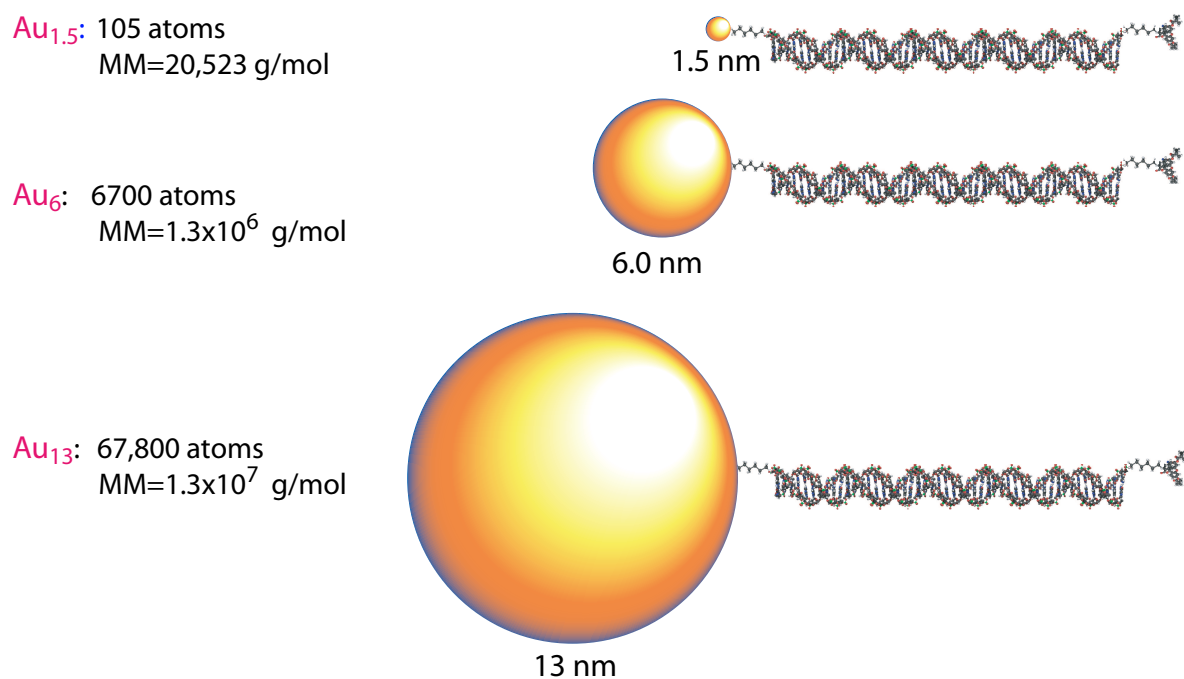


Figure 4.1: Graphic illustration of 45 bp dsDNA (~ 17 nm) appended to gold NP's of various sizes. The 1.5 nm NP is the smallest and least invasive. The 6.0 nm NP is a force to be reckoned with and the 13 nm NP begins to approximate a surface.

sized protein which means that it is no longer a passive observer, but is better considered as a very dense beach ball dominating the movements of any appended bio-molecules. In terms of NSET efficiency, however, the move to 6 nm diameter means significant increase in the density of free electrons and thus its interactions with light. As discussed in chapter 2, nanometal size plays an important role in terms of enhanced density of free electrons, scattering at interfaces and coherent plasmon formation over a diameter of 1.5 nm. As such, the increased density of states and polarizability of such a nanoparticle suggests that it should behave as a much more efficient energy sink for a nearby oscillating electric field.

Considering the same issue from a geometric point of view, the increased cone angle swept out by a 6 nm sphere relative to a point dipole at a fixed distance has also changed drastically, which can be viewed using Förster terminology as an increased dipole projection operator, κ^2 . For example, a point in space at a separation distance of 7 nm (15 bp dsDNA) from a 1.5 nm diameter particle carves out an angle of approximately 24° , (see Fig. 4.2). If the height of the NP changes to 6 nm at the same distance, the angle θ now becomes $\approx 81^\circ$, or an increase of almost four times. At 13 nm diameter, the angle becomes $\approx 124^\circ$, or an increase of 5 times, which is starting to give a good approximation to a planar surface, ($\approx 90^\circ$). Figure 4.2 demonstrates the effect that different NP sizes will have in terms of geometry for a dipole at a fixed separation distance. In this chapter, we will examine the effects that a changing NP size will have upon the efficiency of energy transfer from organic dyes.

4.2 Experimental

4.2.1 Au₆ Nanoparticle Synthesis

Gold nanoparticles with an average diameter of 6 nm (Au₆) were synthesized as described by literature techniques,⁽⁵³⁾ using the controlled reduction of hydrogen tetrachloroaurate (AuCl₄·3 H₂O) in argon-sparged H₂O. Two solutions are prepared in advance: A) 1 mL of 1% HAuCl₄ into 79 mL sparged H₂O. B) 4 mL of 1% sodium citrate plus 1 mL 1% tannic acid solution into 15 mL sparged H₂O. Both solutions were heated to 60°C on the same hot plate, and then under *vigorous* stirring, B was added rapidly to A. The mixture immediately changed colors to a dark wine red and the heat was turned up to bring the contents to a boil. After boiling for ≈ 1 minute, the temperature was dropped and the

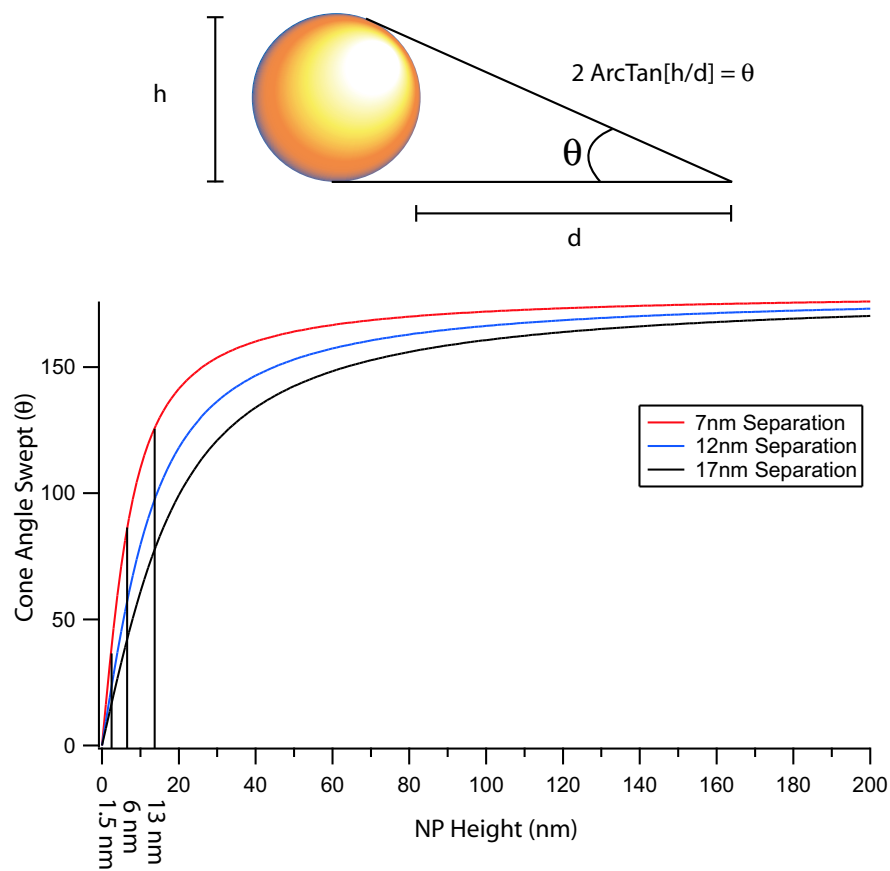


Figure 4.2: NP's of different diameters will sweep out a varying cone angle relative to a fixed point dipole. The effect of NP size on dipole projection can be estimated in this manner. The above calculations were performed for fixed separation distances of 7, 12 and 17 nm, which corresponds to 15, 30, and 45 bp dsDNA spacer lengths, respectively. The cone angles swept out by 1.5, 6, and 13 nm nanoparticles are shown.

mixture was allowed to come to RT. After cooling the synthesis to RT, 500 mg Bis(p-sulfonatophenyl)phenylphosphine dihydrate (SPP) was added to solution to re-cap the citrate as the surface ligand and the mixture was covered and stirred overnight. NOTE: Immediate salting of the citrate-capped Au₆ results in agglomerated particles that will not re-dissolve. For this reason it is better to ligand exchange before salting out.

Purification of the 6 nm colloidal NP's is accomplished by adding dropwise an aqueous solution of 6 M NaCl until the solution begins to turn a dark purple. The salt concentration screens repulsive charge between NP's inducing a Van der Waal's attraction between neighboring particles and causing an aggregation of NP's accompanied by a massive red-shift of the SPR band to lower energy. Once the mixture has begun to precipitate, centrifugation for 1-2 minutes allows easy decanting of the supernatant. Successive precipitations (≥ 3 times) effectively purifies the solution from SPP ligand, which can be qualified based on a strong absorption peak near 290 nm. TEM measurements (Fig. 4.3 displays particles with an average diameter of $6 \text{ nm} \pm 3 \text{ nm}$ as grown via this technique. These particles are stable on the benchtop at ambient conditions indefinitely. Once the NP diameter is known, it is possible to calculate an extinction coefficient by the following equation, which is based upon the empirically obtained relationship published by El-Sayed *et al.*(21):

$$\epsilon(d) = 10^{1.0643 \cdot \text{Log}_{10}[3/2\pi d^3] + 4.0935} \quad (4.2)$$

In this equation, d is the diameter of the gold NP in nanometers and the extinction is given in $\text{M}^{-1} \text{cm}^{-1}$ at the peak of the plasmon resonance, (typically 525 nm). The molar mass for a particle can also be obtained by incorporating the molar volume of gold ($V_m = 10.215 \text{ cm}^3 \text{ mol}^{-1}$) into the geometrical equation:

$$MM_{NP}(d) = \frac{0.5\pi}{3} \frac{N_A \cdot d^3}{V_m} \cdot MM \quad (4.3)$$

where N_A is Avogadro's number, MM is the molar mass of the pure metal element, (Au=197 g/mol), and d is the diameter of the NP in cm. It should be noted that this equation has been expressed in generalized terms and can therefore apply to any pure metal NP. Note also that by using the root form of the equation, one can calculate the number of atoms contained in the particle volume as a function of NP diameter:

$$\text{Atoms}(d) = \frac{0.5\pi}{3} \frac{N_A \cdot d^3}{V_m} \quad (4.4)$$

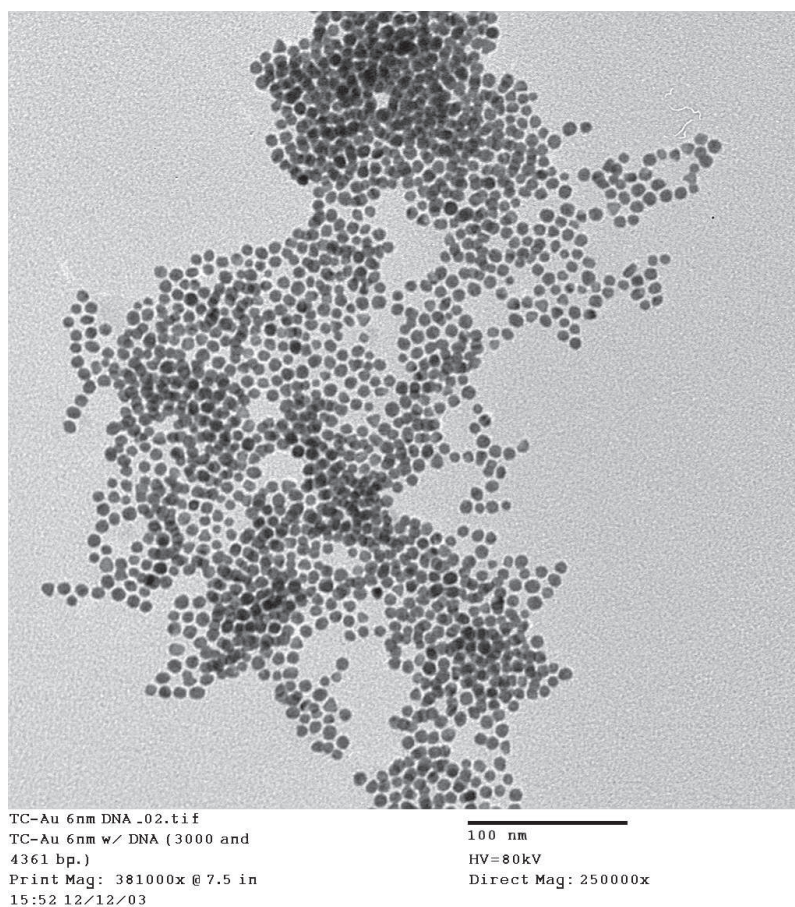


Figure 4.3: TEM image of a synthesis of 6 nm gold NP's. The NP's were synthesized by literature techniques and deposited onto a holey-carbon grid especially prepared for aqueous samples. The average diameter of NP's is $6 \text{ nm} \pm 3 \text{ nm}$.

Using Eqns. 4.2, 4.3, and 4.4 the molar extinction coefficient of Au₆ is $1.97 \times 10^7 \text{ M}^{-1} \text{ cm}^{-1}$, the molar mass is $1.31 \times 10^6 \text{ g/mol}$, and the number of atoms contained within that volume is approximately 6700.

4.2.2 dsDNA - Nanoparticle Coupling:

Complementary DNA strands were purchased with either 5'-C₆-dye or 5'-C₆-SH already HPLC-purified from IDT DNA Technologies. All strands¹ were engineered to minimize secondary structures using mFold.

Coupling of DNA to large NP's is different than the procedure mentioned in Chap. 3 for two main reasons: 1) Because 1:1 stoichiometric coupling results in essentially unmeasurable optical properties for the attached DNA. Also, if the main absorption feature of the dye is at 550 nm or below it is swamped by the massive SPR absorption of the NP centered at 520 nm. 2) Ethanol precipitation does not work for NP's this large; both dsDNA and NP's precipitate out with increased NaCl content and ethanol mole fraction in solution.

For the above reasons, dsDNA was assembled onto 6 nm Au NP's using a 10:1 dsDNA:NP ratio. A standard assembly of double-stranded DNA (dsDNA) with the NP was accomplished by first deprotecting 1 nmol of the single-stranded 5'-SH DNA in 125 μL buffer with 20 μL of 50 mM Tris(2-carboxyethyl)phosphine hydrochloride (TCEP) in 20 mM PBS buffer pH 7.5 at RT for 30 minutes. The freshly deprotected DNA-thiol was desalted with a NAP-5 column and the dye-containing complementary strand (900 pmol) was immediately added. The strands were annealed at 95°C for 2 minutes, cooled to RT for 2 minutes and then added to 50 pmol purified SPP-capped 6 nm NP. The mixture was vortexed and placed at 4°C in the dark for conjugation >24 hours. Purification was accomplished by successive (≥ 3) salt precipitations by adding 6 M NaCl dropwise to solution to induce aggregation, centrifuging at 13,200 rpm 2 minutes, decanting the supernatant, and re-suspending in buffer. The purified dsDNA-NP conjugate was stored in 20 mM PBS pH 7.5 buffer at 4° C in the dark.

¹15dye: 5' Dye-C₆-CGT GTG AAT TCG TGC-3'
15-thiol: 5' C₆S-S-C₆-GCA CGA ATT CAC ACG-3'
30dye: 5' Dye-C₆-CGC CTA CTA CCG AAT TCG ATA GTC ATC AGC-3'
30-thiol: 5' C₆S-S-C₆-GCT GAT GAC TAT CGA ATT CGG TAG TAG GCG-3'
45dye: 5' Dye-C₆-CGT TCC GTG TGC ATA CTG AAT TCC GTG TTA CTC TTG CCA ACC TCG-3'
45-thiol: 5' C₆S-S-C₆-CGA GGT TGG CAA GAG TAA CAC GGA ATT CAG TAT GCA CAC GGA ACG-3'

4.2.3 Absorption/Photoluminescence:

Absorption measurements were acquired on a Varian Cary 50 UV-vis spectrophotometer and photoluminescence measurements were acquired on a Varian Cary Eclipse Fluorescence spectrophotometer using Z-matched 50 μL quartz cuvettes. A typical quantum yield was calculated by measuring the absorption over the 200-800 nm range for both the sample described above and a control (dsDNA-dye without NP), keeping the peak of the dye absorption ≤ 0.1 A.U. Continuous-wave photoluminescence (cw-PL) was first measured on the control strand, adjusting the sensitivity to maximize the PL signal. *Under identical settings* the PL intensity of the dsDNA-NP sample was then measured. Quantum efficiencies of quenching were determined via the following calculation:

$$\Phi_{QEff} = 1 - \frac{I_{sample}}{I_{control}} \cdot \frac{A_{control}}{A_{sample}} \quad (4.5)$$

where Φ_{QEff} is the quantum efficiency of energy transfer, $I_{sample,control}$ is the integrated intensity under the curve for the PL peak, $A_{control}$ is the absorption of the sample at its absorption peak, and A_{sample} is the corrected absorption of the dye after subtracting out the contribution absorbed by the NP.

4.2.4 Lifetime Measurements:

Lifetimes are acquired using the output of a Nd:VO₄-pumped (Spectra-Physics Vanguard, 2 W, 532 nm, 76 MHz, 10 ps) R6G dye laser (Coherent 702-1). Cavity dumping of the dye laser to 1.9 MHz drops the pulse train to 1 pulse every 2 μs . In the case of FAM the laser is frequency doubled for $\lambda_{ex}=300$ nm, used as is tuned to $\lambda_{ex}=560$ nm for TAMRA and to $\lambda_{ex}=600$ nm for Cy5. Samples were excited with <1 μW at a right angle geometry relative to a Chromex 500is 0.5 m imaging monochromator with 50 g/mm grating, 0.5 nm resolution. Output of the monochromator is focused into a Hamamatsu C5680 streak camera operating at 20 ns window (FAM) or 10 ns window (TAMRA, Cy5). Lifetimes are measured by binning intensity vs time for a 20 nm spectral range about the λ_{em} maximum for the dye. Lifetime quenching calculated by:

$$Q_{eff} = 1 - \frac{\tau'}{\tau_0} \quad (4.6)$$

was determined by comparing the measured decay rate for a NP-dsDNA-dye system (τ') vs the observed decay rate for the identical dsDNA-dye in the absence of NP (τ_0).

4.3 Results and Discussion

Binding of DNA to large gold NP's has been accomplished easily in the literature(54; 55) and various methods of medical(56) or bio-molecular(57) optical techniques have been suggested based upon these structures. The research presented here also takes advantage of DNA-NP architectures in examining the optical properties of organic dyes in the proximity of size-controlled metal surfaces.

4.3.1 Degree of Labeling for DNA to Au₆

Quantification of the conjugation efficiency of the dsDNA binding to the metal surface is critical for the further analysis of the optical properties of a reporter dye. The surface area of a 6 nm NP is roughly 450 nm², which means that, assuming a 2 nm diameter for the footprint of a dsDNA strand, approximately 18 dsDNA units could assemble onto the surface of a single NP. However, the surface ligand (SPP) and DNA-DNA steric effects must be taken into account which complicates the problem. Because this study uses 3 different length strands of DNA (15, 30, and 45 bp), the steric interaction as a function of size or dye on the 5' end may come into play when assessing the degree of binding. Figure 4.4 displays the absorptions for the three different strands of DNA onto Au₆. Therefore, by normalizing the absorption spectrum of Au₆ relative to the spectra for DNA-bound Au₆ at a wavelength insignificant to either the DNA or the dye, the contribution to absorption for the Au₆ can be subtracted. While absorption-subtraction technique has further implications toward monitoring changes in the radiative rate of the dye (discussed later in section 4.3.3) here we are only interested in the efficiency of DNA-labeling.

There are two important observations that can be made through inspection of Figure 4.4: 1) Aside from the absorption characteristics in the absorbing region of the dye, the nucleotide absorption region (260 nm) is quite comparable between common lengths of DNA, (15mer-FAM and 15mer-Cy5, for example). This suggests that the different dyes are not affecting the efficiency of DNA labeling to a significant degree. And secondly, 2) the increased absorption

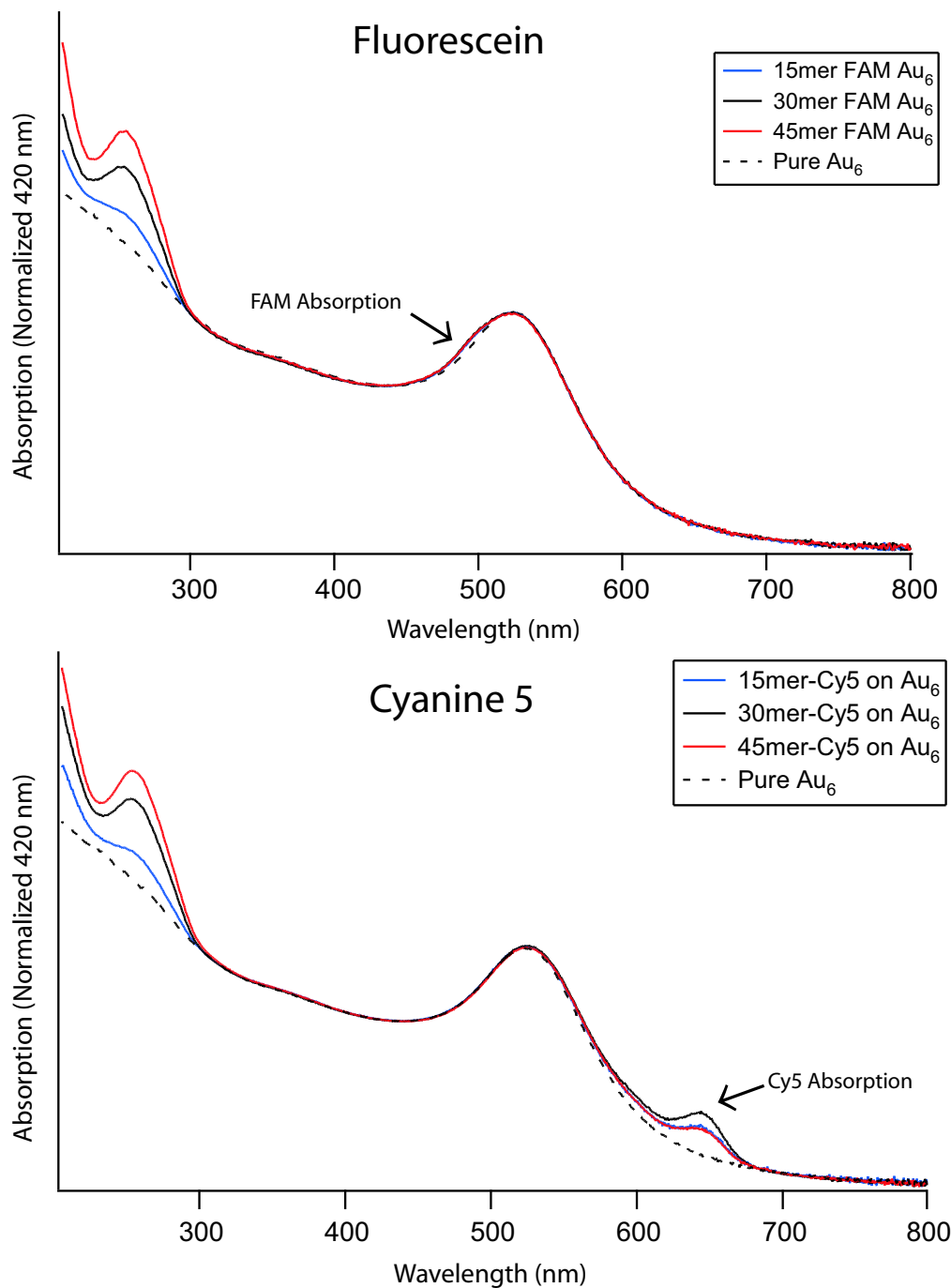


Figure 4.4: *TOP*: Overlaid absorption spectra for FAM-labeled dsDNA bound to 6 nm gold nanoparticles. *BOTTOM*: Overlaid absorption spectra for Cy5-labeled dsDNA bound to 6 nm gold nanoparticles. All absorption data have been normalized at 420 nm for comparison. The DNA absorption at 260 nm increases as the length of the strand moves from 15 bp to 45 bp. The dye absorption (FAM = 490 nm, Cy5 = 647 nm) changes only as a function of its coupling efficiency to the DNA strand.

Table 4.1: Calculated ratios of DNA:Au₆ for 15, 30, and 45 bp dye-dsDNA where the dye is either FAM or Cy5. The starting reaction conditions were 10:1 DNA:Au₆.

	15 bp	30 bp	45 bp
FAM	8.2 ± 2.3	10.4 ± 1.7	10.9 ± 1.3
Cy5	8.2 ± 2.1	11.7 ± 1.5	10.8 ± 1.5

at 260 nm is consistent with the higher extinction coefficient of longer strands of DNA. This suggests that the efficiency of a 15 bp strand binding has not been facilitated or blocked significantly by its shorter size. Table 4.1 shows the calculated ratios of DNA coupling to Au₆ based upon absorptions at 520 nm for the Au and 260 nm for the DNA. The chart shows that the 15 bp system may be a slightly less favorable ligand than the 30 or 45 bp strands due to the consistent 8:1 ratio in both cases, however the difference is within the noise. Understanding that the starting conditions were 10:1 DNA:Au₆, these data show that the binding of thiols to a gold surface is a very efficient reaction with nearly 100% product yield. Because we estimate a maximum coverage of 18 strands of DNA for a 6 nm NP and absorption shows nearly 100% efficiency of binding, we may conclude that the surface has not yet been saturated with dsDNA ligands.

4.3.2 Comparison to SERS

A brief comparison-contrast at this point is helpful in understanding how the subject of fluorophores proximal to metallic colloids may be approached. The photophysical behavior of organic dyes near metal surfaces has been viewed and modeled not only as a function of distance, but has also been compared to its cousin effect, surface-enhanced Raman scattering (SERS). SERS is a phenomenon first noticed by Fleischmann *et al.* in 1974(58) for pyridine adsorbed onto roughened metal electrodes in which the Raman signal had been amplified by 10⁵-10⁶ over predicted calculations. The SERS phenomenon is commonly used for the vibrational characterization of small molecules and has been well-documented when the

“rough” metal surface is modified to be a colloidal nanoparticle.(59; 60; 61; 62; 63) Moskovits describes the SERS effect for the electromagnetic mechanism as the resonant coupling of plasmons to electromagnetic plane waves which must follow the dispersion relation:(18)

$$k_{\parallel}^2 = (\omega/c)^2 Re[\epsilon_0 \epsilon(\epsilon_0 + \epsilon)^{-1}] \quad (4.7)$$

where $\epsilon(\omega)$ is the dielectric function of the metal, ϵ_0 is the dielectric constant of the surrounding medium, and ω is the frequency of the oscillating wave. In the creation of a plasmon by an incident plane wave, both frequency and momentum must be conserved, which is not normally the case for the general range of indices of refraction. However, by making the conductive surface rough, the conditions for the far-field radiation may be relaxed. In this case, Eqn. 4.7 is modified where wavevector matching between the incident wave and the surface plasmon follows k_{\parallel} plus integral multiples of $2\pi/\lambda$, where λ is the periodicity of roughness. A rough surface, therefore, allows a portion of the plasmon’s energy to be radiated instead of being dissipated as heat. Simply put, an emitting dipole very near to a metal surface can excite any order plasmon and “store” the photon energy as a surface plasmon. The $N = 1$ (first order) plasmon has the symmetry of a time-varying dipole and can therefore radiate to the far-field. In this sense, SERS is observed due to the non-linear effects induced upon molecules dependent upon local enhancement of the electromagnetic field near rough conducting surfaces. The fluorescence from dyes adsorbed onto metal surfaces is sometimes enhanced by 1-2 orders of magnitude due to the dye’s ability to directly excite plasmons without breaking momentum conservation laws at these distances. The ability to enhance photoluminescence quantum yields from dyes near metallic nanosurfaces is another field and the primary research of Lakowicz,(19; 64; 65; 66; 67) but will not be elaborated upon here.

Although the true mechanism behind the SERS phenomenon is still under debate and further experimentation is required to gain a deeper understanding, some very interesting research into molecule-colloid interactions has been acquired. Franzen has studied the absorption properties of dye molecules adsorbed onto gold and silver colloidal NP’s near 10 nm diameter in an attempt to explain the relationship between the absorption line-shape and the SERS efficiency.(68) He points out that the additive nature of Beer’s Law in absorption spectroscopy assumes optical homogeneity. However, due to the strength with which colloidal metallic NP’s interact with light, the absorption spectrum of dye-adsorbed NP’s may violate Beer’s Law where the dye may be considered to exist, optically speaking, *inside* the NP. In

this model, the additive nature of dye-NP absorption breaks down as a function of incident light frequency. The plasmon frequency, which typically represents the frequency above which the metal stops to conduct may be considered the energy at which the NP becomes transparent for dye absorption. Therefore at frequencies higher than $\omega_{Fr\ddot{o}lich}$, ($\omega_{Fr\ddot{o}lich} = \omega_p/\sqrt{3}$), the molecule would be free to absorb incident light. At frequencies lower than the plasmon absorption transition, $\omega_{Fr\ddot{o}lich}$, the absorption strength of an adsorbed molecule, especially in the perpendicular orientation, may be diminished by the much higher response of conduction electrons to the electromagnetic field. This tool developed by Franzen, along with the relationship between absorption line strength and the radiative rate as mentioned in Chap. 2 will give valuable insight into the effect of the metal surface on the photosensitivity and photophysics of the donor dye. Note that the electromagnetic mechanism explaining SERS relies upon the enhanced electric field affecting the dye molecule, whereas NSET relies upon the dye molecule first being excited and then affected by the NP.

A contrast should be made at this point in reference to the work discussed in Chap. 3 in which fluorophore properties were investigated in the vicinity of 1.5 nm NP's. Because these particles are below the size where surface plasmons exist, they would not be expected to participate in a SERS event which relies upon the plasmon band and are therefore ruled out of this discussion. The larger 6 nm particles, however, are large enough that they could contribute to either SERS or NSET, depending upon the conditions.

4.3.3 Monitoring Absorption of dyes near Au₆

The electromagnetic enhancement effect, typical to SERS, has been calculated theoretically as a function of distance from the surface of different shaped nanoparticles. Using a silver sphere of radius 20 nm, it was suggested using discrete dipole approximation (DDA) calculations that the enhanced electric field could be significant as far as 30 nm from the surface.⁽⁶⁹⁾ This radius for electromagnetic enhancement could be considered the radius over which molecular dyes respond to the effects of the nanoparticle's presence. Under the Franzen model discussed in section 4.3.2 this could be the radius for absorption masking. Normally, the absorption line strength for a molecule is a constant for a given solvent and the primary contributor to a reduced (or enhanced) photoluminescence intensity is a result of added (or subtracted) non-radiative pathways for the molecule in the excited state. However, because the behavior of a dye near conducting surfaces is an area of hot debate, with many

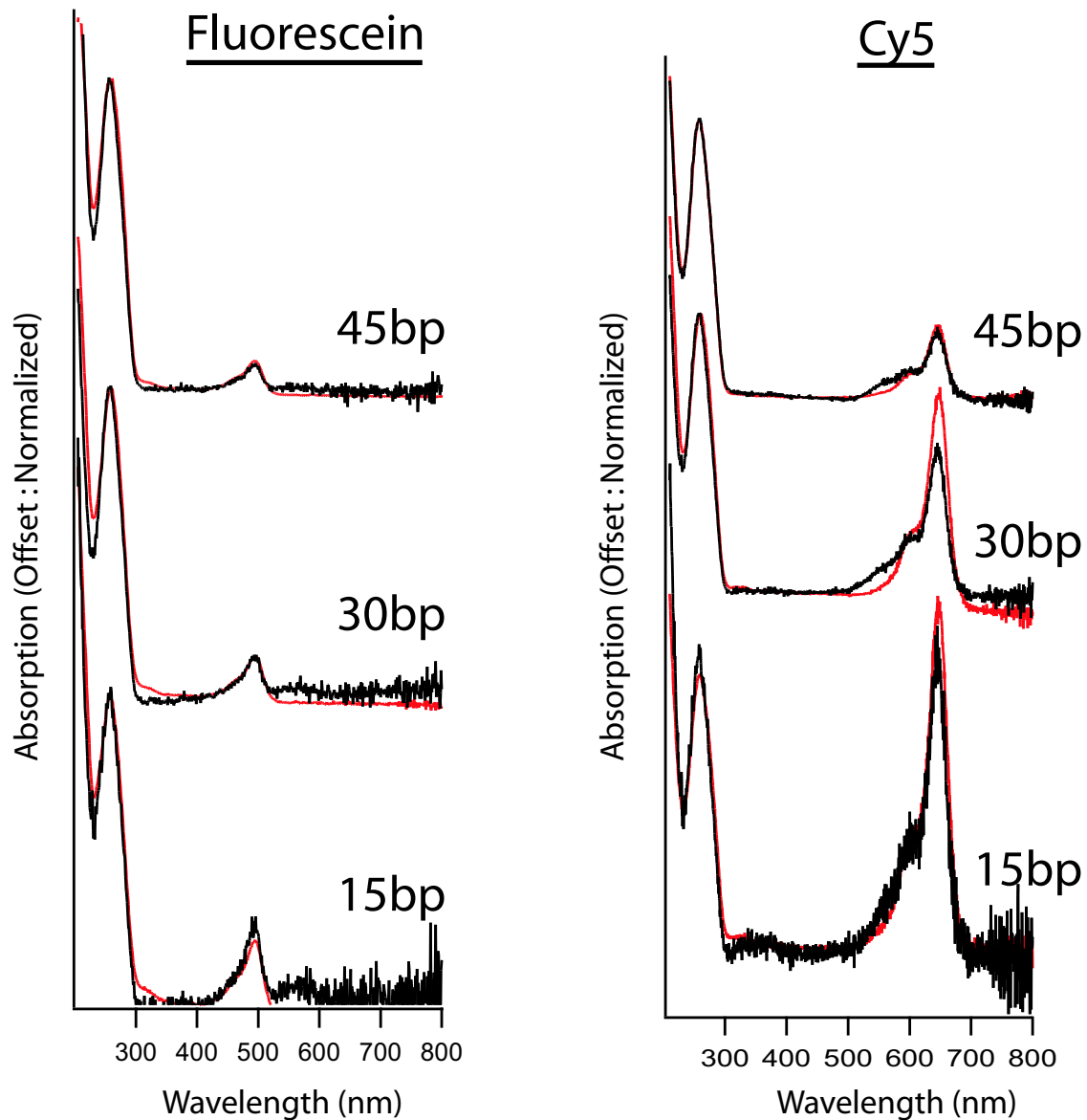


Figure 4.5: *LEFT*: Absorption spectra for the three separate length (15, 30, and 45 bp) FAM-dsDNA samples (black) after subtraction for extinction due to Au₆. The data have all been normalized to the DNA absorption band at 260 nm. *RIGHT*: Absorption spectra for the Cy5-dsDNA samples (black) also normalized at 260 nm. Both FAM and Cy5 samples are compared to absorption spectra of the free dye-dsDNA in the absence of NP, (red). Normalizing at the DNA absorption wavelengths allows a direct comparison of the absorption line strength for each dye in question.

models like those related to the SERS effect, the models of Gersten and Nitzan,(49; 70) or the model of Franzen,(68) the absorptive behavior of a molecule must be carefully controlled. Therefore the dye’s ability to absorb light in the presence of an NP could be a major key to understanding which mechanisms are dominant.

Figure 4.4 showed the absorption spectra of two separate dyes separated from the surface of the NP by three distinct distances using dsDNA as a spacer. The FAM dye has a frequency $\omega_{FAM} > \omega_{Frölich}$ whereas Cy5 has a frequency $\omega_{Cy5} < \omega_{Frölich}$, which is a convenient way of testing Franzen’s theory as applied to our system. Figure 4.5 compares the subtracted dye-dsDNA absorption spectra from Fig. 4.4 to an absorption spectrum of the same DNA strand free in solution. All spectra in this case have been normalized at 260 nm where the extinction arises primarily from DNA absorption. This is useful as an internal calibration to compare the absorption strength of the dye when in the presence (black) and in the absence (red) of a 6 nm NP. Within some error, inspection of the absorption data for each sample, in the cases of either FAM or Cy5, demonstrates that the absorption line strength for each dye is essentially unchanging, even at the closest distance of ~ 7 nm (15 bp). The suggestion that both the DNA and dye absorption strengths are being affected evenly can be ruled out because the FAM dipole oscillating at high frequency should be nearly transparent to the gold’s $\omega_{Frölich}$.

The implications of these absorption spectra are twofold: 1) The gold NP is not masking the absorption of the dyes, and so the dyes must be distanced far enough from the surface of the NP that the strong interaction of the gold conduction electrons with incident lightwaves has not negated the dye’s ability to absorb. 2) The oscillator strengths of each dye being unchanged suggests that, according to the relation between the Einstein A and B coefficients (Chap. 2) the spontaneous emission probability (k_r) is also unchanging. This leaves any changes in lifetime to be a sole function of the efficiency of energy transfer into the NP.

4.3.4 Photoluminescence and Lifetimes of Dyes Near Au₆

The quantitative optical characterization of a dye molecule luminescence can be expressed in the concept of a quantum yield. A quantum yield, often paraphrased as “photons in divided by photons out,” is a relation between the ability of a molecule to absorb light and its ability to release that stored energy as another photon of light, (always at slightly lower energy). This statement implies that not only the measured photoluminescence intensity for

a dye, but also the dye’s ability to absorb light must be measured to accurately determine a quantum yield.

A true quantum yield measure using an integrating sphere will do just this; it will deliver a calibrated amount of electromagnetic energy to an absorbing sample and monitor the amount of energy returned as light. A similar measurement may also be performed, in the absence of an integrating sphere, using a *relative* sample of known quantum yield. The first method of characterizing the efficiency of dye molecules near 6 nm gold spheres is measuring the efficiency of the dye relative to a standard. In these experiments we have a fortunate choice for the standard quantum yield, which is the *identical* sample, only in the absence of a quenching NP.

Because, as was shown in Fig. 4.5, neither the oscillator strength of the dye nor the absorption cross-section have been altered by the enhanced electric field of the NP, we can be sure that there are no non-linear effects taking place and the relative quantum yield determination is as simple as taking the absorption-PL measurements to compare both sample and control according to Eqn. 4.5. Figure 4.6 shows the photoluminescence intensities for both FAM and Cy5, where the intensity of the sample has already been adjusted to account for absorption from the NP. This is accomplished by taking the absorption spectra after subtracting the NP absorption (Fig. 4.5) and comparing an average of 5 data points at the peak (490 nm - FAM; 648 nm - Cy5) and multiplying this ratio by the entire PL signal. The overlaid plot shows the integrated PL intensity as a function of wavelength, where the end value represents the total integrated intensity for the entire curve. By exciting at wavelengths higher in energy than the onset of photoluminescence we are able to capture the entire spectrum without contributions from the excitation source.

When inspecting Fig. 4.6 the photoluminescence intensity is strongly quenched at short distances and follows an expected trend that longer separation distances quench the fluorophore less. Comparison of the photoluminescence quenching found in these systems to those shown in Chap. 3 demonstrates a greatly increased efficiency of energy transfer in the case involving a 6 nm particle. The photoluminescence intensity of the furthest distance measured using the 6 nm particle (45 bp - 169 Å) is indicative of a molecule which is 40 - 50% quenched. This is the quenching efficiency of the *shortest* separation distance measured in the $d = 1.5$ nm NP case. However, to discuss the quenching phenomenon, its origins, and the effects that NP size plays upon the system in terms of geometry, we must first finish the

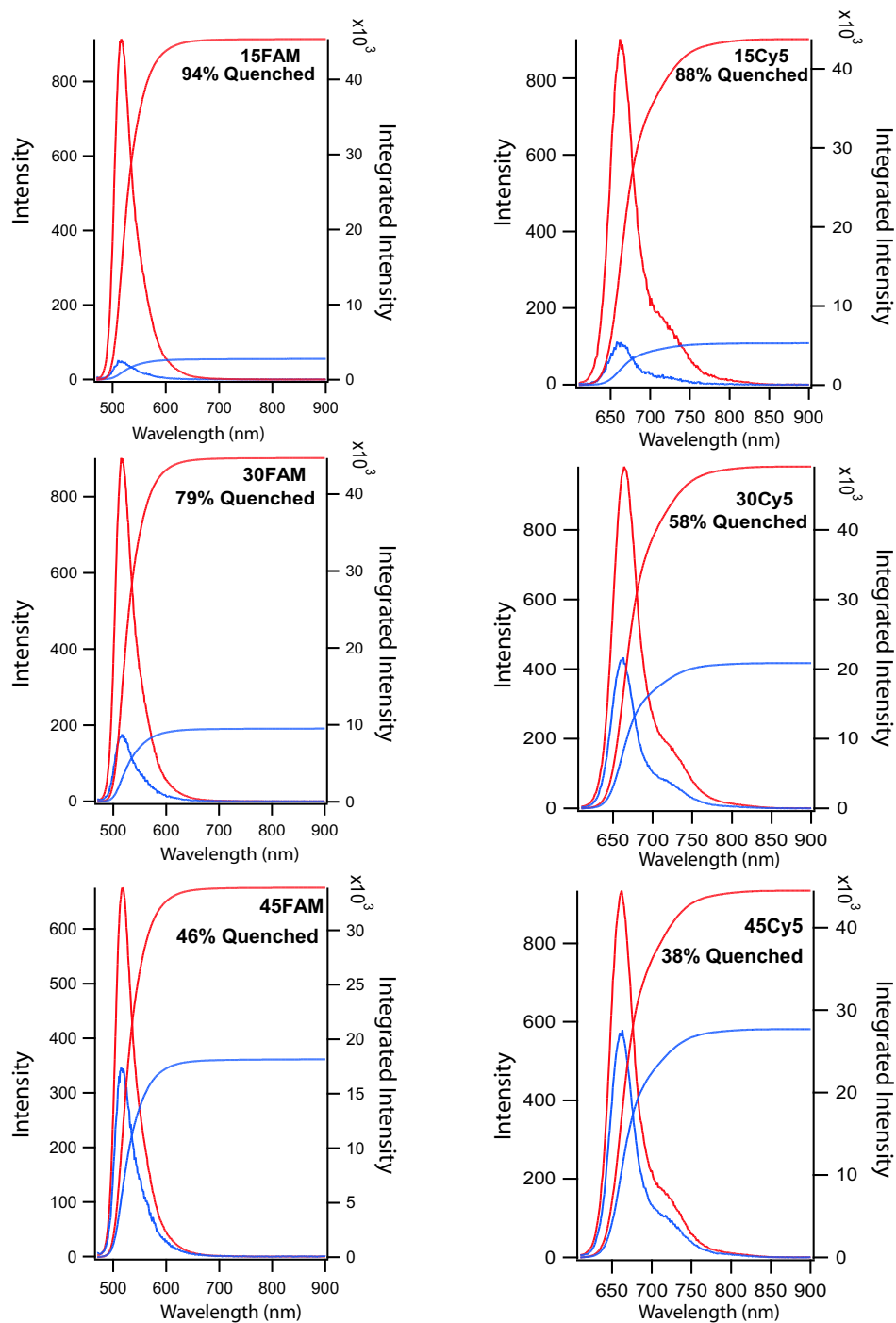


Figure 4.6: *LEFT*: Photoluminescence spectra of FAM-dsDNA at separation distances of 69, 120, and 169 Å (15, 30, and 45 bp, respectively) from the surface of a 6 nm NP. *RIGHT*: Photoluminescence spectra for Cy5 separated from the 6 nm NP by the same distances. The integrated intensity for each curve is overlaid on top of each graph as a function of wavelength from left to right.

optical characterization through inspection of fluorescent lifetimes.

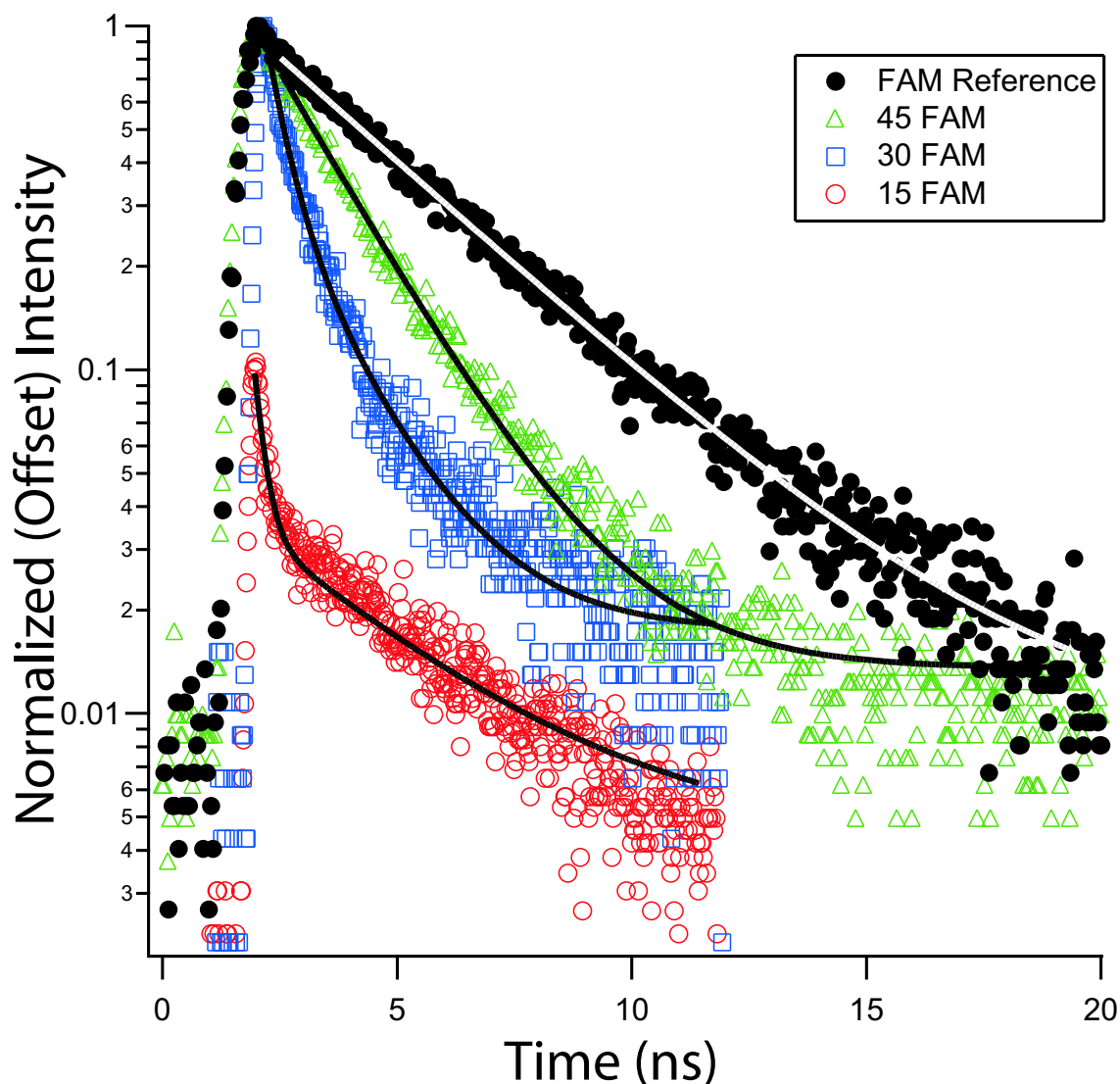


Figure 4.7: Luminescent lifetimes of FAM-dsDNA at separation distances of 69, 120, and 169 Å (15, 30, and 45bp, respectively) from the surface of a 6 nm NP. Although the quenching efficiency at each distance is calculated relative to an identical sample without NP, here we show only one representative control lifetime of FAM (15mer-FAM control strand) for comparison.

The lifetimes for FAM are displayed in Fig. 4.7 and for Cy5 in Fig. 4.8. All lifetimes have been vertically offset and are shown relative to a representative control lifetime for the dye in question. Once again, the trend is clear that as a function of separation distance to

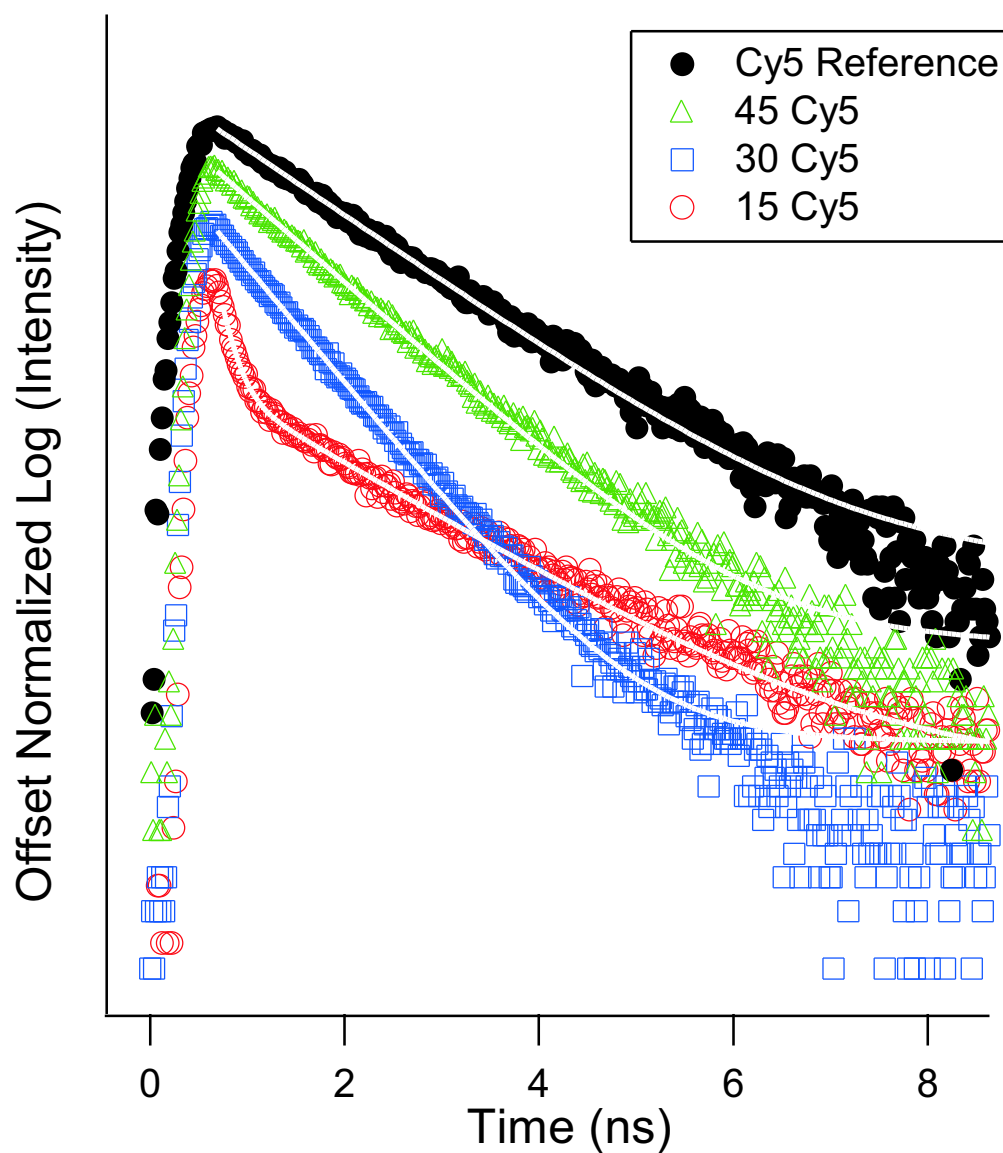


Figure 4.8: Luminescent lifetimes of Cy5-dsDNA at separation distances of 69, 120, and 169 Å (15, 30, and 45bp, respectively) from the surface of a 6 nm NP. Although the quenching efficiency at each distance is calculated relative to an identical sample without NP, here we show only one representative control lifetime of Cy5 (15mer-Cy5 control strand) for comparison.

the surface of the NP, the decay rate changes in a predictable manner. At short distances a very fast rate of decay is observed, which lengthens considerably at the longest distance measured. The reasons for the quenched lifetime can be easily explained through the equation $k_{obs} = k_r + k_{nr} + k_{et}$, which was discussed in Chap. 2. The assumption that the radiative rate is unchanging, which is supported in the absorption data shown earlier, suggests that the only possible changing parameter will be the increased contributions from k_{et} as the dye moves to close proximity of the metal surface.

The observed lifetime of the 15 bp system is quite obviously multi-exponential for both the FAM and the Cy5 measurements. The data have been fit to a bi-exponential function of the form:

$$I(t) = y_0 + I_1 e^{-k_1 t} + I_2 e^{-k_2 t} \quad (4.8)$$

where the intensity as a function of time is related to a linear offset, y_0 plus a two exponential terms including the decay rate constants, k_1 and k_2 weighted by pre-exponential factors, I_1 and I_2 . The fitting allows the deconvolution of both decay rates and yields values that we may use to interpret a physical meaning.

For example, fitting of the FAM-15mer-NP sample shown in Fig. 4.7 to a bi-exponential function gives two lifetimes, τ_{fast} =290 ps and τ_{slow} = 3.4 ns. Comparison with an unperturbed FAM dye on the 5' end of a strand of dsDNA which also has a lifetime of 3.5 ns at pH 7.5, suggests that the slow component of the sample lifetime is the result of some concentration of unperturbed dye molecules in solution. The best explanation for the observation of the 3.5 ns decay rate is that some concentration of *unbound* FAM-dsDNA is found in solution, either as a result of incomplete purification or some equilibrium of dsDNA ligand exchange with the solvent. Luckily, further information beyond the rates of decay may also be extracted from a lifetime measurement.

Equation 4.8 also fits the pre-exponential terms for each decay process which is essentially the relative contribution of each rate to the total signal observed. Therefore, by normalizing and taking the fraction of each pre-exponential term, one can calculate the relative population of bound to unbound dsDNA in solution using the following: $Contribution_1 = I_1/(I_1 + I_2)$. By doing this calculation, we also realize that the contribution to the total intensity under the lifetime is largely ($\sim 67\%$) related to the bound state. The reason that the unbound dye-dsDNA signal exists visibly in the 15mer and is essentially non-existent in the signal for the

45mer is best explained by the relative intensities of these two systems. The intensity of the dye-15mer, being $\sim 90\%$ quenched, means that a good lifetime measurement will require a long period of photon counting for this sample. The intensity of an unquenched population of dye molecules, therefore, will contribute a significant amount to the total signal and become visible. When the photoluminescence efficiency of the bound dye is increased by displacement to further separation distances from the surface, however, the contribution of counts from unbound dye-dsDNA will be “swamped out” by the much higher signal.

Table 4.2 lists the quenching efficiencies based upon photoluminescence and based upon lifetimes for three dyes (FAM, TAMRA, and Cy5) at the DNA separation distances mentioned. The TAMRA dye was only measured on the 15 bp and 45 bp strands, as shown in the table. As a result of strongly biexponential luminescence decay regardless of proximal quencher, the fitting for TAMRA is not shown or discussed in detail.

The theories of Persson and Lang,(35) Chance, Prock and Silbey,(29) and Kuhn(48) all agree that energy transfer from a point dipole to a planar surface will follow a $1/d^4$ dependence, and that energy transfer to a volume will follow a $1/d^3$ distance dependence. The enhanced energy transfer to a 6 nm NP over the 1.5 nm NP suggests one of two possibilities: either the d_0 value has been extended to nearly 17 nm, or the mechanism of energy transfer has changed. At a NP diameter of only 6 nm, the particle size is still much smaller than the mean-free electron path for gold, suggesting that these materials are still too small to exhibit bulk-like electron-scattering events. This would rule out the d^{-3} dependence under the Persson model in which the transition from d^{-4} to d^{-3} depends upon the introduction of bulk scattering processes. Therefore, we predict that the enhanced efficiency of energy transfer is primarily the product of an increased d_0 value.

Hans Kuhn advanced a theory regarding energy transfer to planes of dipoles, (either a metal surface or a film of dipole acceptors), where energy transfer is treated in a very simple manner.(48) The basis of Kuhn’s model assumes the acceptor to be an absorbing body in the field of the emitter dipole where the power absorbed is proportional to the square of the amplitude of the oscillating electric field. Chance, Prock, and Silbey(29) realized the power of such a simple model and extended the theory to account for optical constants of the absorbing media, ie. n , k , ϵ_1 , and ϵ_2 . The final form for calculating the 50% quenching

Table 4.2: Measured lifetime values for Fluorescein, TAMRA, and Cy5 dyes at separation distances of 69, 120, and 168 ± 5 Å. Also reported are the measured rates of energy transfer into the NP. All measurements are recorded from 5' dye-labeled dsDNA in 20 mM PBS solution pH 7.5.

	dsDNA Strand: Distance(± 5 Å):	15bp 69 Å	30bp 120 Å	45bp 167 Å
FAM[†]	Native Lifetime (ns)	3.53 \pm 0.1		
	Quenched Lifetime (ns)	l = (33%) 3.4 ± 0.5 s = (67%) 0.29 ± 0.05	0.44 ± 0.10	1.83 ± 0.11
	Quenching Efficiency	0.92 ± 0.09	0.87 ± 0.08	0.48 ± 0.09
	Energy Transfer Rate, $k_{et}s^{-1}$	$4.33 \times 10^9 \pm 2.22 \times 10^7$	$1.98 \times 10^9 \pm 5.6 \times 10^7$	$2.8 \times 10^8 \pm 1.1 \times 10^7$
TAMRA[‡]	Native Lifetime (ns)	l = 2.13 \pm 0.11; s = 0.43 \pm 0.06		
	Quenched Lifetime (ns)	l = 2.15 ± 0.14 s = 0.17 ± 0.08		l = 1.17 ± 0.05 s = 0.33 ± 0.04
	Quenching Efficiency	l = 0.03 ± 0.2 s = 0.64 ± 0.05		l = 0.43 ± 0.08 s = 0.13 ± 0.04
	Energy Transfer Rate, $k_{et}s^{-1}$	l = 0 s = $3.53 \times 10^9 \pm 2.71 \times 10^7$		l = $3.84 \times 10^8 \pm 3.7 \times 10^8$ s = $6.77 \times 10^8 \pm 3.2 \times 10^7$
Cy5	Native Lifetime (ns)	1.30 \pm 0.1		
	Quenched Lifetime (ns)	0.139 ± 0.04	0.715 ± 0.04	0.97 ± 0.05
	Quenching Efficiency	0.90 ± 0.05	0.43 ± 0.04	0.22 ± 0.04
	Energy Transfer Rate, $k_{et}s^{-1}$	$6.43 \times 10^9 \pm 1.1 \times 10^8$	$6.29 \times 10^8 \pm 1.1 \times 10^8$	$2.62 \times 10^8 \pm 1.1 \times 10^8$

[†] The shortest distance, FAM-15mer-NP, displayed bi-exponential behavior and was fit to a double-exponential decay.

[‡] TAMRA always displayed bi-exponential behavior for these experiments with 2 components to the lifetime, (l = long; s = short).

value is:

$$d_0 = \frac{\alpha\lambda}{n_1}(Aq)^{1/4} \left[\frac{n_2}{2n_1} \left(1 + \frac{\epsilon_1^2}{|\epsilon_2|^2} \right) \right]^{1/4} \quad (4.9)$$

and A is the absorbance of the layer, given by:

$$A = \frac{4\pi\kappa_2 d_2}{\lambda} \quad (4.10)$$

In Eqn. 4.9, λ is the wavelength of emission for the donor, q is the quantum yield of the emitter (this meaning is somewhat under dispute), $\alpha = (1/4\pi)(9)^{1/4}$ for a perpendicular dipole and $(1/4\pi)(9/2)^{1/4}$ for a parallel dipole. The term d_2 in the absorption equation is the thickness of the absorbing layer. Conceptually this is very simple and could be useful in calculating energy transfer from a dye molecule when we are concerned about NP size because the absorbing film thickness, which could be construed as NP diameter, is inherent to the model calculations. To adjust these equations and relate them to a metallic nanoparticle, certain terms need to be changed.

The distance in Eqn. 4.10 uses d_2 as the thickness of the layer, which can be considered as the thickness of a nanoparticle. Also, we know that geometrically the total quenching rate will be proportional to $1/3 k_{\perp}$ and $2/3 k_{\parallel}$, which should be reflected in the final equation. Finally, as demonstrated in Chap. 2, metals below the mean-free electron path begin to alter their response to light, reflected by the adjusted dielectric constants. The final form for calculating a d_0 value to a NP under Kuhn and the CPS model looks like:

$$d_0 = \frac{1}{3} \left[\frac{1}{4\pi} (9)^{1/4} \frac{\lambda}{n_1} (A_{NP}q)^{1/4} \left[\frac{n_2}{2n_1} \left(1 + \frac{\epsilon_{1NP}^2}{|\epsilon_{2NP}|^2} \right) \right]^{1/4} \right] \dots \quad (4.11)$$

$$\dots + \frac{2}{3} \left[\frac{1}{4\pi} \left(\frac{9}{2} \right)^{1/4} \frac{\lambda}{n_1} (A_{NP}q)^{1/4} \left[\frac{n_2}{2n_1} \left(1 + \frac{\epsilon_{1NP}^2}{|\epsilon_{2NP}|^2} \right) \right]^{1/4} \right]$$

where λ is calculated in nm, and the diameter of the NP is also calculated in nm. The final result will therefore be given in nm. (Details of this calculation are given in Appendix B.) For a 6 nm NP quenching the emission of FAM, using the values: $\lambda = 518$ nm, $d_2 = 6$ nm, $q = 0.8$, $n_1 = 1.5$, $n_2 = 0.62$, $\epsilon_1 = -5.12$, and $\epsilon_2 = 6.85$ calculates a d_0 of 20.6 nm.

The quenching data listed in Table 4.2 are plotted in Fig. 4.9 for FAM and Cy5 as a function of distance vs the theoretical lines calculated using the Persson model (black) and the CPS-Kuhn model (red). The most marked contrast between the results shown here vs the results of Chap. 3 is the greatly increased efficiency of quenching by the larger 6 nm particle.

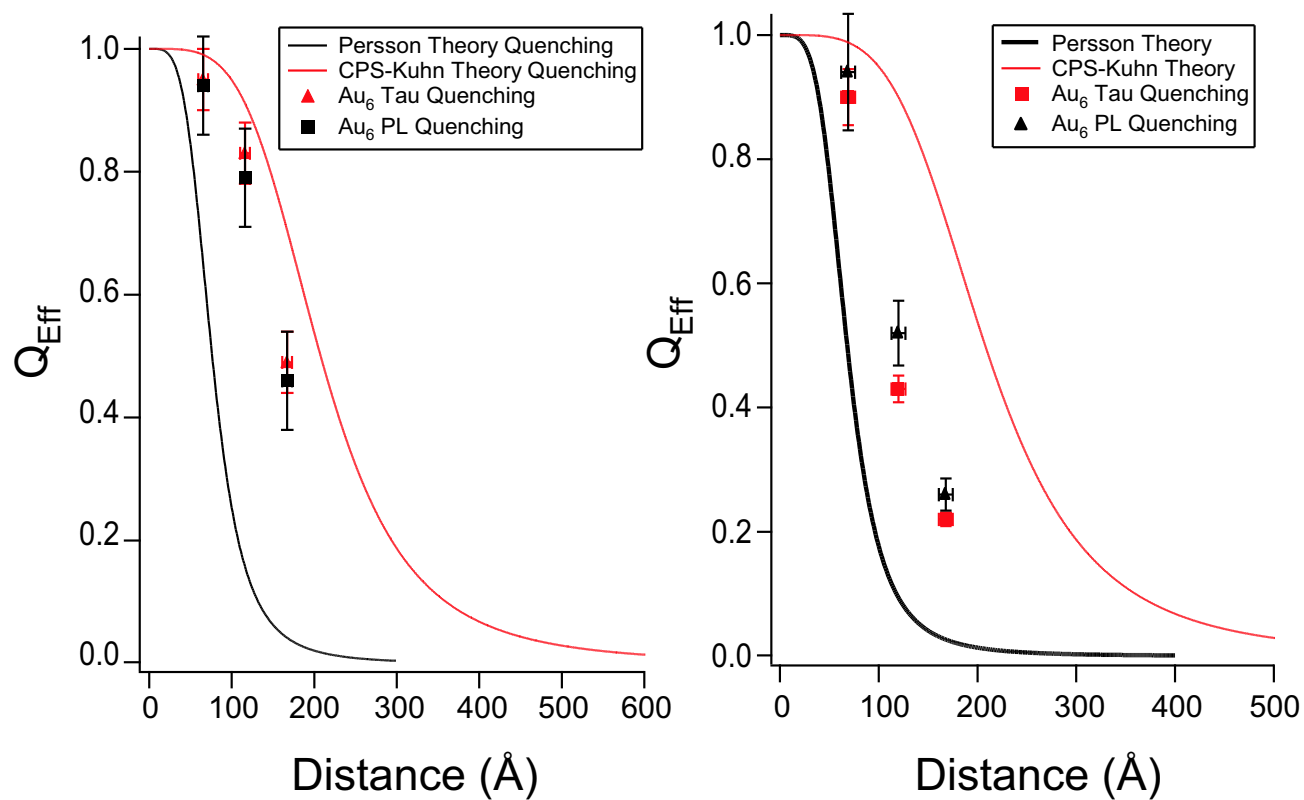


Figure 4.9: Luminescence intensity and luminescence lifetime quenching of both FAM (*Left*) and Cy5 (*Right*) as a function of distance to the surface of a 6 nm gold NP. Data are compared to the NSET efficiency curve as discussed in Chap. 3.

In the case of both dyes, the experimentally measured 50% quenching value is somewhere near the 45 bp distance (~ 17 nm). This seems to be over-predicted by the CPS-Kuhn model, but under-predicted by the Persson-Lang model. From a strictly dimensional argument, if we assume that the majority of dipole projections are parallel to the surface, which becomes a good assumption at longer and longer distances, then the d_0 value calculated only for the k_{\parallel} case becomes 19.7 nm and the theory is a closer match to experimental data.

Attempts to model the cone-angle dependence, as diagrammed in Fig. 4.2 as a function of distance, using a modified quenching efficiency of the form:

$$Q_{Eff}(d) = \frac{2 \cdot \arctan\left(\frac{r}{d}\right)}{\lim_{r \rightarrow \infty} 2 \cdot \arctan\left(\frac{r}{d}\right)} \left(\frac{1}{1 + \left(\frac{d}{d_0}\right)^4} \right) \quad (4.12)$$

where r is the particle radius would account for the cone-angle sweep, but predicts a quenching efficiency that goes to 50% near 6 nm separation distance. This means that geometry corrections as applied to the CPS-Kuhn model cannot account for the slightly lower observed efficiency when considering distances and cone angles. The last geometry argument to invoke may originate in the flexibility of the C_6 -linkers used to attach the DNA to the NP.

For a nanoparticle of diameter 1.5 nm, the flexibility of the organic linkers connecting the DNA to the NP were considered insignificant. This is a good assumption because a shift in the C_6 -chain would result in very slight changes in distance to the organic dye. However, as Fig. 4.10 illustrates, when the NP has grown to 6 nm in size, a shift in the conformation of the C_6 -chain could bring one surface of the much larger NP closer in distance to the emitting molecule. In fact, even though the ligand, SPP, is negatively charged and should repel the negative phosphate backbone of the DNA, the surface of the gold particle is likely to be positively charged due to the oxidation state of gold(I). This is a driving force for the association of DNA to the gold surface, or at least a pre-disposition to move in that direction, which would indeed bring the dye into closer proximity of the NP surface. Such a model could help to explain the increased dye-quenching observed at a predicted distance by changing the actual separation distance by an estimated ~ 3 -6 nm.

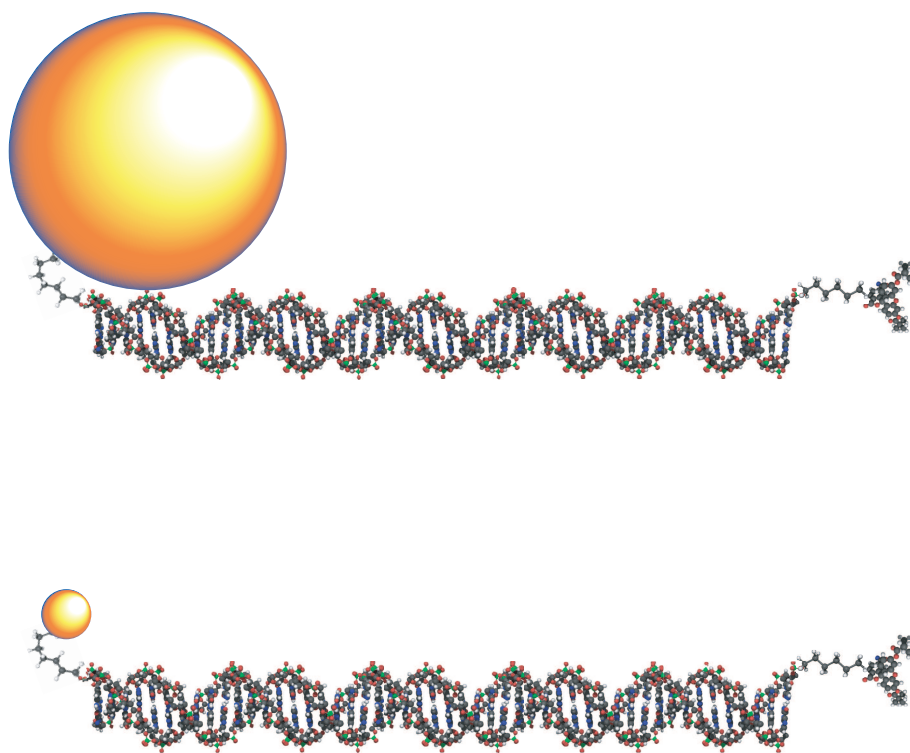


Figure 4.10: Illustration of a 6 nm NP associating with the negatively charged DNA backbone (*Top*) and a 1.5 nm NP associating with the backbone. Because of the NP size, the distance from the dye to the surface of a 6 nm NP would be vastly different than in the case of the 1.5 nm NP (*Bottom*) if the particle associates with the backbone.

4.4 Conclusion

We have shown that the binding of dsDNA-dye ligands to large gold NP's is an efficient reaction with a binding yield of nearly 100% regardless of dsDNA length or dye type. At these 10:1 ratios of DNA:NP, the absorption bands of both the DNA and the dye are measurable and can be separated from the NP absorption to compare not only binding ratios, but also the oscillator strength of the dye as it nears the enhanced electric field of the NP. The oscillator strengths of both FAM and Cy5 are unchanging at the spacer distances measured here, suggesting that the radiative rates are also unchanging. Photoluminescence and lifetime measurements are both supportive and in excellent agreement with each other for a dye with a quenched electronic excited state. The rates of energy transfer are much greater when using a 6 nm NP than when using a 1.5 nm NP, suggesting an enhanced energy transfer mechanism. The modeling proposed by Kuhn, which takes into account the uptake of energy by an absorbing body within the field of the emitter, gives more realistic values for d_0 but over-estimates the degree of quenching. Massaging the Q_{Eff} equation to consider distance-dependent geometry also does not predict the correct quenching behavior. The best fit of experimentally calculated quenching efficiencies to a theoretical model is supplied by considering the flexibility of the C_6 -linkers and the induced change upon separation distance for such a large NP. The larger the NP, the less predictable is the distance to the surface when using DNA as a spacer. For confidence in spacer distance from the larger NP sizes, the best technique to measure the optical properties of dyes may be an inert, non-conducting shell of variable thickness to which dye molecules may electrostatically adsorb or be chemically bound through short organic spacers.

CHAPTER 5

NSET ANALYSIS OF HAMMERHEAD CATALYSIS

5.1 Single-Dye Hammerhead Introduction

Use of nanomaterials, including both metals and semiconductor nanomaterials, has recently gained momentum as a revolutionary technology in biology and medicine for cellular imaging,(71; 72) disease state detection,(73; 7; 6) immunoassays,(74; 75) molecular beacons,(76; 77) and dynamics of protein-nucleic acid interactions.(42) Gold nanoparticles are bio-compatible, have no negative impact on function of the system under study, and can be used for optical characterization of sub-nanomolar samples.(42) Molecular beacons and optical molecular rulers are routinely used to report changes in the distance between a luminescent donor and an acceptor tagged on specific sites of a bio-moiety via Förster resonance energy transfer (FRET). Similar probes using gold nanoparticle acceptors have detected single base pair mismatches in DNA.(77) Recently, we have adapted this methodology for probing dynamic changes in distances for protein interactions on DNA using a molecular ruler approach called nano surface energy transfer (NSET).(42)

The biocompatibility of NSET molecular beacon techniques allows application to a wide range of complex biological systems that require real time dynamics to observe intermediate states, or exhibit fast time-scale kinetics, such as ribozyme substrate interactions. The work of Altman(78) and Cech(79; 80) in the early 1980's demonstrated that certain RNA sequences were capable of complex catalysis in the form of RNA splicing mechanisms. The popularity of studying the catalytic mechanism associated with ribozymes stems from their potential for use as powerful gene expression(81) and viral therapy agents.(82) The hammerhead ribozyme (Fig. 5.1) is a naturally occurring motif of RNA capable of catalyzing its own removal from a longer sequence. The catalysis is Mg^{2+} dependent and undergoes a conformational change to initiate cleavage of the substrate.(83; 84)

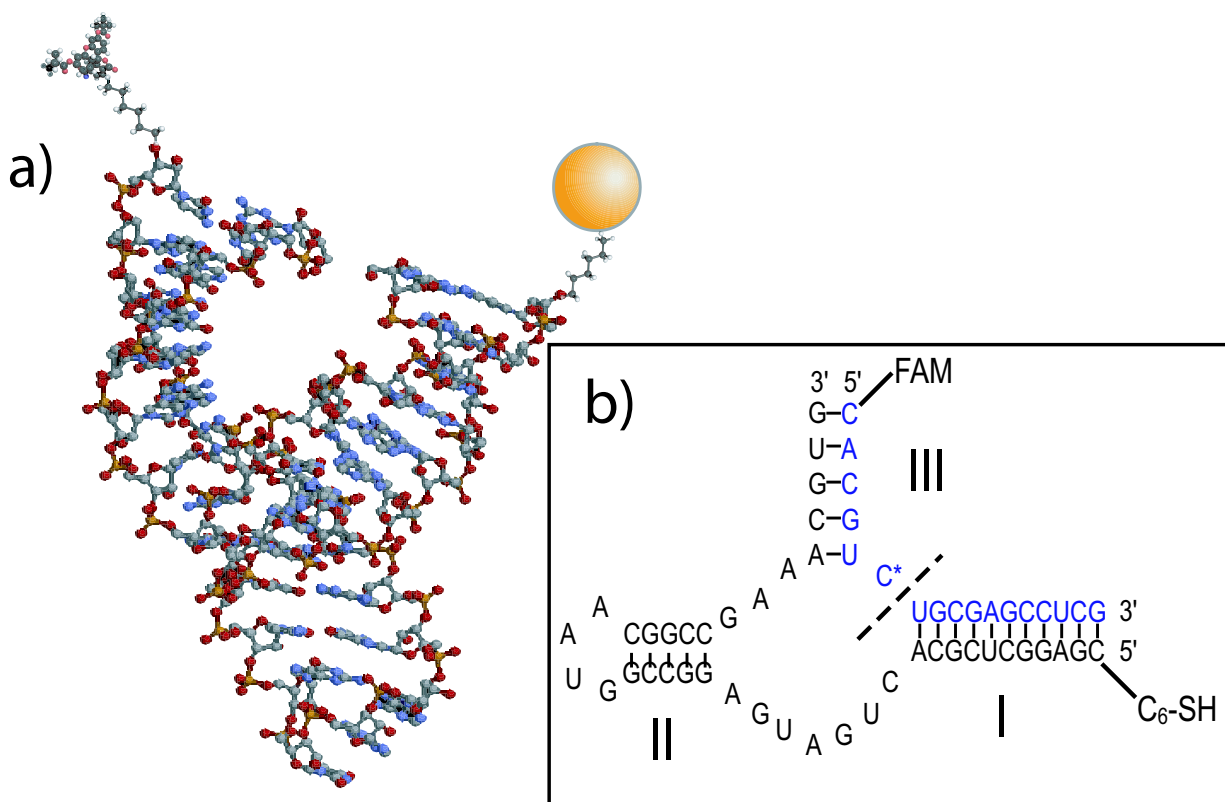


Figure 5.1: a) 3-dimensional scheme of a hammerhead complex containing fluorophore and gold nanoparticle. b) Secondary structure of the I/III hammerhead design used in these studies which employs a fluorescein modifier on the substrate strand and a free thiol on the ribozyme strand. The thiol is used to bind to a 1.4nm gold nanoparticle. Cleavage of the substrate occurs at the “scissile” bond (dashed line). Upon cleavage, the portion of substrate with fluorescein reporter is released outside the quenching radius of the nanoparticle.

Techniques such as stop-reaction polyacrylamide gel electrophoresis (PAGE), analysis of low-pH, rapid freezing single crystal data on the ribozyme,(85; 86) and a variety of insightful FRET experiments(87; 88; 89) have contributed to the current understanding of RNA structural changes associated with catalysis. NSET may be well-suited for application to hammerhead kinetics and conformational studies, particularly because the ribozyme is well studied, can be synthetically manipulated, and demonstrates dynamic distance changes on the 6-11 nm scale.

The purpose of this study is to demonstrate the validity of NSET molecular beacon techniques for analysis of kinetics and conformational changes induced by bimolecular interactions on a synthetic 40-bp hammerhead ribozyme. The ribozyme strand is modified at the 5' end with a thiol functionality for binding to a 1.4 nm Au nanoparticle and its complementary substrate is modified at its 5' end with fluorescein (FAM) as the donor fluorophore. Comparison with results obtained via traditional electrophoresis experiments illustrate the greater precision and ease of the optical methods. The first steps in developing an NSET molecular beacon are testing ribozyme viability under the conditions of our system, detecting intermediates by real-time optical analysis, and proving the method sensitive to the measurement of multi-stage ribozymal activity.

5.2 Experimental

5.2.1 Binding of NanoGold and Preparation of the Hammerhead Complex

RNA strands were purchased PAGE-purified, deprotected and desalted from Dharmacon RNA Technologies and used without further processing. Tris(2-carboxyethyl)phosphine hydrochloride (TCEP) was purchased from CalBiochem. Mono-Maleimido NanoGold®(NG) was purchased from NanoProbes and arrives as a 6 nmol sample lyophilized from PBS buffer which yields a sample at pH 6.5 when dissolved in 200 μ L of RNase-free nanopure H₂O. NG is a 1.4 nm gold nanoparticle composed of 55 atoms and has a single monomaleimido functionality for attachment to a single bio-molecule. It was used without further purification. Binding of NG to the free thiol of the ribozyme strand was performed by dissolving 600 pmol ribozyme into 20 μ L RNase free nanopure H₂O (Barnstead Nanopure Diamond UV/UF). To this solution, 20 μ L of 50mM TCEP was added to the ribozyme solution to regenerate free

thiols from possible dithiol formations. After reacting for 30 minutes at room temperature, the ribozyme solution was brought up to 100 μL and purified from TCEP using successive (2X) P6 spin columns (Bio-Rad). The NG was added to the ribozyme by dissolving a single vial (6 nmol) into 100 μL of nanopure H_2O , which was added to the purified ribozyme solution, vortexed, and placed in the refrigerator at 4°C for at least 24h to allow coupling. Longer reaction times did not influence the activity of the system.

5.2.2 PAGE Analysis of NG - Hammerhead Ribozyme

Equimolar amounts of NG-Rib and FAM-bound substrate strand were combined in a micro-centrifuge tube and heated to 95°C for two minutes, allowed to cool to room temperature over ten minutes, and placed on ice for an additional 10 min to allow formation of the NG-hammerhead complex (NG-HHComp). 60 pmol RNA per lane was loaded on a pre-equilibrated non-denaturing 15% polyacrylamide gel (PA gel) at 4°C and electrophoresed (Fig. 5.3. To show NG-HHComp activity, an identical sample of NG-HHComp was reacted for 2 hours 100 mM Mg^{2+} and loaded on the gel. The gel was imaged first using only FAM luminescence, then EtBr stained and imaged again.

5.2.3 Correlated Optical / PAGE Analysis of NG-Rib

NG-Rib and FAM-labeled substrate strand were annealed in the 20 mM PBS 0.1 M NaCl pH 6.5 buffer and the solution was placed into a clean, dry 50 μL cuvette. The cuvette was placed into a Peltier temperature controlled Cary Eclipse Fluorimeter and allowed to equilibrate at 37°C for 10 minutes. To start the reaction 1.2 μL of 5 M MgCl_2 was mixed in, bringing the solution in the cuvette to 20 mM Mg^{2+} . Photoluminescence (PL) was monitored continuously for 250 minutes (kinetics mode, $\lambda_{ex}=480$ nm, $\lambda_{em}=518$ nm, 5 nm slits). Photoluminescence data was baseline-subtracted based on the minimum intensity after Mg^{2+} -addition and then normalized to pre- Mg^{2+} intensity, (taking into account dilution factors) to obtain product fraction information. PAGE data were obtained simultaneously for the same sample in the PL experiment by removing a 7 μL aliquot (70 pmol hammerhead complex) at specific time points. Each aliquot was quenched by rapid mixing with a denaturing loading buffer containing formamide and 10 mM EDTA, followed by heating to 95°C for 2 minutes and

was electrophoresed on a denaturing 15% PA gel. Using the FAM emission only, the gel was imaged, taking care not to saturate CCD pixels of the gel documenter. Line scans of intensity vs pixel position for each gel lane were background corrected, fit to Gaussian line shapes and the integrated intensity was normalized to a control sample of known concentration (70 pmol of substrate strand) run on the same gel.

5.3 Results and Discussion

5.3.1 Formation of the Hammerhead Complex (NG-HHComp).

In using NSET as a molecular beacon, several questions need to be answered: 1) can the ribozyme labeled by gold still fold into the hammerhead complex? 2) Is the substrate-ribozyme complex still bio-active exhibiting native cleavage kinetics? Figure 5.2 shows an ethidium bromide (EtBr) stained denaturing 10% PA gel for a sample of nanogold (NG) coupled to the ribozyme (NG-Rib) imaged under ambient (visible gel) and UV light (fluorescence gel). When bound to the ribozyme the NG-Rib migrates and is observed visually as a tight brown band for the Au and under UV excitation as a luminescent band due to the EtBr intercalated into the ribozyme. Co-migration of both signals confirms NG binding to the ribozyme strand. Figure 5.3a shows a nondenaturing 15% PAGE after EtBr staining comparing NG-HHComp formation to HHComp. Bands of the HHRib and the NG-HHRib migrate at the same rate, shown by comparing lanes 1 and 2. Also, the HHComp and NG-HHComp (Lanes 4 and 5) migrate the same relative to each other. The identical migration rates of the native RNA strands relative to their NG-counterparts suggests that the bound gold nanoparticle has minimal impact on native conformations of both the ribozyme and the hammerhead complex.

Figure 5.3b is a UV scan of the same gel before staining with EtBr so that only the position of the FAM is imaged. The difference in migration between lanes 3 and 4 arises from the FAM-bound substrate forming the signature hammerhead complex, HHComp, and thereby changing its mobility. A remarkable difference in intensity between the hammerhead complex without NG (lane 4) and the complexes with the bound NG (lanes 5 and 6) is apparent, even though the same amount of FAM-substrate was loaded into all three lanes. This observation is consistent with the high quenching efficiency of fluorophores when in the presence of NG. Fluorescence of FAM on the cleaved substrate in lane 6 indicates that

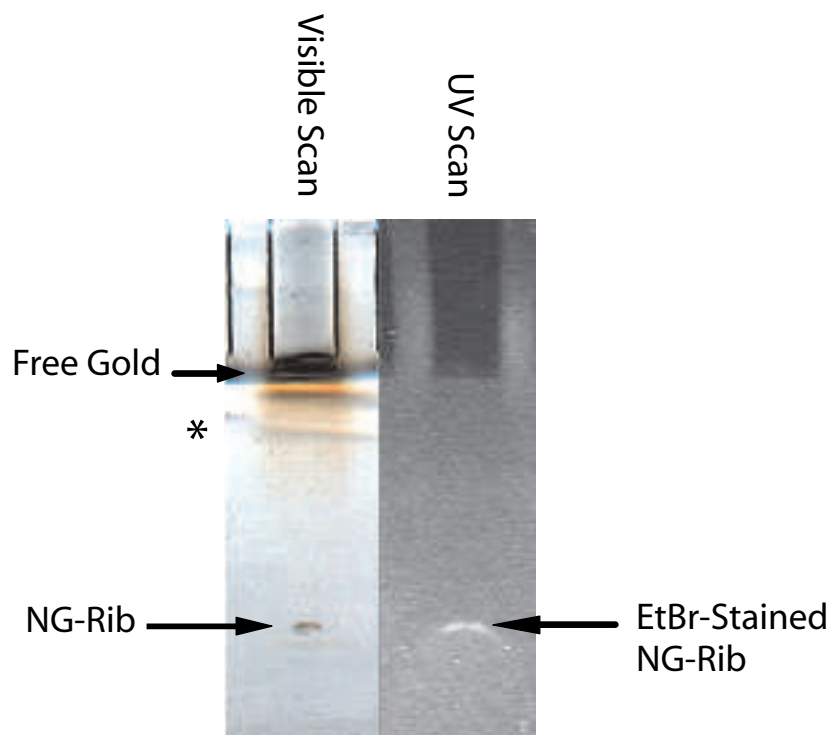


Figure 5.2: Denaturing 10% PA gel of NG-Rib. *Left* shows scanned in image of the gel in which a dark brown band appears near the bottom. *Right* shows the corresponding UV-excitation of EtBr stained gel. Free gold is uncharged and remains at the top of the well. (* Striations just below the well are an artifact of the scanner and are not true bands.)

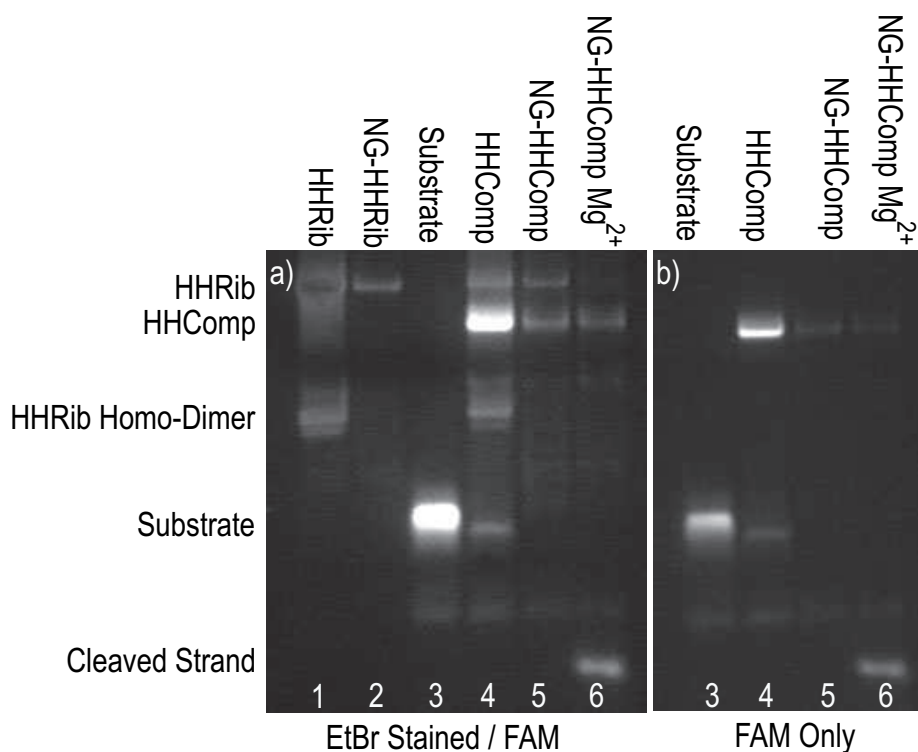


Figure 5.3: a) Ethidium bromide stained nondenaturing PAGE showing different mobilities of (1)HHRib, (2)NG-HHRib, (3)Substrate, (4)HHComp, (5)NG-HHComp, and (6)NG-HHComp reacted with Mg^{2+} . b) Same gel before ethidium bromide staining, demonstrating position of FAM-bound RNA only. Comparison of before and after staining gives evidence of HHRib homo-dimerization to help differentiate from the hammerhead complex, HHComp. All substrate containing lanes have the same amount of FAM-substrate, however it is strongly quenched with the NG-HHComp, (lanes 5,6.) The presence of a high mobility band only in lane 6 in the presence of Mg^{2+} is evidence of NG-HHComp activity.

once the FAM moiety moves outside the quenching radius of the NG, its dipole is no longer damped by the conduction electrons of the NG, which results in an increased fluorescence intensity.

In Fig. 5.3, comparison of the FAM fluorescence image (5.3b) to the EtBr stained image(5.3a) allows differentiation between HHComp and other stable competing structures. The HHRib in lane 1 exhibits a secondary band with higher mobility which we attribute to a stable homo-dimer form of the ribozyme. Based upon calculations using mFold, there are 1-2 stable homo-dimers possible in the absence of the complementary strand at RT. This band

is not observed in lane 2, NG-HHRib, consistent with formation of the lower energy complex.

5.3.2 NSET-based Structural Characterization

NSET is a technique similar to FRET, in which energy transfer from a donor molecule follows a predictable distance dependence; decrease in donor fluorescence intensity is translated into a measurable distance decrease between donor and acceptor. In NSET methods, by coupling the electronic dipole of the luminescent donor to the collection of electron dipoles on the nanometal surface, the dependence of the vector projection is relaxed, resulting in a $1/R^4$ distance dependence vs $1/R^6$ for FRET.(35) Because the metal conduction band is continuous in energy,(52; 22) NSET is dye non-specific and the acceptor is in resonance with all energies for the visible spectrum. This feature, unique to metal nanoparticles, is valuable when using NSET in molecular beacons; single gold nanoparticle will quench all donors on the bio-moiety within a distance of 20 - 210 Å, allowing multiple interactions to be monitored simultaneously. This technique can be applied to kinetic and structural analysis of a wide range of biological molecules, like the hammerhead ribozyme.

The hammerhead ribozyme substrate complex (NG-HHComp) consists of a conserved core for catalysis activity and three complementary base paired regions (Regions I, II, and III) (see Fig. 5.1). The native ribozyme brings together distant regions of a longer sequence through base-pairing with a substrate strand. The NSET molecular beacon allows the characterization of such conformational changes which occur for hammerhead ribozymes analogous to the well-established FRET based optical method in biophysics. Conformational changes of the hammerhead ribozyme have been measured using traditional FRET optical techniques.(90; 91) We use NSET as a molecular ruler because the intensity of the FAM-substrate strand emission will change in a predictable manner as the substrate interacts with the ribozyme. The magnitude of intensity change translates into the varying separation distance between donor and acceptor on the HHComp.

According to the model of Bassi et al. (90) the hammerhead displays a Mg^{2+} concentration dependent structural folding; at high Mg^{2+} concentrations, regions I and II in the minimal complex come closer together while regions I and III move further apart. The addition of NG-Rib to a solution of substrate should give structural information of the native relaxed state (E·S) of the complex, and upon the addition of Mg^{2+} will report the change

in conformation for the activated E·S* complex. Analyzing conformational changes also requires an understanding of the possible conformers for the synthetic ribozyme in Fig. 5.1 that might exist in the native relaxed state. Although we expect the hammerhead complex to be stable at 37°C, we may anticipate that region III is not completely base-paired at this temperature due to its short 5-bp overlap (calculated $T_m < 10^\circ\text{C}$ based on mFold - does not take into account energy of complex formation which will raise the experimental T_m .) Partial basepairing or competition from local structures for these short synthetic ribozymes may result in an unexpected separation distance between donor and acceptor. This is particularly true for the system designed here with the 5-bp overlap in Region III and the 11-bp overlap in Region I. The measured separation includes a combination of ribozyme length, the C₆-linkers and maleimido-coupling groups of the full NG-HHComp. Differences in intensity will be indicative of conformational changes within the activated E·S species of the synthetic ribozyme.

To analyze the conformational changes in our NG-HHComp via NSET, we measured the full fluorescence spectrum of the substrate strand both before and after annealing the NG-Rib and then in the presence of 20 mM Mg²⁺, (Fig. 5.4). The distance change upon binding of Mg²⁺ is estimated by calculating the difference in quantum efficiency of energy transfer between the FAM moiety and the NG. The efficiency of energy transfer between FAM and NG follows a distance dependence according to:

$$\frac{I}{I_o} = \frac{1}{1 - \left(\frac{R}{R_o}\right)^4} \quad (5.1)$$

where I/I_o is the quenching efficiency, R is the separation distance, and R_o is defined as the distance at which 50% of the total intensity has been quenched (in this case 94.3 Å.) This allows a direct measure of the change in structure by following the change in quantum efficiency of energy transfer following Mg²⁺ binding. Figure 5.4 shows that the integrated intensity has dropped by 39% following the addition and annealing of the NG-Rib to the FAM-substrate strand in solution. The change in intensity is indicative of E·S formation and the initial relaxed E·S conformation. Addition of Mg²⁺ to a final concentration of 20 mM results in a decrease of the integrated intensity by an additional 29%, indicating formation of a compact ribozyme structure. The change in intensity of 68% total quenching relative to free substrate is indicative of the conformation change for the NG-HHComp upon Mg²⁺ binding.

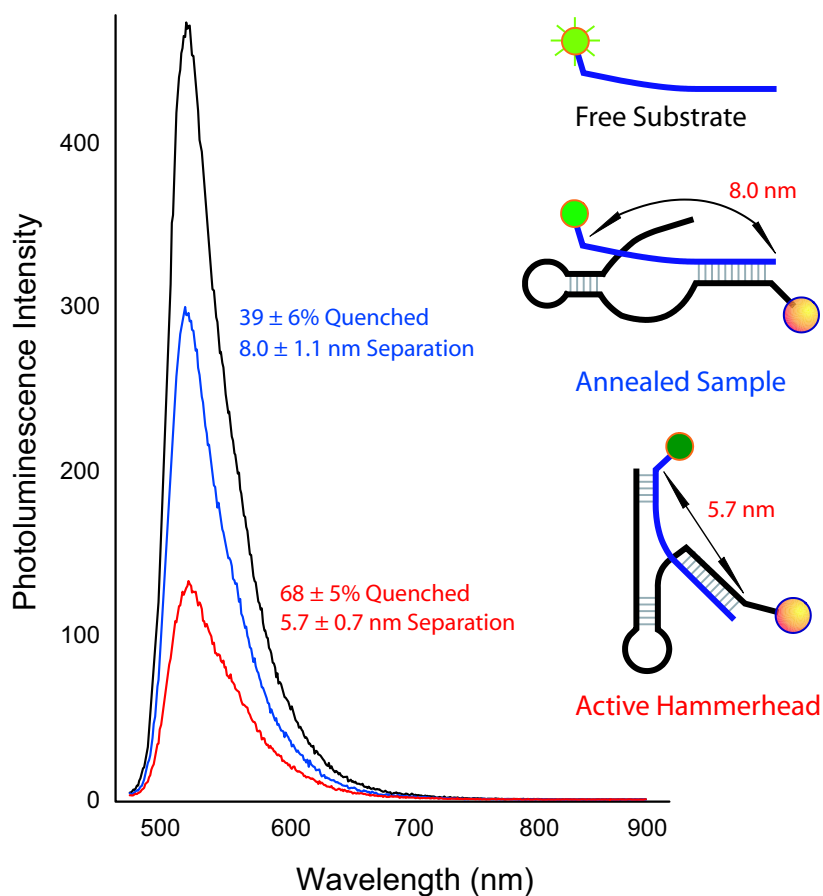


Figure 5.4: Photoluminescence quenching correlated structural changes in the hammerhead ribozyme via NSET. The most intense spectrum shows the intensity of the substrate alone, and then after annealing with NG-ribozyme (blue). Finally, the solution is made to 20 mM Mg^{2+} and PL is measured again, (red.)

Using eqn. 5.1 to calculate the separation distance, R , and correcting for the C_6 -linker length, we estimate separation distances between the 5' ends of regions I and III of 8.0 ± 1.1 nm and 5.7 ± 0.7 nm for the relaxed and activated hammerhead complexes, respectively. In the relaxed E·S conformation, the measured distance of 8.0 nm between the FAM and NG reflects a structure that is unzipped, and not fully annealed in region III. This is reasonable for the short arm of region III, which will have a low T_m . In the activated state following Mg^{2+} addition, the structure adopts a compacted form with a separation distance of 5.7 nm suggesting that region III must be stabilized due to restricted degrees of freedom when the ribozyme complex adopts the correct geometry for catalysis. The ribozyme conformation of 5.7 nm is similar to previously reported values of 6.3 nm based upon FRET for the folded state, (E·S*) of a comparable ribozyme.⁽⁹⁰⁾ Variations in the measured distance between that reported here and in the literature are explained by the differences in sequence and lengths of regions I and III, and the cone angles swept out by the C_6 -linkers.

5.3.3 Optical Tracking of Ribozyme Cleavage

To verify that changes in PL are directly correlated to ribozyme kinetics, a cleavage reaction was performed in the fluorimeter simultaneous with aliquot removal for PA gel. After establishing the relationship of PL to kinetics, we then optically measure different kinetic rates in the next section for a more thorough analysis of our hammerhead ribozyme.

Region I has a calculated T_m value of 53°C, while Region III was designed to have a $T_m < 10^\circ\text{C}$. This design facilitates melting of the FAM-containing product following substrate cleavage and diffusion outside the quenching radius of the gold nanoparticle. Although it has been shown for a natural hammerhead ribozyme that NaCl concentrations $\gtrsim 500$ mM enhance folding into an active state via loop-loop interactions,⁽⁹²⁾ the experiments on this minimal complex were all performed at 100 mM NaCl where, in the absence of auxiliary loops, the concentration is assumed not to affect the results. Figure 5.5 illustrates the substrate - ribozyme strand interaction. By following the intensity of the FAM fluorescence in time, the formation of the substrate-ribozyme complex, the folding in the presence of Mg^{2+} , and the cleavage at the scissile bond (C^*) were followed optically.

After Mg^{2+} addition, we observed a gradual increase in the fluorescence of FAM which correlates directly to the kinetics of the cleavage reaction. The kinetics of hammerhead

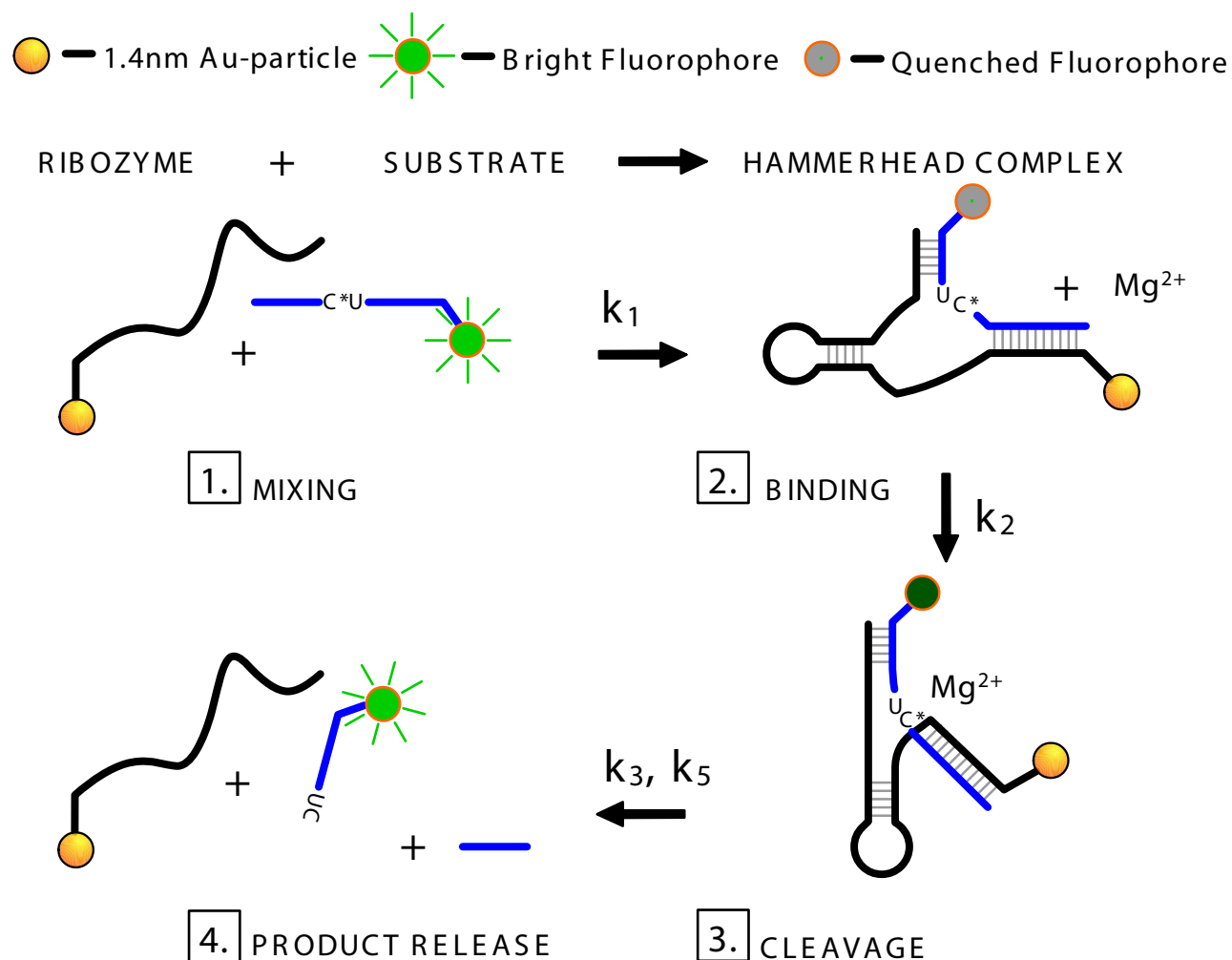


Figure 5.5: Scheme of hammerhead cleavage. The ribozyme binds to substrate strand (1) to form the “hammerhead complex” (2) which, in the presence of Mg^{2+} will cleave the substrate at the scissile bond (3) (dashed line.) The products are released as two separate strands (4) and the ribozyme is regenerated.

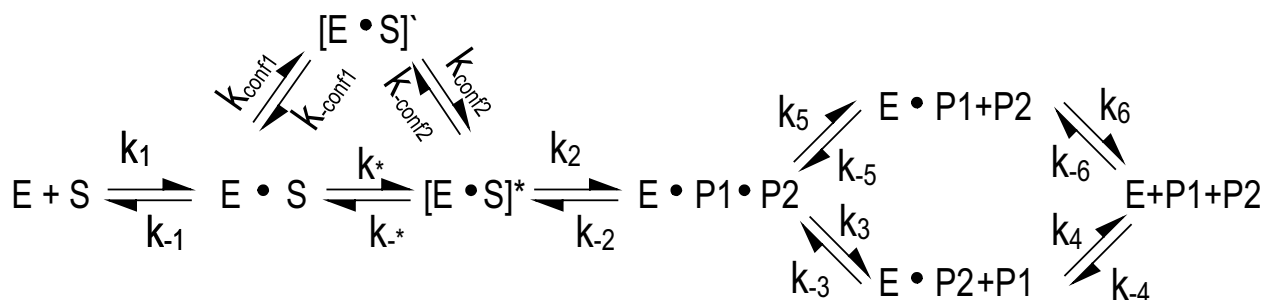


Figure 5.6: Suggested reaction pathway for the hammerhead ribozyme. E is ribozyme, S is substrate, P1 and P2 are the 5' and 3' products, respectively. k_* and k_{-*} represent the forward and backward rates for interconversion with an activated state $[E \cdot S]^*$ which in turn yields products during the cleavage reaction, k_2 .

cleavage(93; 94) (Fig. 5.6), suggest that the pathway leading to product release requires multiple steps with different kinetic rates for each step along the trajectory. The complexation step for ribozyme (E) - substrate (S) is the first process with rate, k_1 , followed by folding in the presence of Mg^{2+} (k_*) to form the activated complex ($E \cdot S^*$). We note the possibility of inactive complex formation which may interconvert between the $E \cdot S$ and $E \cdot S^*$ states with rates k_{conf1} and k_{conf2} . The existence of an inactive state would influence the rate of cleavage by providing a separate pathway that must convert back to an active state before a reaction may occur. From the activated complex $E \cdot S^*$, the slow step of product formation is k_2 and dominates the observed kinetics if k_5 and $k_3 \gg k_2$. This can be achieved by carrying out the reaction at elevated temperature, (37°C). The optimal pH for rapid ribozyme cleavage is pH 7.5. However, in order to allow significantly better time-resolved PAGE kinetics, reactions were performed at pH 6.5 where literature shows that the rate of cleavage is commonly on the order of 10^{-2} min^{-1} .(94; 95; 96)

The kinetics for substrate cleavage (k_2) generated from the NSET molecular beacon and PAGE on a pre-annealed 1:1 ratio of ribozyme to substrate are analyzed in Fig. 5.7. Figure 5.7a shows a fluorescent denaturing PAGE image of FAM under UV-excitation. The upper band is the intact substrate strand and the lower band is the cleaved portion with attached FAM. In Fig. 5.7b, the kinetic traces derived from the PAGE data and the continuously monitored photoluminescence for the FAM at 518 nm are plotted versus time. Fig. 5.7b

shows that upon rapid mixing of Mg^{2+} to the NG-HHComp, the intensity of the FAM decreases immediately as the complex folds to bring the FAM into closer proximity of the NG. After 1-2 min. the intensity of the FAM photoluminescence begins to increase as the cleavage reaction progresses, approaching a maximum value near $t = 250$ min. The kinetics traces for both PAGE and PL results can be fit to a first order reaction rate of the form:

$$F(t) = F_o + F_{\infty}(1 - e^{-kt}) \quad (5.2)$$

In this equation the fraction of product as a function of time, t , is equal to the initial fraction present, F_o , plus an exponential term including the rate of reaction, k , weighted by the fraction of product formed at time infinity, F_{∞} . The intensity data for each kinetic trace were normalized to a sample of the NG-HHComp in the absence of Mg^{2+} ($t < 0$), and the value of F_o is assumed to be zero at $t = 0$ (time of Mg^{2+} addition), which allows the background intensity of the photoluminescence trace to be subtracted. This assumption can be confirmed by PAGE where no product is observed before the addition of Mg^{2+} . At $t = 250$ minutes, the reaction had gone sufficiently to completion for good kinetics fitting using both methods.

A fit of the kinetic traces in Fig. 5.7b yields the rate of cleavage, $k_2 = 0.014 \pm 0.001 \text{ min}^{-1}$ for PAGE and $0.013 \pm 0.001 \text{ min}^{-1}$ for PL. The strong agreement on observed rates verifies for the two techniques that the changes in photoluminescence intensity are directly related to ribozyme kinetics.

A slight difference of 6% total product fraction, F_{∞} , was observed between the two methods. Because the fluorimeter measures the control photoluminescence (intensity at 518 nm before addition of Mg^{2+}) as well as changes in intensity under identical conditions throughout the course of the experiment, the PL measurement is likely to be more accurate regarding the total product fraction. Despite the small difference in F_{∞} , the kinetics are identical.

5.3.4 Ribozyme-Substrate Binding and Cleavage: E·S Stability

The initial complexation step (k_1 in Fig. 5.6), which represents annealing of the substrate strand to ribozyme, was extracted from NSET analysis. Because the hammerhead complex was designed for high T_m in the complexed state, it is expected that the hammerhead

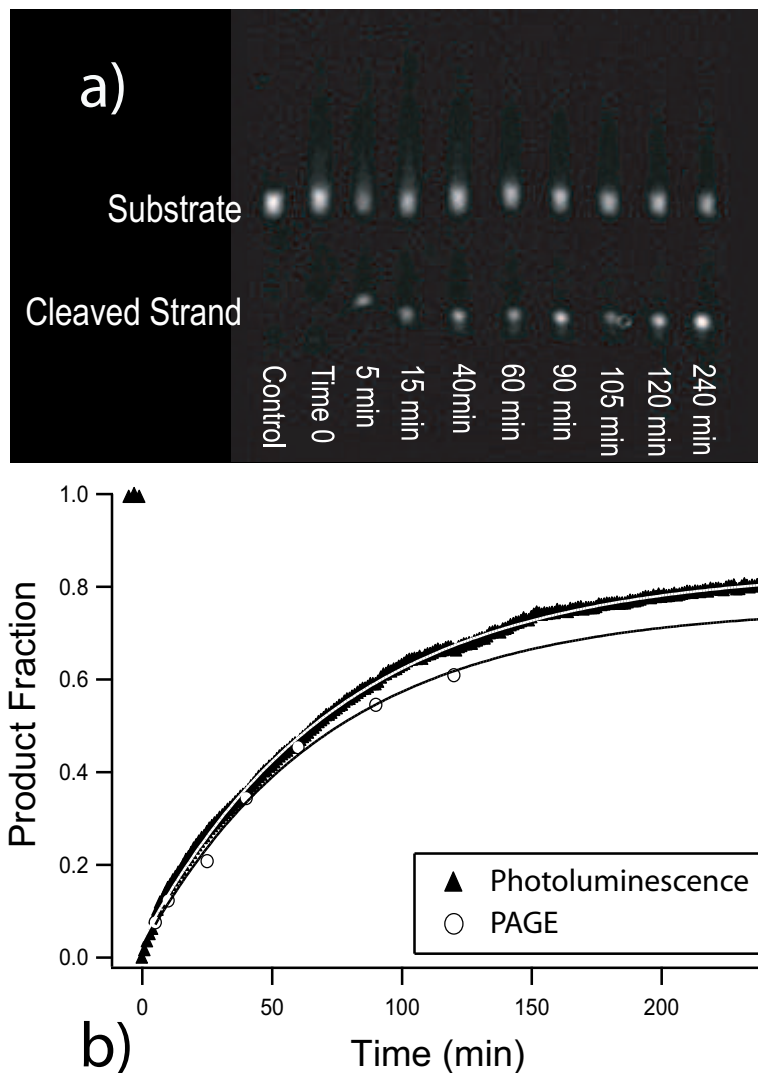


Figure 5.7: a) Denaturing PAGE of ribozyme kinetics. Each lane represents an aliquot removed from reaction at a specific time. b) Photoluminescence intensity of FAM monitored at 518 nm. The initial intensity of FAM fluorescence decreases sharply upon addition of Mg^{2+} as the hammerhead folds into a tighter structure prior to substrate cleavage.

complex remains annealed after formation, i.e. the dissociation rate k_{-1} is much slower than the binding rate k_1 .⁽⁹³⁾ However, the rate of substrate binding can be a difficult kinetic parameter to measure because it is a rapid event, often taking place within seconds, thus necessitating an expeditious method of analysis. By measuring the binding rate at several different ribozyme - substrate concentrations, it is possible to extract the binding rate constant (k_{c1}) and the rate of dissociation (k_{-1}). Three different reactions were performed on the NG-HHComp at ratios of ribozyme:substrate 1:1, 3:1, and 10:1. The substrate strand concentration was held constant at 2×10^{-7} M and both ribozyme and substrate were 20 mM Mg^{2+} before combining the two solutions. The presence of Mg^{2+} did not appear to influence the rate of binding. Figure 5.8 shows the photoluminescence data for the substrate in buffer from the time of ribozyme addition $t=0$, to the point of minimal intensity for 3 different ratios. Because this experiment is being performed at low pH, it has the additional advantage that cleavage, and therefore brightening, does not occur fast enough to influence the decay kinetics of substrate binding. The binding of ribozyme to substrate is first order, as shown by the linear decay in Fig. 5.8 when plotting the log of intensity vs time (the asymptotic drop in intensity due to mixing in a quencher has been omitted). For this reason, each of the decays in Fig. 5.8 have been fit to an equation of the form:

$$Sub_{free}(t) = Sub_{free}^0 e^{-k_1 t} \quad (5.3)$$

Equation 5.3 allows the forward rate of binding substrate, Sub_{free} , to ribozyme, (k_1 , min^{-1}) to be calculated. The concentration independent binding rate constant, (k_{c1} , $\text{M}^{-1} \text{min}^{-1}$) may be calculated by plotting the rate of binding, k_1 , vs ribozyme concentration. The slope of the resulting line, (inset of Fig. 5.8), is the binding rate constant and the y-intercept is the dissociation rate of the ribozyme, k_{-1} . The slope, $14.9 \pm 1.5 \mu\text{M}^{-1}, \text{min}^{-1}$ is of the expected order of magnitude⁽⁹³⁾ and the y-intercept ~ 0 suggests that the dissociation rate is negligible for this hammerhead complex. Fig. 5.9 shows the cleavage traces based upon PL for the same three different E:S ratios. The rate is shown to increase with increasing ribozyme concentration, yet demonstrates intriguing kinetics because the two lowest ratios, 1:1 and 3:1, show similar cleavage rates to the pre-annealed sample in Fig. 5.7 whereas the high ratio, 10:1, exhibits much faster biphasic kinetics.

The kinetics may be understood by treating our hammerhead complex as a regime 2 ribozyme, according to the nomenclature suggested by Stage-Zimmerman *et al.*⁽⁹³⁾ Regime

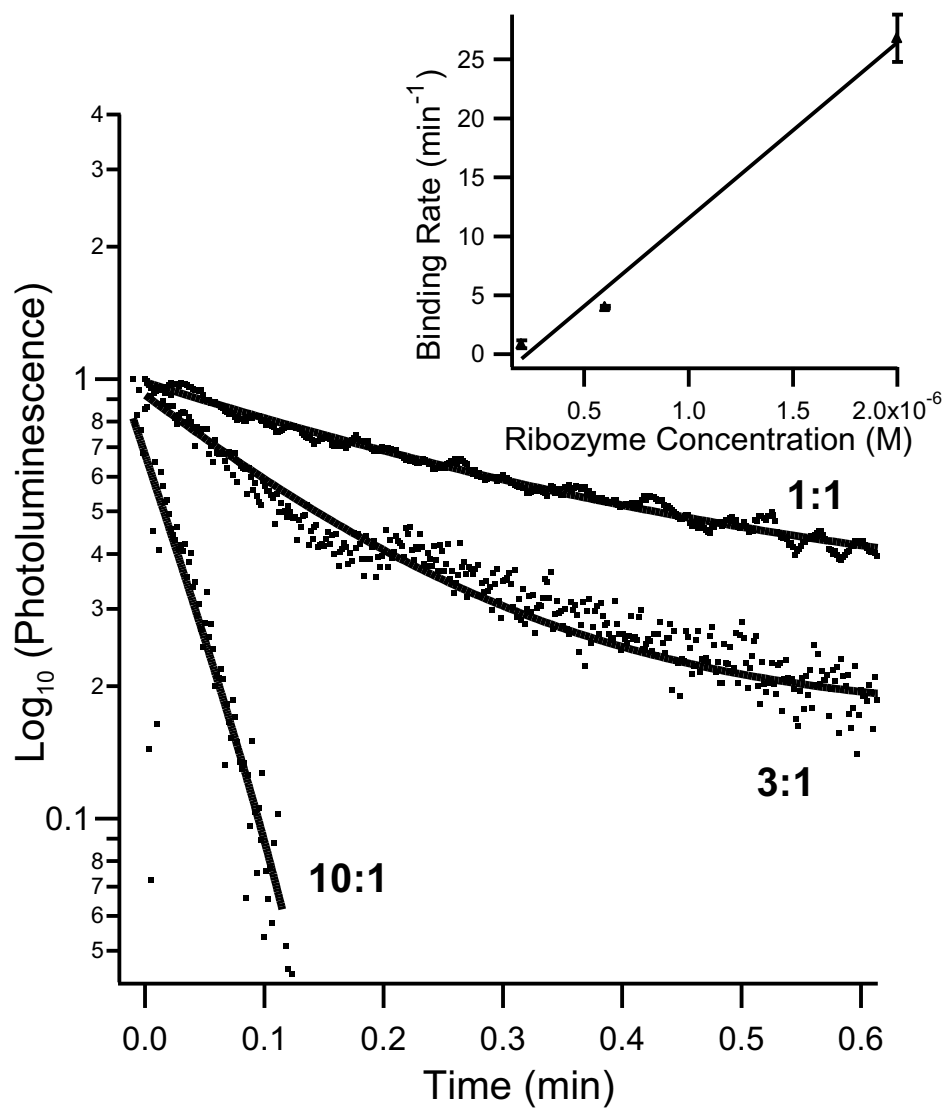


Figure 5.8: Hammerhead complex formation studies via NSET. The substrate strand at constant concentration was given different stoichiometric ratios of NG-ribozyme while monitoring fluorescence. Early time kinetics show that different ratios of ribozyme to substrate (E:S) affects the rate of substrate binding. The inset shows a plot of binding rate vs. ribozyme concentration, the slope of which yields the binding rate constant, k_{c1} , for our complex at 37°C.

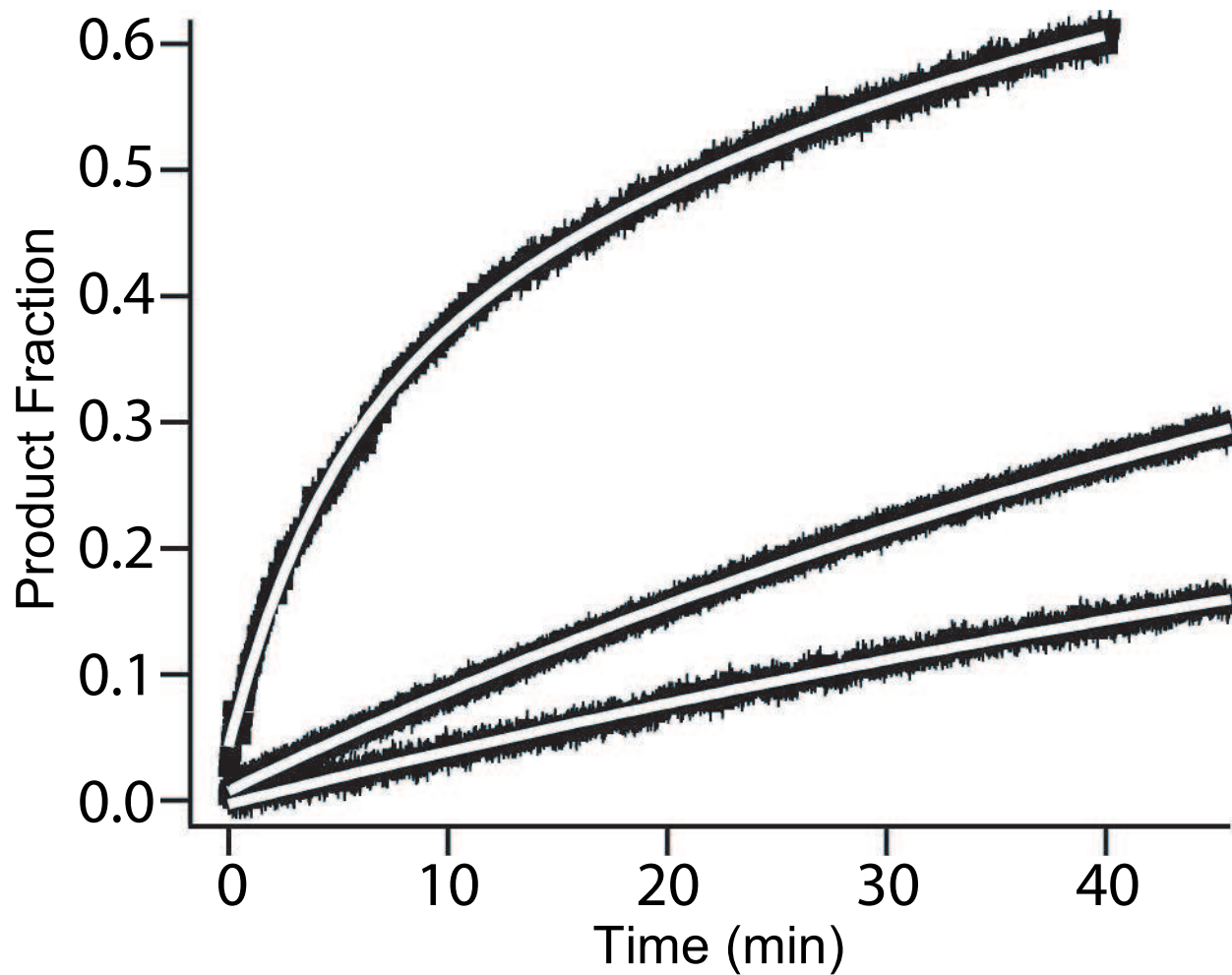


Figure 5.9: The resulting cleavage traces based upon emission from the 5' substrate bound fluorescein dye as a function of ribozyme-Au concentration. The ratio of ribozyme to substrate, (E:S), was varied from 1:1, 3:1, and 10:1. *Inset* shows the cleavage rate, k_2 as a function of ribozyme concentration at 37°C and pH 6.5.

2 kinetics exhibit the relationship: $k_{-1} \ll k_2$, meaning that all substrate binding goes forward to form product because the rate of dissociation is negligible. However, as NSET structural characterization has shown, region III of the complex is not entirely stable at 37°C, giving the hammerhead regime 1 characteristics in which k_{-1} may govern ribozyme activity by controlling K_d .

The conclusion is that the hammerhead studied here is likely to fall between regimes 1 and 2, thereby suggesting the probable formation of an inactive complex $E \cdot S'$ off the kinetic pathway. Slow interconversion from such a structure may manifest biphasic kinetics if $k_{conf1,2} \sim k_2$. The rate of reaction for a regime 2 hammerhead is controlled by the fraction of $E \cdot S$ complexes present in solution, which is a function of both the binding rate and annealing conditions. At the 10:1 ribozyme:substrate ratio (Fig. 5.9), the reaction is strongly biphasic, which is commonly explained by the existence of inactive conformations along the kinetic pathway. To test the possibility of inactive state formation, time-resolved nondenaturing PAGE was performed on the hammerhead complex.

Nondenaturing PAGE is sensitive to the different conformations of nucleotides, which means that a folded vs. an unfolded structure may be discriminated from each other. Figure 5.10a gives an example of a nondenaturing PAGE hammerhead reaction where time-resolved aliquots were electrophoresed on a continuously running PA gel. Because the gel is running continuously and aliquots are added at different times, there is necessarily a curvature to the gel at later time points. The bands imaged in this gel use only FAM fluorescence as a marker. Three different bands are seen for each aliquot, none of which align with free substrate strand, which suggests the existence of three distinct conformations. The cleaved strand with the highest mobility migrates the furthest, while determination of the upper two bands arises from line scan analysis. Figure 5.10b shows the comparative results after integrating each band. Total intensity for each lane was normalized to 1 and the fraction of intensity under each band is plotted vs time. The kinetics displayed in 5.10b demonstrate classic steady-state conditions where the rates $k_1 \approx k_{conf1,2} \approx k_2$. Under these conditions, the concentration of an intermediate state is formed rapidly and maintains its concentration for the duration of the experiment or until the concentration of starting material, ($[E \cdot S]$) is depleted. A typical reaction diagram is displayed in Fig. 5.10b.

A structure such as this may be intriguing for further kinetic characterization because it contains a known inactive state which may be controlled through sequence engineering or

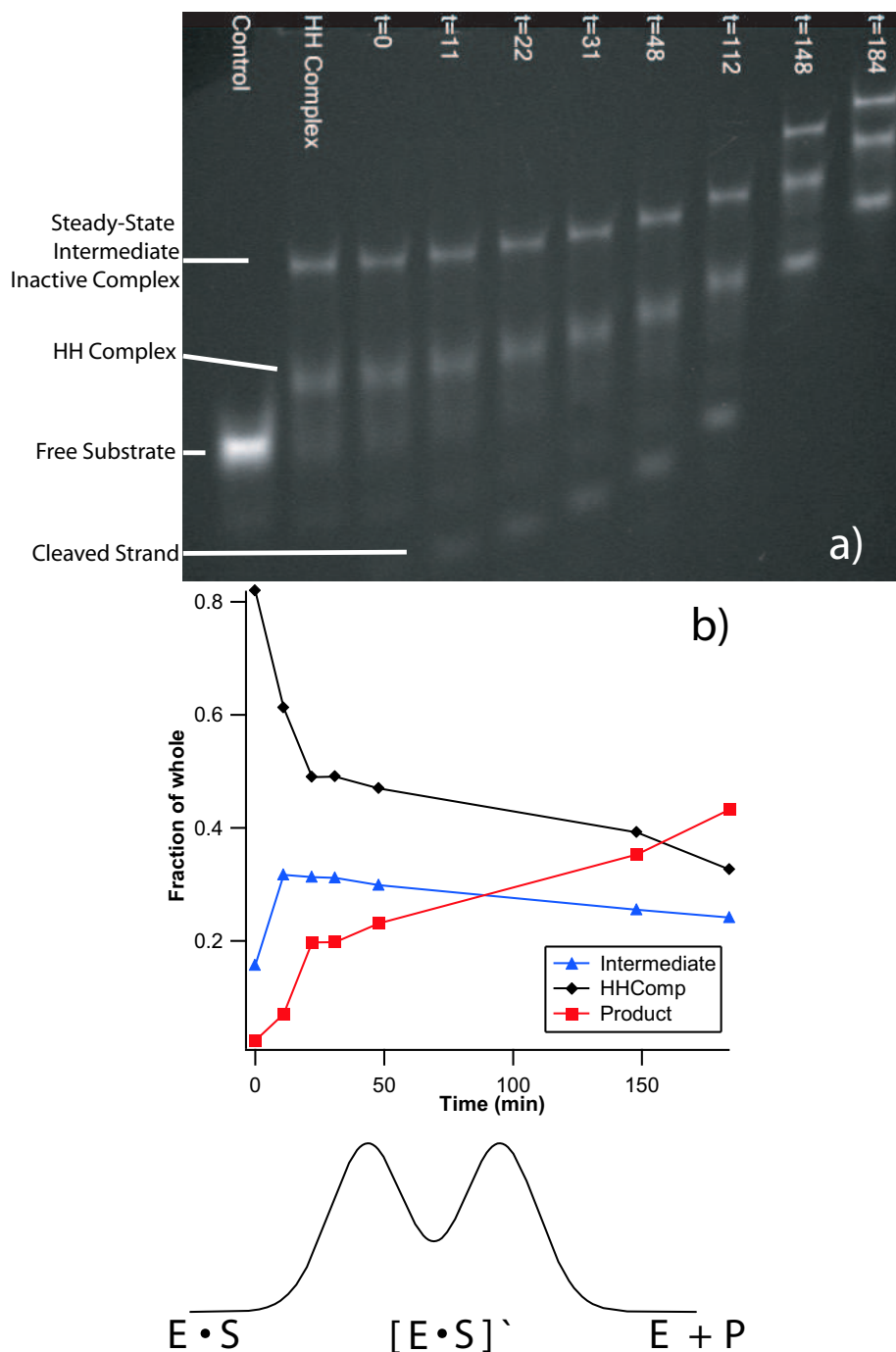


Figure 5.10: a) Nondenaturing 15% PA gel of a hammerhead reaction. The samples are all loaded immediately upon extraction from solution on a continuously running gel. The top band is the steady-state inactive complex, the middle band is the tighter active complex, and the bottom band is the cleaved substrate strand. b) Relative integrated intensity of each band vs. time. A steady-state intermediate (inactive complex) $[E \cdot S]'$ is formed which transitions into an active state to form products.

Table 5.1: Binding and cleavage rate constants of the all RNA hammerhead ribozyme as measured here by NSET optical analysis. The substrate was held at constant $2 \times 10^{-7} \text{M}$ in all assays. The 10:1 ratio was fit to a bi-exponential rise and the fast, k_2^1 and slow, k_2^2 cleavage rates are reported.

Ribozyme	Binding Rate	Cleavage Rate
Concentration (M)	$k_1, (\text{min}^{-1})$	$k_2, (\text{min}^{-1})$
2.0×10^{-7}	0.855 ± 0.02	0.010 ± 0.0020
6.0×10^{-7}	4.00 ± 0.12	0.013 ± 0.001
2.0×10^{-6}	26.8 ± 2.01	$k_2^1 = 0.23 \pm 0.02$
		$k_2^2 = 0.03 \pm 0.01$

temperature controlled experiments.

Table 5.1 lists the calculated cleavage and binding rates (k_1 and k_2) and the binding rate constant (k_{cl}) observed in the NG-HHComp system. We measure a binding rate constant for our hammerhead complex to be $k_{cl} = 14.9 \pm 1.5 \mu\text{M}^{-1} \text{min}^{-1}$, which is in very good agreement with the binding rate constants reported for different hammerhead ribozymes measured by radioactively-labeled pulse-chase experiments which are on the order of $2.5 \mu\text{M}^{-1} \text{min}^{-1}$ to $84 \mu\text{M}^{-1} \text{min}^{-1}$.(97) These results are the first reported binding rate measurements on hammerhead ribozyme kinetics measured using optical nanoprobe methodologies.

5.4 Conclusions

A new molecular beacon style optical method based on NSET has been applied to the measurement of hammerhead ribozyme kinetics and analysis of the Mg^{2+} induced conformational changes. The HHComp exhibits incomplete base-pairing for region III in the complexed state, giving a calculated distance between 5' ends of 8.0 ± 1.1 nm which folds up to 5.7 ± 0.7 nm in the presence of Mg^{2+} . We have been able to establish that the NG-HHComp is active and yields kinetics information consistent with earlier studies on similar ribozyme complexes. The results demonstrate that binding a small gold nanoparticle (NG) to the 5' end of a strand of RNA, the RNA has neither lost the ability to bind to its complement and form a hammerhead ribozyme complex nor the ability to perform catalysis. The maintenance of catalytic activity in the presence of NG is a critical demonstration if NSET-based molecular beacons or molecular rulers are to be utilized in biophysical studies. As PAGE results demonstrated, the use of NSET as an optical method is valid for the real-time monitoring of ribozyme kinetics with the added ease of ability to measure other rates along the ribozyme-substrate interaction, such as binding kinetics.

NSET has shown to be advantageous to the measurement of very fast processes which are otherwise difficult to observe. The rate constant of binding for our hammerhead ribozyme was measured to be $k_{cl} = 14.9 \pm 1.5 \mu\text{M}^{-1} \text{ min}^{-1}$ in pH 6.5 buffer and at 37°C, which is similar to reports in literature under these pH conditions. Structural characterization suggesting incomplete base-pairing in region III elucidates the observed kinetics by suggesting the existence of known inactive complex.

CHAPTER 6

DUAL DYE HAMMERHEAD NSET TRIANGULATION

6.1 Introduction

Förster resonance energy transfer (FRET) - based optical rulers as used in biology have become a standard tool for many biochemists and structural biologists in the determination of bio-molecular processes such as protein structural changes(98; 99) protein-protein or protein-RNA interactions(100; 101) to name a few examples. Although FRET is a wonderful tool and is capable of reporting separation distances up to 10 nm from a donor to an acceptor (D-A) molecule, it has certain weaknesses: 1) Coupling of two point dipoles leads to a $1/R^6$ distance dependence and therefore very short measurable distances, 2) FRET dye-pairs must overlap in energy (photoluminescence energy from the donor and absorption energy of the acceptor), and 3) are usually spectrally difficult to separate the photoluminescence arising from the donor and from the acceptor. While theoretically the efficiency of FRET can be improved by orienting D-A dipoles in space,(102) a more universal adjustment must be implemented if fluorophores are to truly triumph over the FRET barrier of modern optical rulers.

Nanomaterials are changing the way many scientists currently approach problems in science, and the FRET barrier too may have fallen to their steady approach. We have shown that small gold nanoparticles are very efficient quenchers of nearby excited state fluorophores via through-space interactions with the high density of metallic conduction electrons.(42; 103; 104) This is readily understood in terms of earlier theoretical work,(29; 48; 35) where a $1/R^4$ D-A distance dependence occurs geometrically from the relaxation of the dipole projection as the nanoparticle better approximates a surface than a point dipole. Furthermore, conduction band electron behavior of the metal extends energetically across the

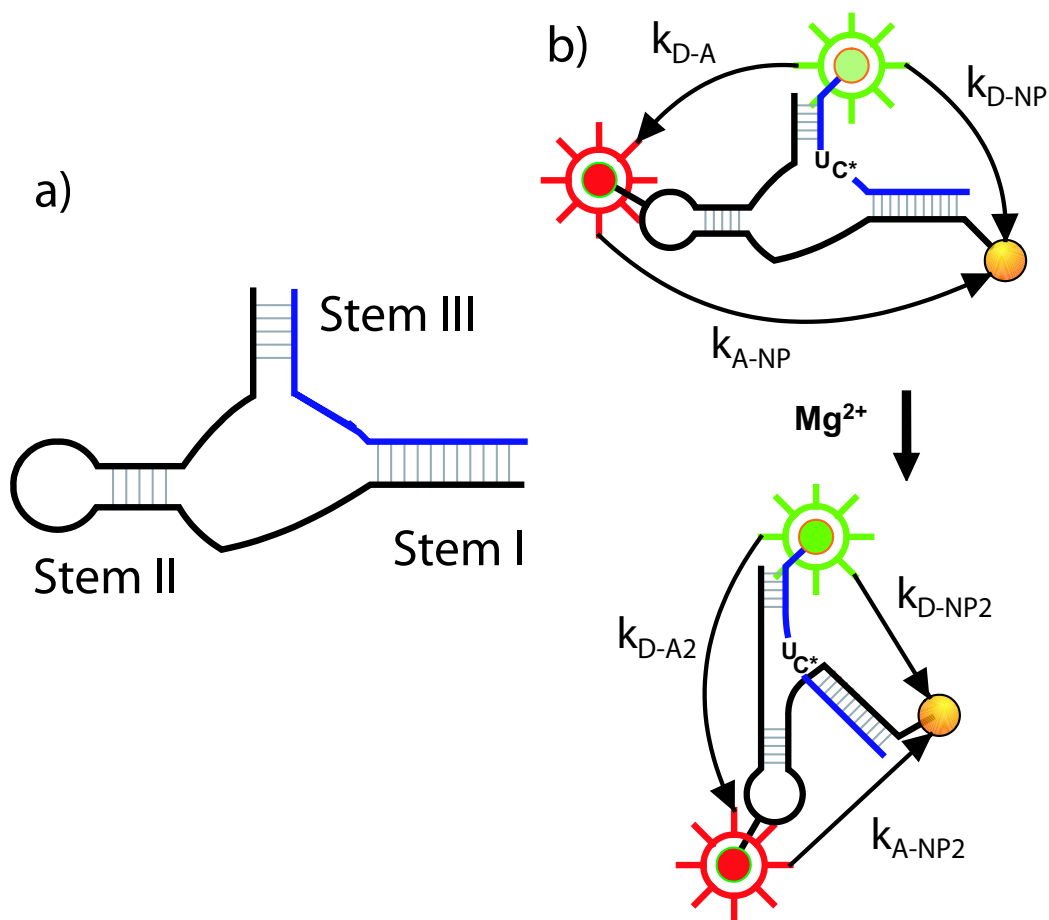


Figure 6.1: A) Generalized hammerhead primary structure resembling an upside-down hammer. In this structure, the hammerhead complex is formed via base-pairing of a substrate strand to stems I and III. b) Scheme of multiple dye quenching to a single 1.5 nm gold NP bound to Stem I of a hammerhead ribozyme. The Cy3 and Alexa Fluor 647 dyes are a FRET pair, yielding distance information between them, while both are being simultaneously quenched by the metal NP. Lifetimes allow the measurement of energy transfer rates between D-A (k_{D-A}), between donor - NP (k_{D-NP}), and between the acceptor - NP (k_{A-NP}). Also, the addition of Mg^{2+} induces a conformational change which should change the rates of energy transfer between all emitters and acceptors.

visible spectrum which allows the metal nanoparticle to damp the excited state oscillations of a nearby dipole with essentially no resonance condition.⁽⁴⁸⁾ The ramifications of these properties when using a metal instead of a point dipole as the energy acceptor are that we have now overcome to a large degree the disadvantages of FRET; the measurable distance is extended, there is no overlap integral to calculate, and a gold nanoparticle does not fluoresce so that spectrally no separation is necessary between D-A emission.

We use this advantage of nanometal surface energy transfer (NSET) as a tool to characterize the distances and conformational changes associated with the three arms of a I-III hammerhead ribozyme. Figure 6.1 shows how, by using two organic dyes in conjunction with a 1.5 nm diameter gold nanoparticle appended to separate arms of a hammerhead ribozyme we may triangulate distances between the ends of separate base-paired helices. In this scheme, the Cy3 dye on stem I will transfer energy using a FRET mechanism to the AF647 dye appended to stem II. In an NSET mechanism, however, Cy3 will donate energy into the NP on stem I if present. Utilizing these two different energy transfer pathways, we measure separation distances between stems II and III and also between stems I and III. The ability to gauge separation distance between stems I and II comes about by measuring the energy transfer from the AF647 dye to the NP in an NSET event. Therefore, by appending probes to each stem of a hammerhead ribozyme, we take advantage of multiple dye-quenching processes, yielding three-dimensional information about the native structure and the Mg^{2+} -induced conformational changes. For the correct controls, the ribozyme strand was separated synthetically into three categories: Type I ribozyme contains only the gold NP (NP-Rib), Type II ribozyme contains only the Alexa Fluor 647 dye (AF647-Rib), and Type III ribozyme contains both the gold NP and the Alexa Fluor 647 dye (NP-Rib-AF647).

6.2 Experimental

Nanoparticle Synthesis: Gold nanoparticles (NP's) were synthesized as described by literature techniques,⁽⁴⁶⁾ using the rapid reduction of hydrogen tetrachloroaurate ($AuCl_4 \cdot 3 H_2O$) in the presence of tetraoctylammonium bromide by sodium borohydride in an argon-sparged water/toluene mixture. TEM measurements displayed particles with an average diameter of 1.5 ± 0.5 nm. The particles were washed thoroughly with a variety of solvents including hexanes, sodium nitrite solution, and MeOH- H_2O . Ligand exchange was

accomplished using ~ 400 mg Bis(p-sulfonatophenyl)phenylphosphine dihydrate (SPP) in 30 mL nanopure H₂O to 32 mg purified nanocrystal in 32 mL methylene chloride. The two phases were stirred overnight resulting in extraction of the organically-soluble NP to the aqueous phase through ligand exchange. Aqueous NP was lyophilized into small aliquots of ~ 2 nmol/vial and stored at 4° C.

Binding of gold NP's and Preparation of the Hammerhead Complex. RNA strands were purchased HPLC-purified, deprotected and desalted from Integrated DNA Technologies and used without further processing. Two strands were purchased, a substrate strand with appended Cy3 dye (Cy3-Sub), and a ribozyme strand (Rib). The ribozyme strand contained two base modifications: a 5' dithiol for NP coupling, and an internal dT-C₆-amine for succinimidyl ester dye coupling.¹

Type I Ribozyme preparation: Binding of NP to the free thiol of the ribozyme strand was performed by dissolving 1 nmol ribozyme into 20 μ L RNase free nanopure H₂O (Barnstead Nanopure Diamond UV/UF). To this solution, 20 μ L of 50 mM dithiothreitol (DTT) was added to the ribozyme solution to regenerate free thiols from possible dithiol formations. After reacting for 30 minutes at room temperature, the ribozyme solution was brought up to 100 μ L and purified from DTT by desalting through a NAP-5 column, collecting the first 750 μ L containing $\sim 90\%$ of the ribozyme with free thiol. This solution was immediately added to a vial containing ~ 6 nmols dry, purified 1.5 nm NP's. The solution was vortexed and placed in the refrigerator at 4°C for at least 24 hours to allow coupling. Longer reaction times did not influence the activity of the system. The NP-ribozyme (NPRib) was then purified by 3X successive ethanol (EtOH) precipitations. The unbound NP does not precipitate with increased salt and ethanol conditions, and so the formation of a dark brown pellet is proof of successful NP conjugation with the ribozyme.

Type II Ribozyme preparation: Alexa Fluor 647 (AF647) amine reactive dye was purchased from Molecular Probes as a labelling kit (PN: A-20196). The dye was reacted with the free amine of the ribozyme strand by following Molecular Probes' protocol provided

¹Ribozyme: 5' - HS-C₆-AGU GAC UGA UGA GGC CGT_{C₆Amine} AAG GCC GAA ACU UCA - 3'
 Substrate: 5' - Cy3-UGA AGU CUC ACU - 3'

in the kit and allowed to react in the dark at room temperature overnight. Purification of the ribozyme from the free dye was accomplished by performing successive (3X) EtOH precipitations, followed by desalting through a NAP-5 column, followed by successive (2X) EtOH precipitations again. The absorption of the dye peak (647 nm) relative to absorption at 260 nm was monitored throughout until no change could be observed, at which point it was determined that all free dye had been removed. Absorption calculations helped to determine a coupling efficiency of 67% for this reaction.

Type III Ribozyme preparation: To accomplish the dual conjugation of both NP and dye to the same strand, the NP was conjugated first because DTT has been shown in our laboratory to have a detrimental effect upon dye quantum efficiency. Therefore, NP was bound to ribozyme and purified identically to the procedure described above under “Type I Ribozyme preparation.” Afterward, 2 nmol purified product was obtained and the free amine was conjugated to Alexa Fluor 647 as described in “Type II Ribozyme preparation” and then purified by successive (3X) EtOH precipitations, (2X) NAP-5 columns, and (2X) EtOH precipitations. UV-vis absorption showed >99% coupling of the dye to the ribozyme, where the coupling efficiency may have been increased by the higher ratio of dye-RNA by using only 2 nmols RNA instead of 8 nmols as recommended in the protocol by Molecular Probes.

Lifetime Measurements: The hammerhead complex was formed by annealing 60 pmol ribozyme strand (Type I, II, and III) with 44 pmol Cy3-Sub in a total solution volume of 160 μ L of pH 6.5 20 mM phosphate buffer (280 pM total concentration RNA) at 95° C for 2 minutes, allowed to cool to RT for 5 minutes, and finally placed on ice for 5 minutes. All samples were measured in a quartz cell maintained at 2° C. The combination of low pH buffer and low temperatures keeps the reaction from moving forward efficiently so that a static lifetime may be measured. The Cy3 dye was excited using the pulsed output of a SpectraPhysics NdVO₄ laser (532 nm, 76 MHz, 10 ps) dropped with neutral density to \sim 100 μ W excitation power, used without focusing at the sample. Alexa Fluor 647 dye was excited using the cavity dumped output of a Coherent 720-1 R6G dye laser, (620 nm, 1.9 MHz, 10 ps, 10 μ W focused). Fluorescence was collected right angle and focused into a Chromex 500is 0.5 m monochromator (100 μ m slits, 50 g/mm grating, 0.5 nm resolution) coupled to a

Hamamatsu C5680 Streak Camera operating with a 10 ns time window with 50 ps resolution.

6.3 Results and Discussion

Figure 6.2 compares the appropriate emission spectrum for Cy3 to the absorption spectrum of AF647, where the area bound between the two spectra is the J-overlap integral using the equation:

$$J = \frac{\int_0^\infty I(\nu)\varepsilon(\nu) \cdot \nu^4 d\nu}{\int_0^\infty I(\nu) d\nu} \quad (6.1)$$

Where the integral has been normalized such that the total area under the photoluminescence data curve is equal to one. Using this equation, we calculate a R_0 value equal to 4.5 nm, (details of this calculation may be found in Appendix C).

The energy transfer efficiency from both Cy3 and AF647 can be calculated by treating the problem using NSET theory which yields a value of d_0 according to the expression:

$$d_0 = \left(0.225 \frac{c^3 \Phi_{dye}}{\omega_{dye}^2 \omega_F k_F d^4} \right)^{1/4} \quad (6.2)$$

where d_0 is the analogous NSET value to R_0 in FRET theory. By using the quantum efficiencies of the dyes and the angular frequencies of emission we calculate d_0 values of 6.2 nm for both dyes to the NP.²

The observed luminescence lifetime of a molecule represents the probability for radiative transition to the ground state as opposed to any other non-radiative pathway:

$$1/\tau_{obs} = k_{obs} = k_r + k_{nr} + k_{et} \quad (6.3)$$

where τ_{obs} and k_{obs} are the observed lifetime and the observed luminescence decay for the molecule. The observed rate will be the sum of all rates contributing to de-excitation of the molecule such as the radiative rate (k_r), the non-radiative rate (k_{nr} - mostly vibrational), and the rate of energy transfer (k_{ET}). The purpose of this study is to controllably introduce multiple rates of energy transfer from the Cy3 dye to two different acceptors, namely AF647 and the gold NP. Also, we introduce a single rate of energy transfer from the AF647 to the NP. Because the proximity of donor and acceptor is directly related to the efficiency

²The values used in this equation were: $\omega_{Cy3}=3.34 \times 10^{15} s^{-1}$; $\omega_{AF647}=2.81 \times 10^{15} s^{-1}$; $\omega_F = 8.4 \times 10^{15} s^{-1}$; and $k_F = 1.2 \times 10^8 cm^{-1}$.

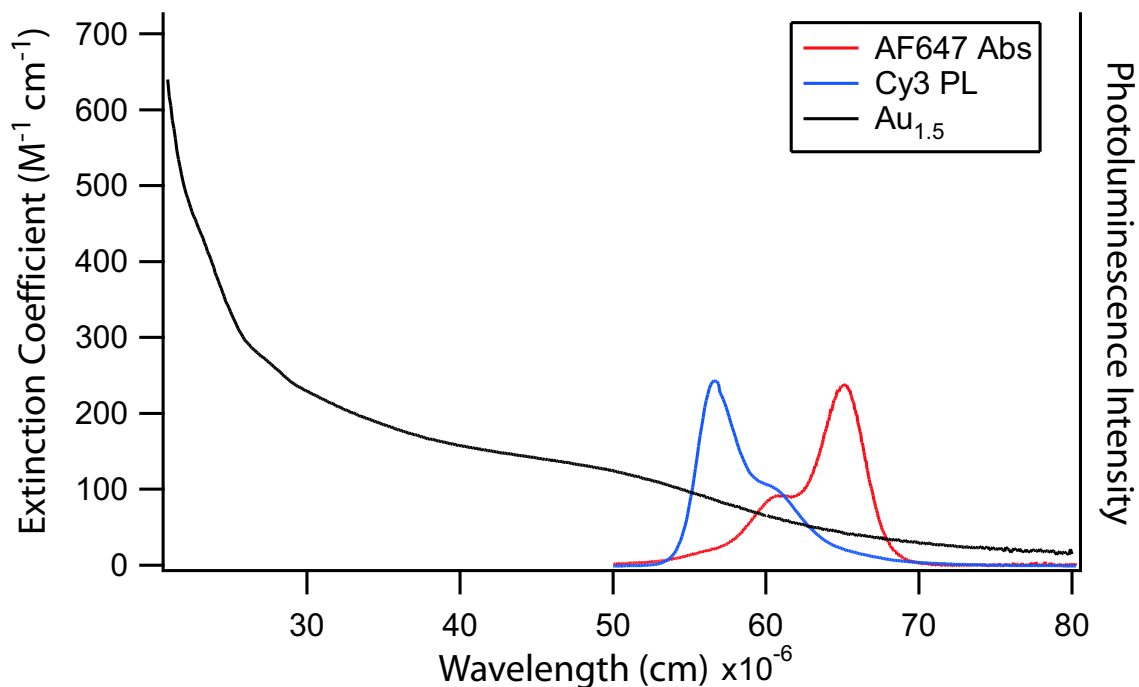


Figure 6.2: Spectra of interest for the FRET pair (Cy3 emission - red, AF647 absorption - blue) and for the NSET system (1.5 nm gold NP absorption - black.) Energy transfer occurs from the Cy3 to the AF647, where the J-overlap integral may be calculated as the area bound by Cy3 emission and AF647 photoluminescence. Both dyes transfer energy to the gold nanoparticle.

of energy transfer, and the rate of energy transfer affects the observed lifetime through the introduction of competitive de-excitation pathways, then luminescence lifetime quenching is a direct measure of D-A separation distance. The ribozyme illustration in Fig. 6.1 has multiple energy transfer pathways that are possible between probes. To examine the physics of the problem one must account for all possible energy transfer pathways, including D-A Förster pairs and D-Au SET pairs. If we consider the potential of energy transfer from Cy3 to AF647, the efficiency of energy transfer will follow a R^{-6} dependence, described classically by FRET. Because the Cy3-AF647 is a Förster pair of dyes, the efficiency of energy transfer from the Cy3 to the AF647 is dependent upon the distance between the D-A pair, where the R_0 value may be calculated theoretically requiring only the donor emission and acceptor absorption.

With these tools in hand, the measurement of observed lifetimes of Cy3 and AF647 for each system, one may calculate the separation distance between donor and acceptor using FRET theory between the Cy3-AF647 pair, and using NSET between the Cy3-NP and AF647-NP systems.

6.3.1 Analysis of Stems I and III

To perform the proper control experiments, the lifetimes of each dye must be measured individually unquenched in solution and also in the presence of each energy sink (NP and AF647). This allows us to extract the rates of energy transfer from the Cy3 donor to both the AF647 dye as well as to the nanoparticle individually before combining all rates into a single system. The same holds true when measuring the rate of energy transfer from the AF647 dye to the NP. Table 6.3.1 tabulates all of the experimental measured and calculated values for the Cy3 and AF647 dyes for all three Type I, Type II, and Type III systems.

Comparison of the data in Table 6.3.1 allows one to conclude first and foremost, that the data are not perfectly straight-forward. We see that for the Type I hammerhead complex, there are two different lifetimes reported for both the native complex (no Mg^{2+}) and different conformation complex (with Mg^{2+}). This is because the luminescence decay is bi-exponential for this system and therefore gives rise to two separate extracted decay parameters. The slow component, accounting for 32% of the total signal, shows an observed lifetime of 1.1 ns which, according to NSET theory for this dye, would mean a separation distance of about 7.4 nm. The fast component comprises 68% of the total signal and, with a lifetime of 0.2

Table 6.1: Tabulated values for the measured lifetimes of the Cy3 and AF647 dyes in the three different systems. Type I refers to the hammerhead complex involving only Cy3 and the NP. Type II refers to a FRET-like system containing Cy3 as a donor and AF647 as an acceptor. Type III is the hammerhead complex in which all parts are involved. Measured and calculated values for Cy3, which is a donor being quenched by both the AF647 and NP, are listed in the top section. Because AF647 is only quenched by the NP, only Type III hammerhead complex applies to this dye. All errors calculated from the standard deviation of three separate measurements.

			Type I Cy3 - NP	Type II Cy3 - AF647	Type III Cy3 - AF647 - NP
Cy3 $\tau = 1.57 \pm 0.09$ ns QY = 0.27 ± 0.05	No Mg^{2+}	τ_1 (ns)	(32%) 1.1 ± 0.1	0.39 ± 0.11	0.61 ± 0.17
		k_{et1} (s^{-1})	$9.45 \pm 0.75E^8$	$2.54 \pm 0.7E^9$	$1.65 \pm 0.5E^9$
		%Quenched ₁	33 ± 3	75 ± 7	61 ± 17
		Distance ₁ (nm)	7.4 ± 0.2	3.7 ± 0.3	
	Mg^{2+}	τ_2 (ns)	(68%) 0.20 ± 0.02
		k_{et2} (s^{-1})	$4.9 \pm 0.6E^9$
		% Quenched ₂	87 ± 7
		Distance ₂ (nm)	4.0 ± 0.9
AF647 $\tau = 1.54 \pm 0.07$ ns QY = 0.21 ± 0.06	No Mg^{2+}	τ_1 (ns)	(30%) 1.23 ± 0.05
		k_{et1} (s^{-1})	$1.6 \pm 0.1E^8$
		%Quenched ₁	20 ± 3
		Distance ₁ (nm)	8.7 ± 0.3
	Mg^{2+}	τ_2 (ns)	(70%) 0.25 ± 0.02
		k_{et2} (s^{-1})	$3.35 \pm 0.2E^9$
		% Quenched ₂	84 ± 1
		Distance ₂ (nm)	4.1 ± 0.1
	Mg^{2+}	τ_1 (ns)	(32%) 0.77 ± 0.2
		k_{et1} (s^{-1})	$6.46 \pm 1.7E^8$
		% Quenched ₁	50 ± 13
		Distance ₁ (nm)	6.2 ± 0.8
		τ_2 (ns)	(68%) 0.11 ± 0.02
		k_{et2}	$8.68 \pm 1.6E^9$
		% Quenched ₂	93 ± 2
		Distance ₂ (nm)	3.3 ± 0.2

... Not applicable. Either no energy transfer possible, or showed monoexponential kinetics.

† Not applicable because of multiple energy transfer processes.

ns, suggests a separation distance of 4.0 nm. The substrate strand, however, would have a calculated length of approximately 5.8 nm, which means that if correctly bound to the hammerhead complex, the maximum separation distance possible is only ~ 6 nm and not 7.4 nm. The measurement of two discrete distances is clearly a dilemma which must be resolved.

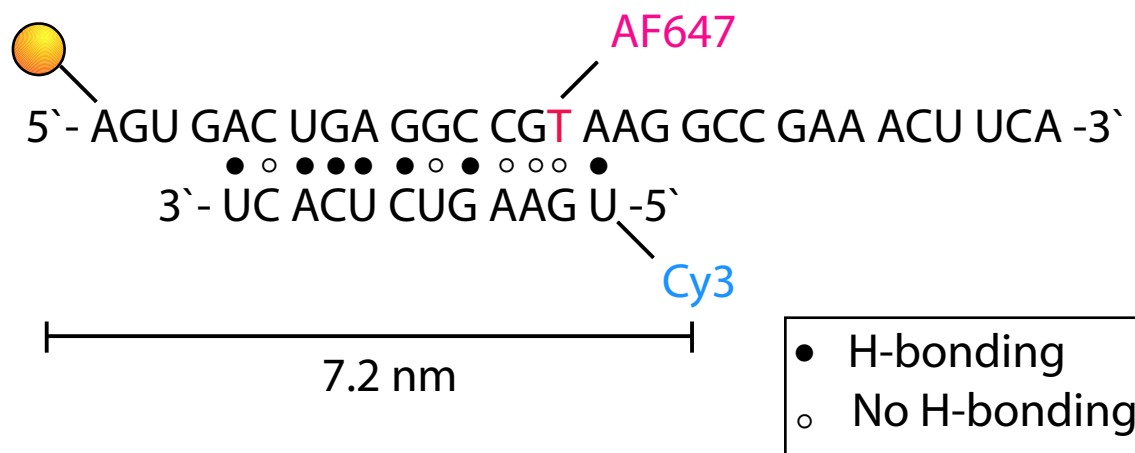


Figure 6.3: Alternate configuration scheme for substrate binding to ribozyme. Good hydrogen bonding of sporadic bases may lead to a well-stabilized secondary conformation and different separation distances between donors and acceptors. Note that in this configuration, the Cy3 and AF647 are *very* close to each other.

Figure 6.3 demonstrates a stable alternate configuration based upon base-pairing of the substrate to the ribozyme strand. In this scheme, the Cy3 dye may be separated from the gold NP by ~ 7.2 nm and would be in excellent agreement with the long lifetime component measured and reported in Table 6.3.1 in the absence of Mg^{2+} . This would suggest that the other 68% of the population in solution is in the lower energy hammerhead complex formation and is therefore responsible for the short component of the lifetime with a separation distance of 4.0 nm. Upon Mg^{2+} addition, it is known that the hammerhead complex undergoes a conformational change, and the extremities of each stem flanking the conserved core should shift in position relative to each other. Figure 6.4 shows the raw lifetime data, with bi-exponential fits through the pre- and post- Mg^{2+} sample decays. Based upon lifetimes, it would appear that there is no net change in the difference between stems I and III because the lifetime remains constant at 0.20 ns, even though the long portion of the lifetime increases

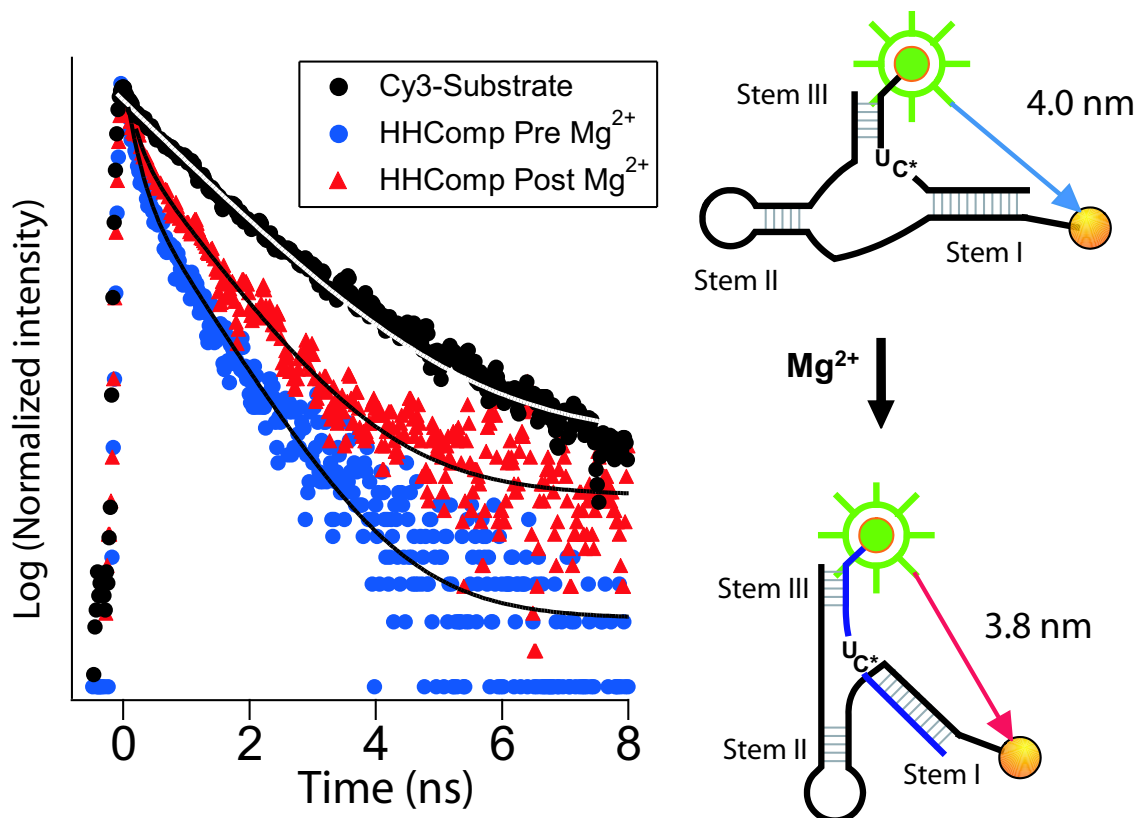


Figure 6.4: *LEFT*: Experimentally measured lifetimes of Cy3-Sub in buffer (black), Cy3 in the native hammerhead complex (blue), and after the induced Mg^{2+} dependent conformational change. *RIGHT*: Molecular scheme of hammerhead primary structure with a single dye energy transfer to a gold NP. Addition of Mg^{2+} induces a structural change and a change in the separation distance between Cy3 and the NP.

from 1.1 to 1.23 ns. Based upon FRET photoluminescence studies in the literature,^(91; 90) it is thought that stems I and III move away from each other due to an observed brightening

of the donor emission. However, it is possible that this may not be the case in reality. The brightening of solution upon the addition of Mg in the experiments presented here would have been a direct result of *alternate configuration* conformational changes, not the true hammerhead complex itself. This serves as an example of the power wielded in time-resolved studies over continuous wave photoluminescence, where the kinetics are suggestive of a different structure than that reported in literature.

6.3.2 Analysis of Stems II and III

The Type II hammerhead complex consists of only the Cy3 and AF647 FRET pair dyes, excluding the gold nanoparticle. This study allows the measurement of separation distance between stems II and III of the hammerhead complex. The Cy3 dye in the excited state should donate energy coulombically using FRET to a nearby AF647 dye molecule, where the efficiency of energy transfer should follow the relation:

$$Q_{Eff}(r) = \frac{1}{1 + \left(\frac{r}{R_0}\right)^2} \quad (6.4)$$

and R_0 is the theoretically calculated 50% (4.5 nm for Cy3-AF647) quenching value discussed earlier in this section. Table 6.3.1 shows the measured Cy3 lifetimes for this system, which were quenched and single-exponential. Comparison of lifetimes before and after Mg^{2+} addition shows basically no change in lifetimes for the Cy3 dye. Figure 6.5 shows the lifetimes of Cy3 being quenched by AF647 when no NP is present. Before the addition of Mg^{2+} , the lifetime shows an unresolvably fast component at early time, most likely a result of very efficient energy transfer to AF647 from a population of alternate conformations as mentioned earlier. The Cy3 dye would be separated from AF647 by a single basepair in this configuration and donate energy extremely efficiently to the acceptor.

We have now measured lifetimes and calculated distances between stems I and III using NSET as well as the separation distance between stems II and III using FRET. The last step is to measure and calculate the separation distance between stem II (carrying AF647) and stem I (carrying the NP) using NSET a final time.

6.3.3 Analysis of Stems I and II

Inspection of Table 6.3.1 for the analysis of AF647 energy transfer to the gold NP suggests again another dilemma. The AF647 demonstrates bi-exponential lifetimes with a 30:70 split

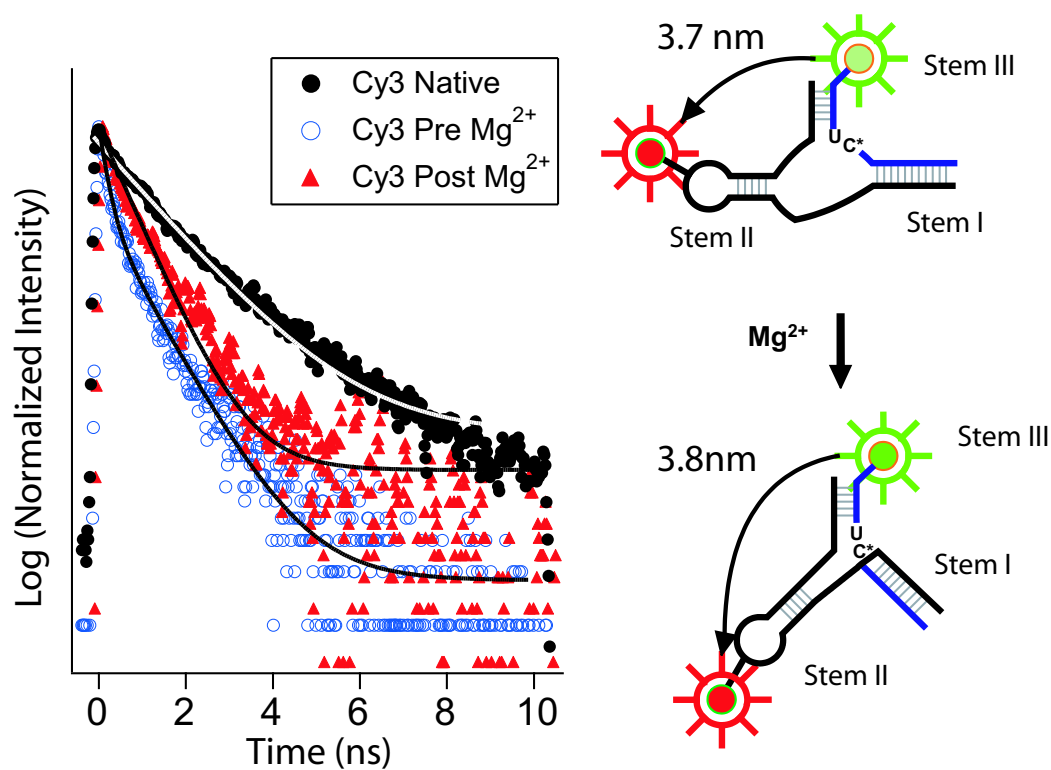
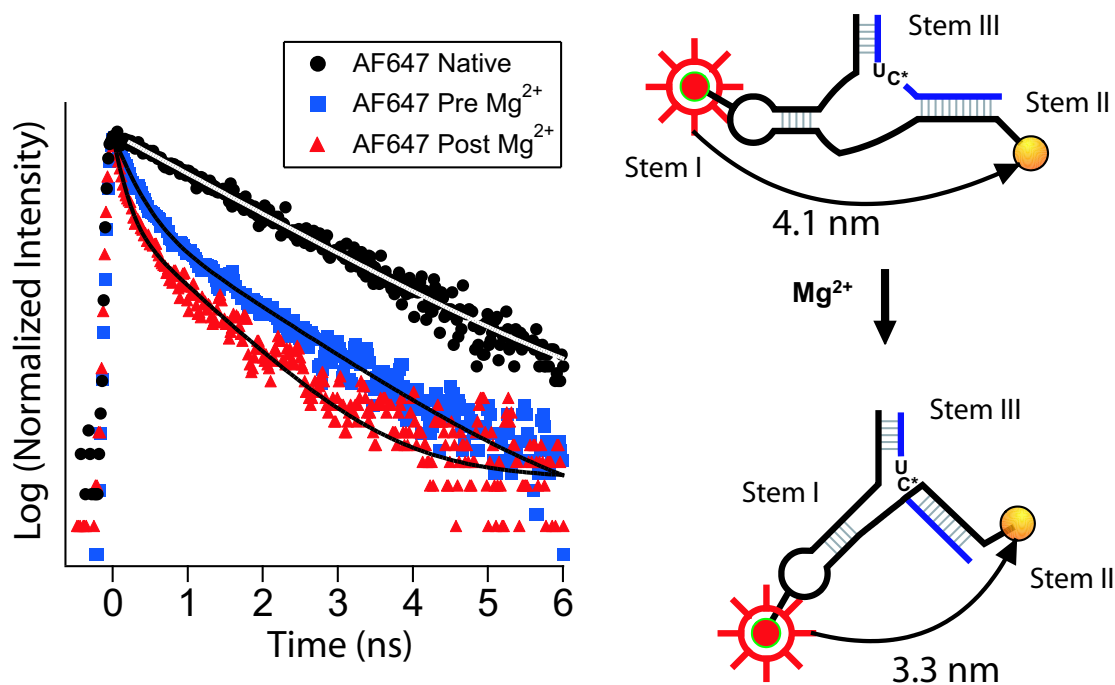


Figure 6.5: *LEFT*: Lifetimes and suggested conformational change for a dual dye - labeled hammerhead ribozyme. For the pre- Mg^{2+} scenario, a very fast component to the lifetime occurs at $t = 0$, most likely due to extreme proximity of AF647 in an alternate configuration. *RIGHT*: Suggested models for the hammerhead ribozyme where stem II moves along a plane equidistant to the Cy3 donor.



where the higher 70% accounts for the fast lifetime component. The longer component is still sufficiently shorter than the natural decay rate of an unquenched AF647 dye molecule and shortens further in the presence of Mg^{2+} , which discounts any possibility of free dye. (Free AF647 did not change lifetime in the presence of Mg^{2+} .) The answer to the dilemma of two components may possibly be gleaned through consideration of the experimental setup.

As mentioned in the experimental section, a slight excess of ribozyme strand was always added to solution as a means to insure an acceptor for every Cy3 donor. In fact, 28% extra ribozyme is the calculated excess concentration of AF647-ribozyme in which the dye is located 18 nucleotides (7.9 nm) from the 5' end containing the NP. With this realization in mind, it would be *expected* that two decay components would be observed in the lifetime of AF647 and, as calculated in Table 6.3.1, the separation distance measured is 8.7 nm. The separation distance falls to 6.2 ± 0.8 nm upon the addition of Mg^{2+} which may be accounted for by realizing that a divalent metal cation like Mg^{2+} may induce any number of conformational changes to a single stranded RNA through interactions with the negatively charged phosphate groups of the backbone.

The faster decay rates of this dual-labeled hammerhead complex arise via through-space energy transfer processes related to NSET. Figure 6.6 shows the quenched lifetimes of the AF647 dye both before and after Mg^{2+} addition. Unlike the Cy3 data shown in section 6.3.1, the dye becomes quenched much stronger after the conformational change which is suggestive of a decreased distance between AF647 and the NP. The separation distance closes from 4.1 nm with the hammerhead complex in its native state to 3.3 nm after folding.

6.4 Discussion and Conclusions

Optical methods applied to chemistry and biology are a proven fast and efficient means of analyzing otherwise difficult parameters. FRET has a strong presence in many fields related to structural characterization of small molecules. While fast and easy to use, FRET does have certain disadvantages as listed earlier. However, the power of FRET can be enhanced by coupling with NSET energy transfer techniques. In so doing, one gains the advantages of simultaneous quenching events of any dyes in the visible, (be they Förster pairs or not) along with an enhanced usable distance range. The use of NSET coupled to FRET here has allowed the triangulation of three separate base-paired helices flanking the same centrally conserved core. Figure 6.7 shows pictorially the measured values upon a cartoon scheme

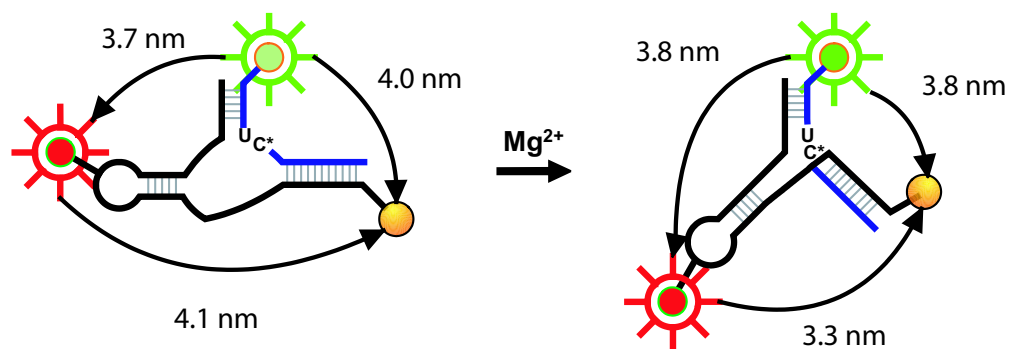


Figure 6.7: *LEFT:* The native (inactive) structure of the hammerhead ribozyme with measured distances between stems I, II, and III. *RIGHT:* After Mg^{2+} addition, the hammerhead complex undergoes a structural folding, bringing stem II into closer proximity of stem I upon a path nearly equiplanar with the original AF647 dye.

of a hammerhead complex folding event. Some of the advantages of this method over cw-PL FRET methods are first, the ability to spectrally separate out dyes from each other. Secondly, time-resolved spectroscopy allowed insight into the number of mechanisms taking place, leading to the observation of alternative conformations, a factor that would have been overlooked in traditional PL-FRET. And finally, we have demonstrated the ability to use NSET as a means of multiplex analysis within a single isolated system where, by using such techniques as time-resolved spectroscopy, it may be possible to measure multiple distance changes and reconstruct a more three-dimensional model than could be accomplished using a single FRET experiment.

CHAPTER 7

SEMICONDUCTOR NANOPARTICLES: SYNTHESIS AND CHARACTERIZATION

7.1 Introduction

Scientific research has seen a great deal of excitement centering around the development, characterization and practical utility of nanomaterials over the last couple of decades. The evolving electrical and optical properties as the dimensions of a material become confined in the nanometer scale show huge potential for use in such technologies as memory storage, display technology, catalysis, photoelectric devices, biological sensing, and others. Although nanomaterials exist in many forms depending upon the chemical makeup (metal or semiconductor) and shape (sphere, rod, pyramid, tetrapod, etc.), spherical semiconductor quantum dots (QD's), are probably the most prevalent category found in the literature. Cadmium Selenide QD's in particular have been popular because of their ease of synthesis, colorful optical properties which range from 490 - >650 nm emission, and especially their high quantum yields which have been reported at over 80%. In fact, a direct comparison of CdSe QD's with many organic dyes shows them to be superior in almost every way. Their primary advantages include: 1) No red-tailing 2) customizable optical properties 3) solubility in almost any medium 4) No Photobleaching 5) VERY broad excitation range and 6) long lifetimes. For these reasons in particular, QD's are becoming an increasingly common tool in the biological areas of cellular imaging(71; 72) and disease state detection.(73; 7; 6)

The successful integration of QD's into biological systems, however, is not straightforward synthetically because water and oxygen, which are prevalent in biology, are generally considered destructive for the optical response of QD's due to the oxidation of inorganic surfaces. The solution to the problem of interfacial oxidation has been alleviated to some degree by re-capping the QD with a separate material of either insulating (SiO_2) or of higher

band gap properties. The classic example is CdSe core QD's capped with ZnS. The re-capping of core semiconductor nanomaterials has shown desirable properties beyond protecting the surface from oxidation because it has the additional advantage of passifying the surface and filling atom vacancies that would otherwise be considered defect sites for low-energy emission.

The purpose of this chapter is to detail the synthesis of CdSe core QD materials and a characterization of the optical and physical response of the material as a function of ZnS capping thickness. The materials are characterized via powder X-ray Diffraction (pXRD), transmission electron microscopy (TEM), X-ray photoelectron spectroscopy (XPS), quantum yields (QY's), photoluminescence (PL) and lifetimes. We see that the photoluminescent energy and quantum yield of the materials are dependent upon ZnS-thickness and that the optical response for each material can be explained through relation to its physical state properties.

7.2 Experimental

7.2.1 Synthesis of Core CdSe/HDA

Core CdSe QD's were synthesized as detailed by Cumberland *et al.*(105). First, inorganic clusters of $(\text{Li})_4[\text{Se}_4\text{Cd}_{10}(\text{SPh})_{16}]$ were prepared by literature techniques(106), purified and isolated as a bluish-white powder. The inorganic cluster was measured into eight portions of 100 mg each, sealed into separate flat-bottom 10 mL glass vials containing a stir bar, and placed under high-purity argon at 90° C in an Al-block on the hot-plate.¹ 5.0 mL distilled, de-gassed hot hexadecylamine (HDA) was injected into each vial under constant stirring. The temperature was raised from $\sim 130^\circ \text{C}$ to 230°C over 3 hours time and allowed to grow for 5 hours at an average temperature of $235 \pm 5^\circ \text{C}$. The temperature was then lowered and allowed to anneal overnight at 190°C . Absorption spectra on each sample showed that six of the eight samples had exactly the same absorption spectrum, shown in Fig. 7.1.

7.2.2 ZnS-Capping of Core CdSe QD's

Purification of the core materials was accomplished by two successive precipitations with de-gassed, anhydrous methanol. The purified QD's were redispersed in minimal toluene

¹The Al-block method was developed by Jeffrey Gerbec in our laboratory and consists of eight cylindrical wells, custom-machined in a centro-symmetric pattern to fit the glass vials mentioned. This arrangement insures equal distribution of heat and rates of stirring to each vial.

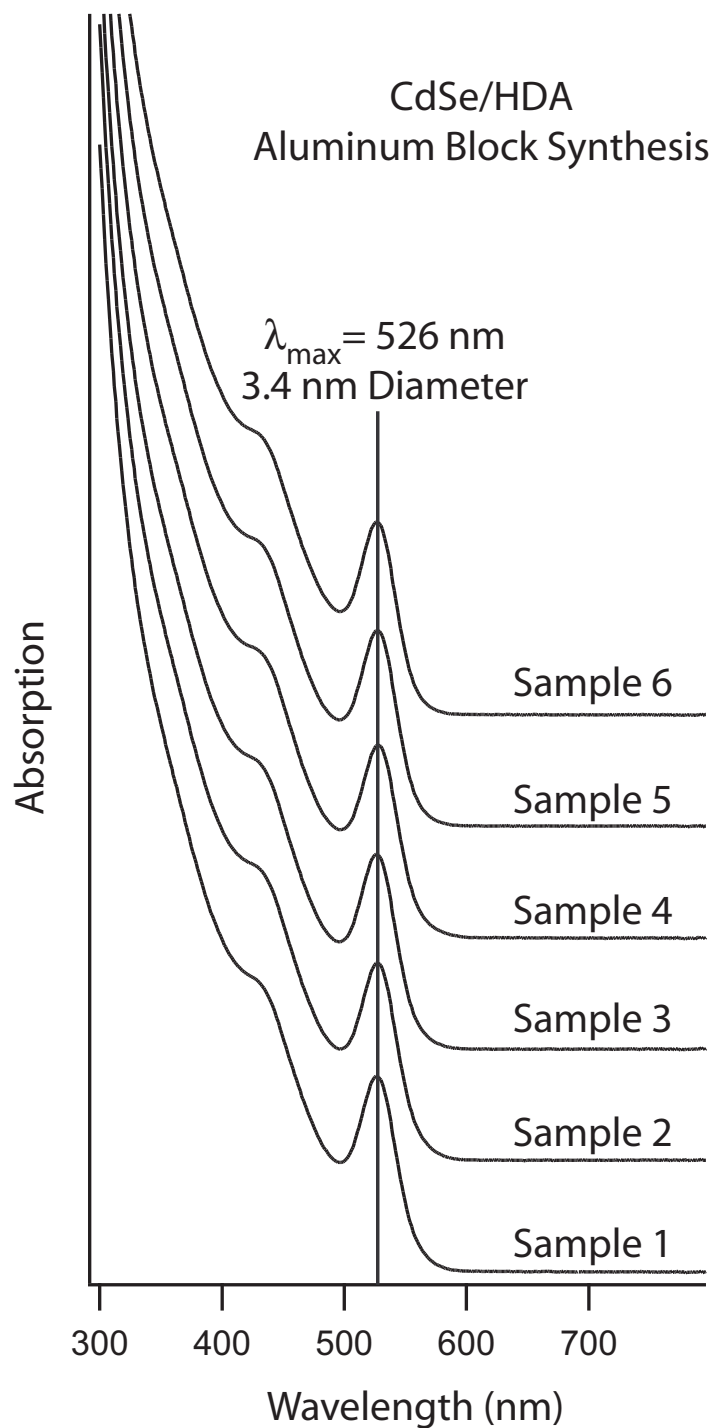


Figure 7.1: Vertically offset Absorption spectra for six samples grown under identical conditions in an Aluminum block setup. The first exciton is centered at 526 nm, which is consistent with CdSe QD's that are 3.4 nm diameter. These absorption spectra show the reproducibility of samples in the Al-block configuration.

and transferred to fresh, clean, de-gassed flat bottom 10 mL vials in the Al-block. Another 5.0 mL distilled de-gassed HDA was injected into each vial. Dry argon was blown across each vial while heating and stirring at 130° C to remove the toluene. The ZnS-capping was accomplished using a SILAR technique similar to that published by Peng(107) in which alternating injections of sulfur then zinc precursor solutions passivate the surface in an evenly distributed shell. The precursor solutions were prepared by:

- **S:** 0.5 mL trimethylsilyl sulfide (TMS Sulfide) in 8.0 mL trioctylphosphine (TOP) in 50 mL RB flask airlessly.
- **Zn:** 1.5 mL of 2.0 M dimethylzinc in toluene plus 8.0 mL TOP in 50 mL RB flask airlessly.

To accomplish different shelling thicknesses grown onto same-core size QD's, different numbers of injections were delivered to each sample. The injection procedure was performed at 220° C as follows:

- 0.25 mL S-precursor injected. Wait 20 seconds.
- 0.25 mL Zn-precursor injected. Wait 20 seconds. Repeat.

In this manner, the following samples were prepared:

- S1: No Injections
- S2: 1 Injection
- S3: 3 Injections
- S4: 5 Injections
- S5: 10 Injections

Upon shelling, the materials were glowing under ambient conditions in the hot HDA. The materials were cooled to 150° C and allowed to anneal for 2 hours before cooling to RT. To purify the ZnS-capped QD's, the materials were precipitated two times with anhydrous de-gassed methanol and then re-dissolved into molten HDA and allowed to solidify for storage.

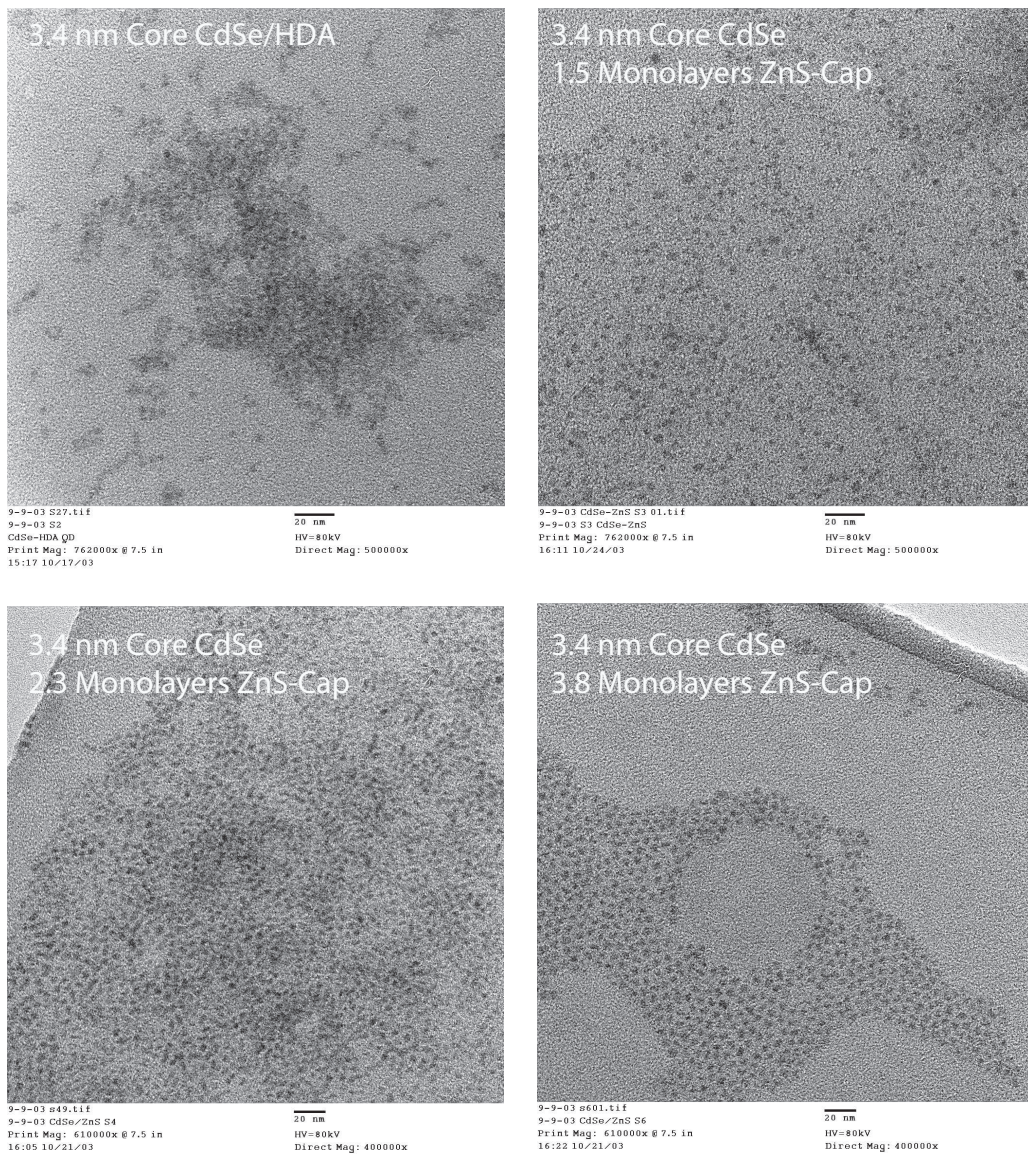


Figure 7.2: TEM pictures of CdSe and CdSe/ZnS QD's with varying shell thickness. Due to low contrast on CdSe, the core materials (*top - left*) at 3.4 nm diameter are difficult to visualize. As the ZnS shell increases in thickness to 3.8 monolayers (*bottom right*) the estimated size of the QD is considerably larger. All pictures were taken at 500000 X magnification and 80 keV acceleration.

TEM measurements, shown in Fig. 7.2, demonstrate the slight size evolution as the thickness of ZnS capping layer increases. The thickness of ZnS was calculated theoretically by taking into account the concentration of QD's in solution, the size and area of the surface for the QD, the number moles Zn or S injected, and the unit cell volumes for each material. The equation used was:

$$ML(n) = \frac{\left[\frac{\frac{4}{3}\pi \left(\sqrt[3]{\frac{4n}{\pi} \frac{3 \cdot V_{m,shell}}{N_A} * 5 + r} \right)^3 - \frac{4}{3}\pi r^3}{U_V} \right] \cdot Cores}{\text{No. Unit Cells Injected}} \quad (7.1)$$

where n is the number of injections (1 injection = (1×S) + (1×Zn)), $V_{m,shell}$ is the molar volume of the shelling material (ZnS = 2.38×10^{22} nm³/mole), N_A is Avogadro's number, U_V is the volume of one unit cell of the capping material (ZnS - 80.0 Å), r is the radius of the core QD (16.5 Å), and $Cores$ is the mole number of QD's in solution.

7.2.3 Water Solubilization: Thiocholine Ligand Exchange

The ZnS-coated materials were rendered water soluble via ligand exchange with hydrolyzed thiocholine. The acetyl protecting group was first removed from acetylthiocholine chloride by dissolving 0.3 g into a 1:4 Acetone:Water mixture. To this mixture was added 3.3 mL 1M NaOH to achieve a 2:1 ratio of base to acetylthiocholine. The mixture was stirred at room temperature for 1 hour and then neutralized with concentrated HCl to pH 7. The QD's in toluene were then stirred vigorously overnight with the deprotected thiocholine and phase extracted to the aqueous layer.

7.2.4 Measurements and Characterization

Quantum Yields: Quantum yields were measured by comparison against [Ru(bpy)₃](PF₆)₂. Absorption spectra for QD's and [Ru(bpy)₃](PF₆)₂ were adjusted so that the cross-section was ~ 0.1 at 460 nm. PL spectra were then obtained on each sample by exciting at 460 nm and measuring intensity over the entire visible spectrum from 470-800 nm. The relative quantum yield was calculated using the equation:

$$QY = \Phi_{Ref} \cdot \frac{I_{Sample}}{I_{Ref}} \cdot \frac{A_{Ref}(\lambda)}{A_{Sample}(\lambda)} \left(\frac{\eta_{Sample}}{\eta_{Ref}} \right)^2 \quad (7.2)$$

where Φ_{Ref} of $[\text{Ru}(\text{bpy})_3](\text{PF}_6)_2$ is 0.065, I is the integrated emission intensity over all wavelengths, $A(\lambda)$ is the absorption of either the sample or reference at the wavelength of excitation, and $\eta_{Ref/Sample}$ is the index of refraction for the reference (acetonitrile - 1.344) and the sample (toluene - 1.496), respectively.

XPS / pXRD: Prior to XPS or pXRD analysis, each sample was washed thoroughly by successively dissolving in minimal toluene, precipitation with anhydrous methanol and repeating the process 3 \times total. By the third wash, the thicker ZnS-capped materials became less soluble in toluene, presumably due to oxidation of Zn on the surface.

Lifetimes: All samples were cleaned by two methanol precipitations and then diluted in toluene to give an absorption cross-section of ~ 0.1 at the band edge prior to lifetime analysis. Samples were excited at 315 nm, 10 μ W, 10 ps pulses using the frequency-doubled output of an R6G dye laser. Fluorescence was collected, focused into a 0.25m imaging monochromator coupled to a Hamamatsu C5680 Streak Camera operating with a time window of 200 ns. Temporal traces were acquired by spectral binning over the central 50 nm wavelength range.

7.3 Results and Discussion

7.3.1 Absorption, Photoluminescence, and Quantum Yields

Because the purpose of this study is to analyze the change in physical and optical properties of a single-sized QD versus incremental shell thicknesses of ZnS capping, the success of such an experiment relies upon the controlled synthesis of starting materials. The Al-block method used to synthesize core QD's for this study is a convenient method for the synthesis of large amounts of high-quality QD materials, where the materials grown in each vial are identical to the materials grown in every adjacent vial on the same block. Figure 7.1 demonstrates the consistency of core growth for each vial where the position and full-width half-max (FWHM) is identical for six of eight total samples synthesized. Growth of the higher bandgap ZnS semiconductor material has a tendency to broaden and shift the energy of the first exciton absorption. Figure 7.3 shows the evolving absorption and PL spectra for the series of QD's synthesized in this study. If zinc and sulfur were diffusing into the CdSe lattice to form an alloy, there tends to be a blue-shift both the band edge and PL energies.(108; 109) However, the spectra are seen to red-shift with increased shell thickness, which is common for capped materials.(110) The lower energy of the absorbing state is suggestive that ZnS-

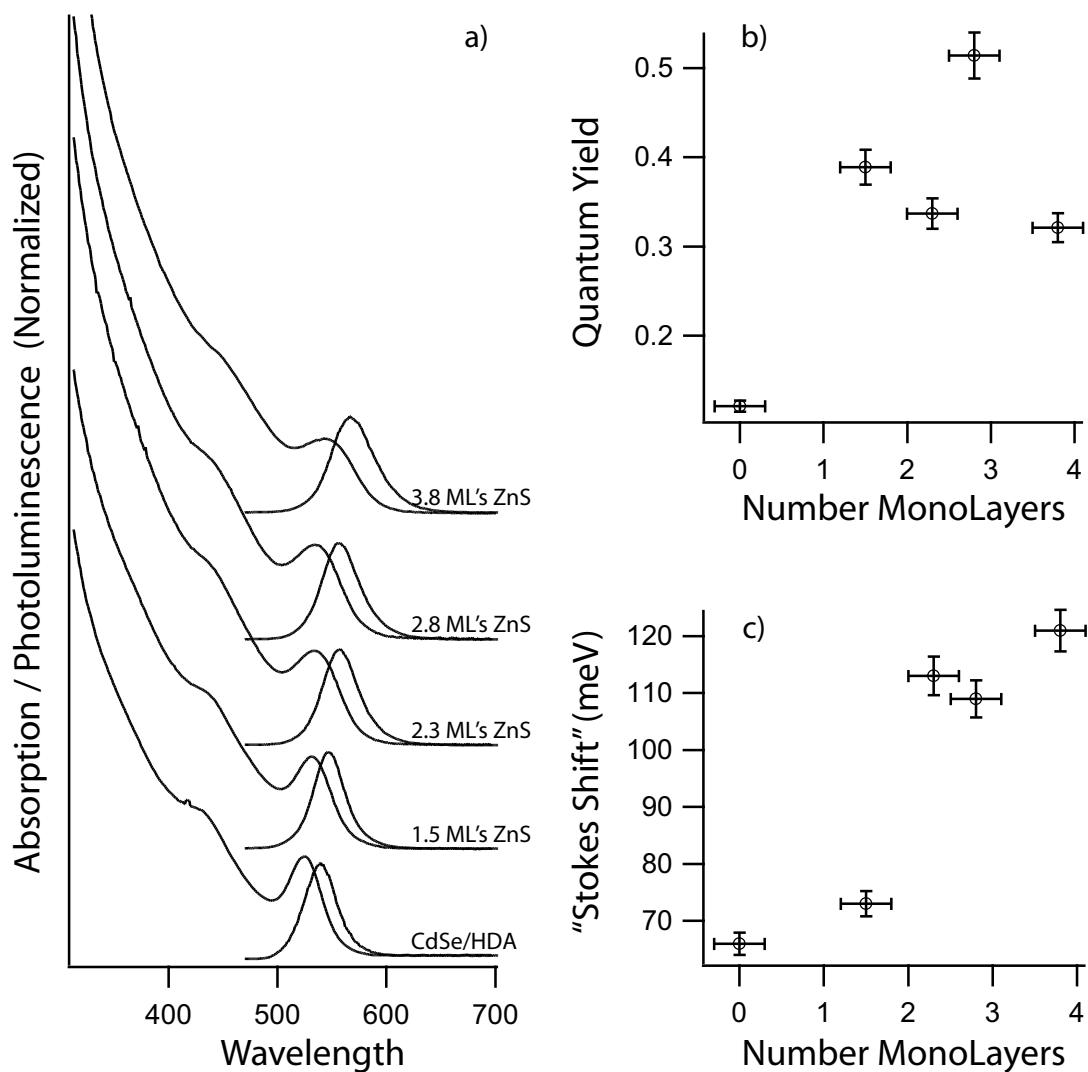


Figure 7.3: a) Offset and overlaid absorption / PL spectra for CdSe QD's as a function of ZnS-thickness. The bottom spectrum shows the spectra associated with the core HDA-capped CdSe QD's, and the spectra above show the change in properties as monolayers of ZnS are grown onto the surface. b) Quantum yields of the QD materials as a function of ZnS thickness. The medium thickness of 2.8 monolayers shows the highest QY. c) Shows the "Stokes shift" associated with different thickness of ZnS, as measured from the peak of the absorption band to the peak of the PL.

coating effects the ground-state of the QD. The broadening of the data could be explained by either a relaxation of the absorption selection rules or by a spread in the population of ZnS thicknesses, where incomplete passivation of some fraction of the materials in solution has broadened the energies of this state. Already the behavior has become intriguing, where, simply by passifying the surface of the QD with another semiconductor material, energy and energy distributions have begun to spread. Further insight into the behavior of these materials may be obtained by QY and Stokes shift calculations.

The quantum yields are observed to increase from $\sim 10\%$ uncapped to an average of 35% after ZnS-capping with a maximum QY of 51% at 2.8 ML thickness. The “Stokes shift”² is also measured to increase further with every layer of ZnS grown onto the surface. We expect that the passivation of the surface of a QD should result in less defect emission and the stronger confinement of the exciton, however only the effect upon QY seems to remain true. If the exciton were being more strongly confined, this would lead to an increased energy of absorption and emission. Therefore, this could be the basis of an argument that the wavefunction of the exciton actually leaks into the ZnS layer and is actually less confined than the core QD, which would explain the lower energies of absorption and emission. However, this does not explain the increased “Stokes shift” which becomes larger and larger as a function of ZnS thickness. Another argument may be constructed from a physical basis through comparison of the different structures of ZnS and CdSe.

The Stokes shift is a measure of the distortion of the luminescent species in the excited state before emission. Therefore, an increased Stokes shift for an emitting fluorophore is consistent with larger atomic re-organization in the excited state of that species. While ZnS exists either as zinc-blende or as wurtzite in structure, it is expected that the core wurtzite CdSe will template the growth crystal structure for the ZnS causing it also to go wurtzite. However, a comparison of the bulk lattice parameters shows that ZnS is $\sim 11\%$ shorter in bond length which would be a source of interfacial strain at the surface of the material. This strain can be imagined to exert itself upon the core QD and may be the basis for the increased “Stokes shift” measured in Fig. 7.3.

The physical characterization of the QD and the surface as a function of ZnS-thickness

²This is not a true Stokes shift. The Stokes shift is defined as the energy difference between the $0 \rightarrow 0$ vibronic absorption to the $0 \rightarrow 0$ emission feature which, for these materials, can only be measured at low temperature using line-narrowing luminescence spectroscopy. The shift reported in Fig. 7.3 is measured from the absorption maximum to the PL maximum for the ensemble in solution.

may be used to interpret the spectral properties of this series of QD's. The structural questions that we ask are: 1) How uniform is the ZnS-shell? 2) What effect does the shell thickness have upon the structure of the core QD?

7.3.2 Surface and Structural Analysis

X-ray spectroscopy is the most appropriate form of characterization to study structural and surface properties of nanomaterials because X-rays interact strongly with the nuclei of atoms. We may use XPS to analyze nanomaterials and determine the types of atoms present on the surface. In discussing core-shell materials like CdSe/ZnS, we would expect to see the sudden appearance and increased strength of energetic lines associated with the binding energies of both Zn and S core electrons with the increased shell thickness. Figure 7.4a shows comparative XPS data for all QD materials where the ZnS shell thickness is increasing from bottom to top. The strongest lines from each atom are highlighted: Zn 2p, Cd 3d, S 2p, and Se 3d. The appearance and increasing intensity of the Zn 2p line with increasing thickness of capping layer is most obvious, as is the decreasing strength of Cd 3d as it becomes buried further toward the core of the QD. Also noticeable is the increasing strength of O 1s, which, along with the observation of decreased solubility of the thicker ZnS-QD's after purification mentioned earlier, is suggestive of the formation of a significant ZnO layer. Figure 7.4b compares directly strengths of the Cd and Zn lines relative to each other where the relationship shows sigmoidal behavior with increased ML thickness. Figure 7.4c is a total comparison of all 4 species: Cd, Zn, Se, and S relative to each other as a function of ML thickness. The Cd and Se are both shown to decrease in percentage of the total signal relative to Zn and S which quickly increase to account for >50% of the total XPS signal after the first injection (1.5 ML's) of ZnS.

This surface analytical technique has shown that the CdSe cores have indeed been epitaxially passivated by the higher bandgap ZnS semiconductor. The XPS data are also suggestive that the surface has been well passivated with capping material because of the marked disappearance of the Cd and Se signals. Further, it seems that XPS is only probing the first few layers of the nanomaterial, and not analyzing the entire composition, a conclusion which may be garnered by realizing that 1) all samples were analyzed an identical period of time, and 2) by observing the C 1s line at 284.8 eV coming primarily from HDA carbon chains on the surface and should be more or less a constant. The Cd

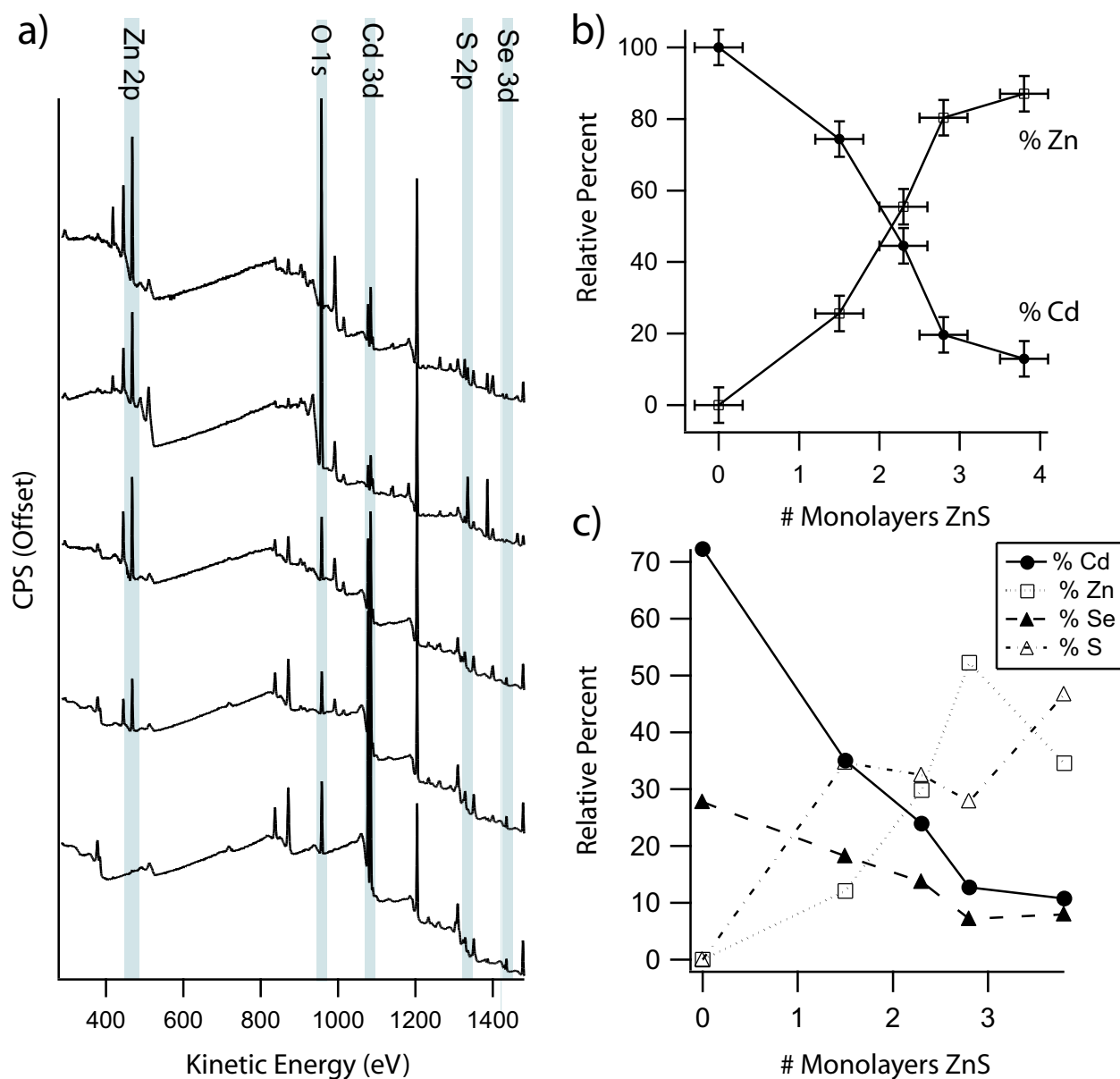


Figure 7.4: a) X-ray photoelectron spectra of CdSe/ZnS QD's. Binding energies associated with the Zn 2p and S 2p binding energies increase from bottom to top as the shell thickness increases, while the Cd 3d and Se 3d lines decrease in strength. The increased strength of O 1s at the high Zn concentrations is consistent with the readily oxidized metal. b) Comparison of Zn to Cd ratios relative to each other, where the percentage Cd decreases and Zn increases as Zn passivates the surface to a greater extent. c) Relative comparison of all species: Cd, Zn, Se, and S as a function of ML thickness.

and Zn peak heights change significantly relative to the C 1s line, which suggests that XPS is not probing the entire volume of the QD. Elemental analysis of the surface has given information regarding the chemical make-up of the QD and has proven the epitaxial growth of relatively uniform ZnS over the QD core. Additional physical information may be extracted by analyzing the structure of the QD as a function of shell thickness using pXRD.

Powder X-ray diffraction is becoming more and more a standard technique for the analysis of nanoscale materials because it can yield both structural and size information in a single spectrum. Structurally, we may determine if the material is crystalline or amorphous, and if crystalline we may determine the crystal structure. Figure 7.5 shows pXRD spectra for the different synthesized QD's as a function of ZnS capping layer. A silicon standard with three sharp lines at 1.638, 1.920, and 3.136 Å was mixed in with each sample to calibrate each spectrum for the most accurate comparison of shifting peaks. The broad peak at 3.49 Å actually contains three peaks below it: $\langle 100 \rangle$, $\langle 002 \rangle$, and $\langle 101 \rangle$. Similarly, three peaks exist closely spaced at the lower d-spacing for the $\langle 110 \rangle$, $\langle 103 \rangle$, and $\langle 112 \rangle$ peaks which are slightly better resolved from each other. The $\langle 002 \rangle$ peak of CdSe is the lattice spacing in the crystallographic axis of growth and shows the greatest shift as thicker ZnS is grown onto the surface. The $\langle 002 \rangle$ peak shifts to smaller d-spacing by 1.07 Å from the HDA-capped CdSe to the thickest (3.8 ML) capped CdSe/ZnS sample and is plotted in Figure 7.5b. The shift to smaller d-spacing is demonstrative of a lattice spacing which is becoming more and more compressed.

As was mentioned earlier, the difference in lattice parameters (6.05 Å - CdSe; 5.41 Å - ZnS)(111) is 11% and the ZnS is expected to induce strain at the interfacial boundary. The induced strain depth “felt” by the core QD could depend upon the thickness of the ZnS layer where, at some finite thickness, the compressive force induced by the ZnS will overcome the resistive expansive force pushing outward from the core. A similar model has been suggested in the literature where the compression exerted by the shelling material is thought to be responsible for the lowering of quantum yields at certain shell thicknesses.(112) Under this model, the successful *complete* passivation of a shell disallows the alleviation of core strain through reconstruction at fault boundaries. This could be responsible for the introduction of low energy self-trapped excitons (STE's) at the boundary between phases. This model would then explain an increased red-shift with thicker shells and also the observation of a QY maximum with shell thickness, beyond which the induced strain has the tendency to

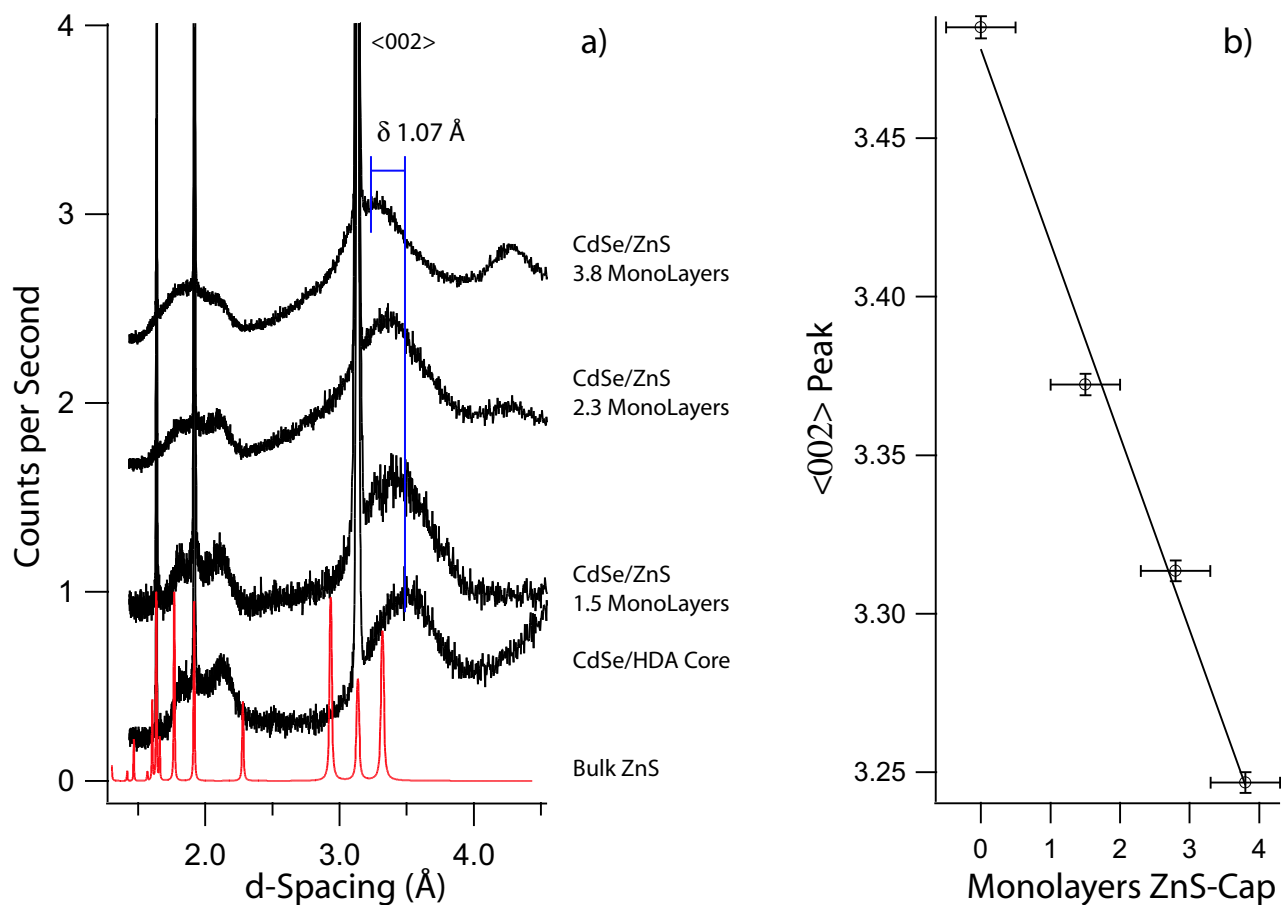


Figure 7.5: a) Powder X-ray diffraction spectra of CdSe QD's monitored by the increasing thickness of ZnS capping layer. Each sample contained a silicon standard for calibration purposes, yielding the sharp lines observed at 1.64, 1.92 and 3.13 Å in d-space. *Bottom* shows the bulk diffraction spectrum of wurtzite ZnS in d-space. b) The <002> peak extracted from Gaussian fitting plotted as a function of ZnS monolayers grown onto the surface. The lattice constant is decreasing with increased thickness of the ZnS capping material.

reduce PL efficiency.

7.3.3 Luminescence Lifetimes of CdSe/ZnS

Luminescence lifetimes of quantum dots have been a controversial subject in the literature, largely stemming from the strongly bi-exponential character in almost all QD's measured to-date. The explanations for bi-exponential lifetimes have ranged from Auger recombination(113) to trapped exciton states(114) to charged state recombination(115; 116; 117) and most recently to dot-dot far-field interactions.(118) With so many models attempting to explain the same phenomenon, I will only discuss the subject of radiative decay in light of the possibilities as related to the subject of ZnS-overcoating of core QD's.

Figure 7.6 shows the measured decay profiles for each of the samples in toluene displayed on a logarithmic scale following exciting at 315 nm. An interesting trend is observed in Fig. 7.6 in which the first few monolayers (up to 2.3 ML's) of ZnS actually *decrease* the observed lifetime of the QD while *increasing* the QY from 10% to >30%. This is particularly interesting because, of course, $QY = k_r \tau_{obs}$. This is strong evidence of a greatly enhanced radiative rate, and also means that the oscillator strength is likely increasing as well. Unfortunately, we do not have the data to assess this observation independently. Interestingly, the sample with 2.8 ML ZnS thickness shows the highest quantum yield and the observed lifetime has elongated from the lesser thickness sample. Overall, the lifetimes tend to shorten immediately upon the addition of ZnS coating, and slowly then to increase again. The shortened lifetime could be explained by the existence of a trapped state near the strain boundary of the epitaxial layer. This would essentially support the model of Chen *et al.*(112) where it is expected that the strain induced by the capping material may localize an exciton and emit from this lower energy state.

The lifetimes for the organically-passivated CdSe/HDA and the first two capping thicknesses of ZnS are obviously multi-exponential and give very good fits to bi-exponential equations. The significance of a bi-exponential equation is that it suggests two discrete excited states which depopulate to ground with the emission of a photon of light. The two thickest ZnS-capped samples, however, show nearly monoexponential decay characteristics, and could, in fact, be considered monoexponential if the ~5% size distribution is taken into account. Different sized QD's are expected to have variances in their lifetimes and this could explain the slight curvature.

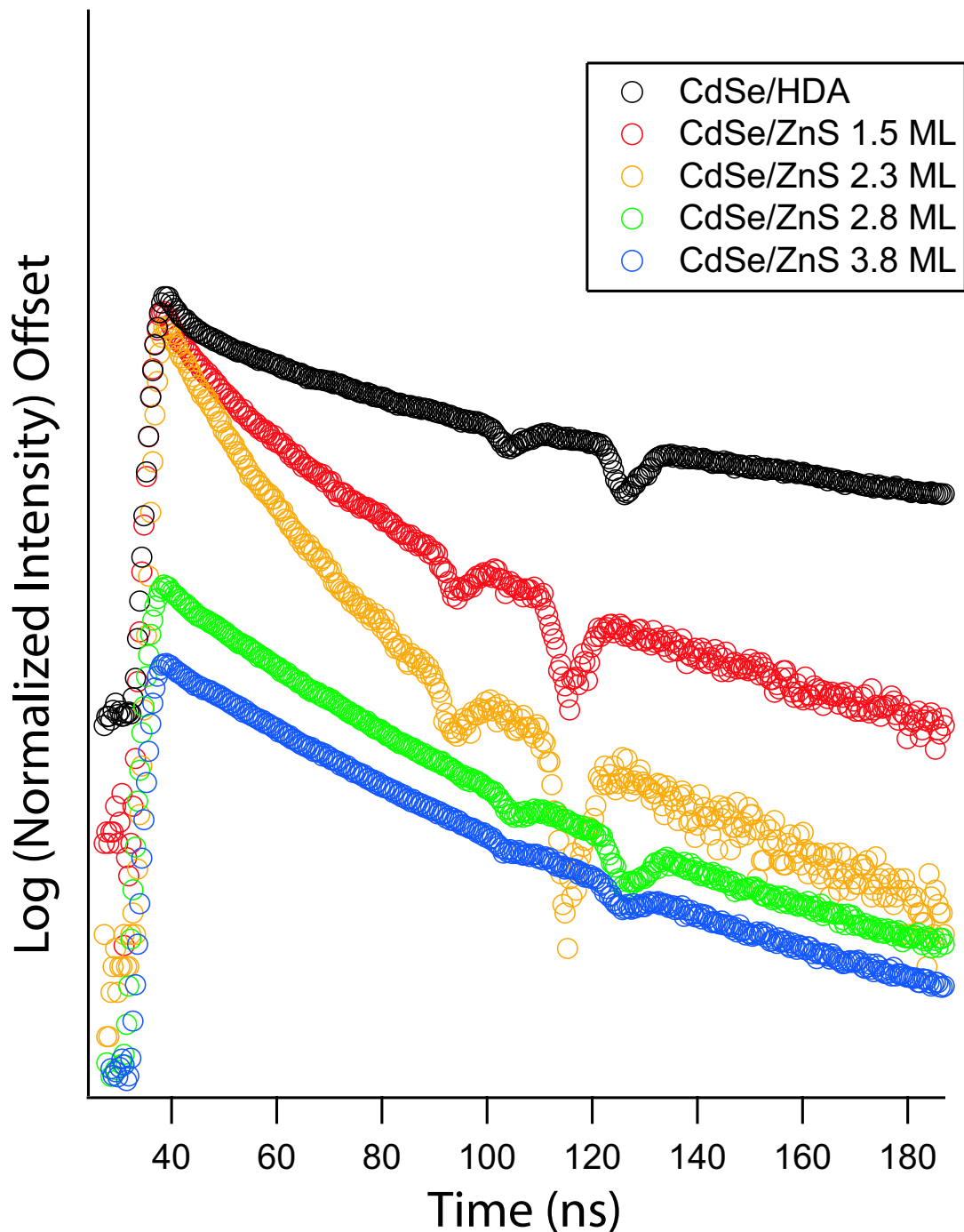


Figure 7.6: Luminescence lifetimes of the series of QD's under study. The decay traces have all been normalized to 1 at the peak and offset vertically for viewing. The topmost (black circles) decay is representative of the organically-passivated CdSe/HDA sample. Below that in descending order are the traces from the 1.5, 2.3, 2.8, and 3.8 ML thickness samples. The large dip in intensity at later time is a result of a damaged microchannel plate from the streak camera, and does not represent real excitonic decay emission.

Observation of a ML thickness at which the QY maximum and lifetime decay parameters coincide is indicative of a structure-related relationship between capping layer thickness and the optical properties of a QD. A monolayer thickness near three ML's could be the optimal growth size for a capping layer over a QD where the surface has not only been passivated but is well screened from effects related to the solvent bath such as oxidation or charge transfer. To a certain extent, these are the most important properties of concern in regards to the core QD structure if the end application is the implementation of biological conditions for imaging or optical studies.

7.3.4 Water-solubilization and Effects on Photoluminescence

If the main application of a QD is the integration with biology for sensing and imaging studies, then the most important properties to control will be the quantum yield, energy of photoluminescence, and the stability of the material. By using QD's, we have the convenient advantage over organic fluorophores to manipulate the energy of photoluminescence simply by controlling the growth size and capping layer thickness. The capping layer, therefore, has multiple usages where it is not only responsible for the high quantum yields, but also the PL energy and the protection of the core QD from the sometimes harsh environment of the outside world.

Figure 7.7 shows the absorption and PL spectra overlaid for the 2.8 ML thickness CdSe/ZnS sample after ligand exchange for thiocholine and dispersion into water. The aqueous QD has actually blue-shifted by 5 nm (557 - 552 nm; 20 meV) from the original spectrum in toluene. Most significantly, however, is the defect-free emission as evidenced in the red to infrared region where no broad, low energy intensity can be measured. This is indicative of a surface that has been well protected from the oxidizing aqueous environment and demonstrates the stability of these shelled materials. The QY was measured to be $24 \pm 3\%$ for this sample, down from the organically measured QY of $51 \pm 4\%$. The brightness of the QD was therefore reduced by 50% of its original value which suggests that either solvatochromic effects have not entirely been separated by the capping layer, or that (probable) oxidation of the ZnS-coat may be affecting the core QD non-radiatively.

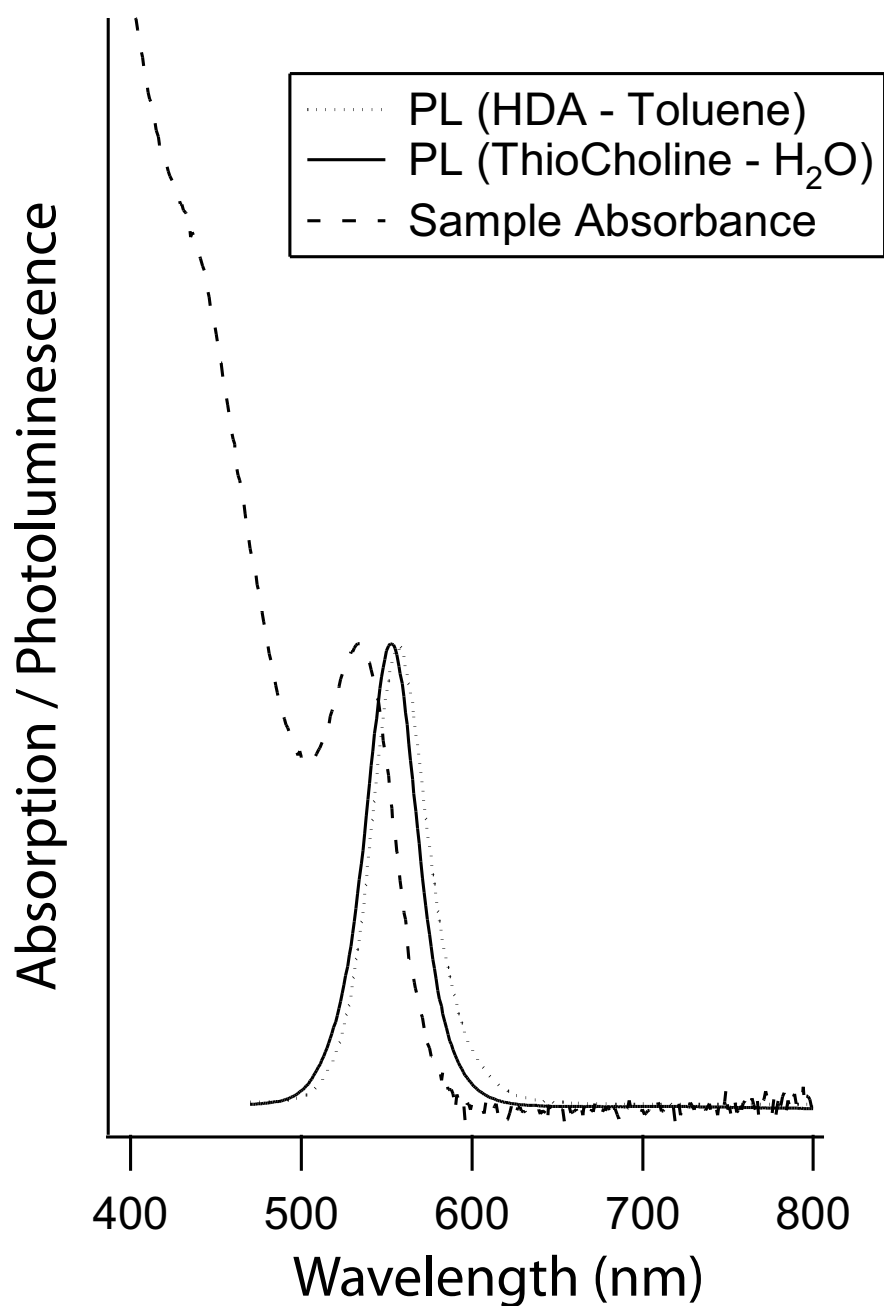


Figure 7.7: Absorption and photoluminescence spectra for the 2.8 ML CdSe/ZnS overcoated QD. The PL spectrum for the organically soluble sample is shown for comparison where the aqueous QD has blue-shifted slightly from the original spectrum. The spectrum shows that there is no defect emission, but only flat zero intensity signal going into the infrared region, consistent with a defect-free QD.

7.4 Conclusions

One size of quantum dot was controllably synthesized in six separate vials using the Al-block technique combined with cluster-route nanomaterial synthesis. The QD's were successfully overcoated with ZnS higher bandgap material via alternating injections of S followed by Zn to produce a series of QD samples all with identical cores but varying shell thicknesses. The samples were characterized physically using XPS and pXRD showing the successful overcoating with ZnS and also the changing structure presumably due to compression by the smaller lattice constant ZnS material. Photoluminescence, absorption, lifetimes and quantum yield measurements demonstrated that these materials change optically with the epitaxial growth of ZnS onto the surface of the CdSe. The changing optical properties may be explained by the reduction of surface defects along with interfacial strain incurred from overcoating of ZnS. Water-solubilization of a thickly-coated QD resulted in a 50% loss of the photoluminescence intensity, but showed no signs of defect formation in the photoluminescence. Epitaxially protected quantum dots such as these should be useful for applications to biological imaging and other similar aqueous studies.

APPENDIX A

Gold Absorption Calculations

Au_Absorption Generation.nb

2

```
Off@General::spell, General::spell1, InterpolatingFunction::dmval, FindRoot::cvnwtD;
<< Graphics`
<< Statistics`NonlinearFit`
<< Graphics`Graphics3D`
JCE2Data = 880.64`, 25.3552`<, 80.77`, 12.5552`<, 80.89`, 8.18634`<, 81.02`, 5.7015`<,
81.14`, 3.861`<, 81.26`, 2.794`<, 81.39`, 1.92542`<, 81.51`, 1.62656`<,
81.64`, 1.27176`<, 81.76`, 1.06678`<, 81.88`, 1.03516`<, 82.01`, 1.37424`<,
82.13`, 1.66054`<, 82.26`, 2.1113`<, 82.38`, 2.58044`<, 82.5`, 3.81264`<,
82.63`, 4.84438`<, 82.75`, 5.28264`<, 82.88`, 5.6492`<, 83, 5.71736`<,
83.12`, 5.73888`<, 83.25`, 5.64436`<, 83.37`, 5.6092`<, 83.5`, 5.598`<,
83.62`, 5.53816`<, 83.74`, 5.42568`<, 83.87`, 5.84584`<, 83.99`, 5.79258`<,
84.12`, 5.78034`<, 84.42`, 5.59644`<, 84.36`, 5.49486`<, 84.49`, 5.28242`<,
84.61`, 4.97628`<, 84.47`, 4.7223`<, 84.86`, 4.49008`<, 84.98`, 4.33846`<,
85.11`, 4.16328`<, 85.23`, 4.05504`<, 85.36`, 3.8922`<, 85.48`, 3.8252`<,
85.6`, 3.7102`<, 85.73`, 3.6062`<, 85.85`, 3.51`<, 85.98`, 3.3904`<, 86.1`, 3.39682`<,
86.22`, 3.32766`<, 86.35`, 3.39288`<, 86.47`, 3.17592`<, 86.6`, 3.04128`<<;
JCNData = 880.64`, 0.92`<, 80.77`, 0.56`<, 80.89`, 0.43`<, 81.02`, 0.35`<,
81.14`, 0.27`<, 81.26`, 0.22`<, 81.39`, 0.17`<, 81.51`, 0.16`<, 81.64`, 0.14`<,
81.76`, 0.13`<, 81.88`, 0.14`<, 82.01`, 0.21`<, 82.13`, 0.29`<, 82.26`, 0.43`<,
82.38`, 0.62`<, 82.5`, 1.04`<, 82.63`, 1.31`<, 82.75`, 1.38`<, 82.88`, 1.45`<,
83, 1.46`<, 83.12`, 1.47`<, 83.25`, 1.46`<, 83.37`, 1.48`<, 83.5`, 1.5`<,
83.62`, 1.48`<, 83.74`, 1.48`<, 83.87`, 1.54`<, 83.99`, 1.53`<, 84.12`, 1.53`<,
84.42`, 1.49`<, 84.36`, 1.47`<, 84.49`, 1.43`<, 84.61`, 1.38`<, 84.47`, 1.35`<,
84.86`, 1.33`<, 84.98`, 1.33`<, 85.11`, 1.32`<, 85.23`, 1.32`<, 85.36`, 1.3`<,
85.48`, 1.31`<, 85.6`, 1.3`<, 85.73`, 1.3`<, 85.85`, 1.3`<, 85.98`, 1.3`<,
86.1`, 1.33`<, 86.22`, 1.33`<, 86.35`, 1.34`<, 86.47`, 1.32`<, 86.6`, 1.28`<<;
JCKData = 880.64`, 13.78`<, 80.77`, 11.21`<, 80.89`, 9.519`<, 81.02`, 8.145`<,
81.14`, 7.15`<, 81.26`, 6.35`<, 81.39`, 5.663`<, 81.51`, 5.083`<, 81.64`, 4.542`<,
81.76`, 4.103`<, 81.88`, 3.697`<, 82.01`, 3.272`<, 82.13`, 2.863`<, 82.26`, 2.455`<,
82.38`, 2.081`<, 82.5`, 1.833`<, 82.63`, 1.849`<, 82.75`, 1.914`<, 82.88`, 1.948`<,
83, 1.958`<, 83.12`, 1.952`<, 83.25`, 1.933`<, 83.37`, 1.895`<, 83.5`, 1.866`<,
83.62`, 1.871`<, 83.74`, 1.833`<, 83.87`, 1.898`<, 83.99`, 1.893`<, 84.12`, 1.889`<,
84.42`, 1.878`<, 84.36`, 1.869`<, 84.49`, 1.847`<, 84.61`, 1.803`<, 84.47`, 1.749`<,
84.86`, 1.688`<, 84.98`, 1.631`<, 85.11`, 1.577`<, 85.23`, 1.536`<, 85.36`, 1.497`<,
85.48`, 1.46`<, 85.6`, 1.427`<, 85.73`, 1.387`<, 85.85`, 1.35`<, 85.98`, 1.304`<,
86.1`, 1.277`<, 86.22`, 1.251`<, 86.35`, 1.266`<, 86.47`, 1.203`<, 86.6`, 1.188`<<;
JCE1Data = 880.64`, -189.042`<, 80.77`, -125.3505`<, 80.89`, -90.426461`<,
81.02`, -66.218525`<, 81.14`, -51.0496`<, 81.26`, -40.2741`<, 81.39`, -32.040669`<,
81.51`, -25.811289`<, 81.64`, -20.610164`<, 81.76`, -16.817709`<,
81.88`, -13.648209`<, 82.01`, -10.661884`<, 82.13`, -8.112669`<,
82.26`, -5.842125`<, 82.38`, -3.946161`<, 82.5`, -2.278289`<, 82.63`, -1.702701`<,
82.75`, -1.758996`<, 82.88`, -1.692204`<, 83, -1.702164`<, 83.12`, -1.649404`<,
83.25`, -1.604889`<, 83.37`, -1.400625`<, 83.5`, -1.231956`<, 83.62`, -1.310241`<,
83.74`, -1.169489`<, 83.87`, -1.230804`<, 83.99`, -1.242549`<, 84.12`, -1.227421`<,
84.42`, -1.306784`<, 84.36`, -1.332261`<, 84.49`, -1.366509`<, 84.61`, -1.346409`<,
84.47`, -1.236501`<, 84.86`, -1.080444`<, 84.98`, -0.891261`<, 85.11`, -0.744529`<,
85.23`, -0.616896`<, 85.36`, -0.551009`<, 85.48`, -0.4155`<, 85.6`, -0.346329`<,
85.73`, -0.233769`<, 85.85`, -0.1325`<, 85.98`, -0.010416`<, 86.1`, 0.138171`<,
86.22`, 0.203899`<, 86.35`, 0.192844`<, 86.47`, 0.295191`<, 86.6`, 0.227056`<<;
SetDirectory@"F:\Travis\Research\Manuscripts\TeX\Final Thesis\NP_Size\Figures"D;
```

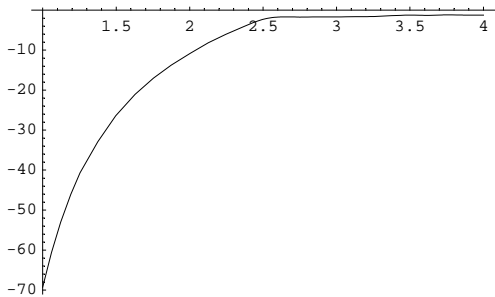
à Calculations

```

JCE2 = Interpolation@JCE2DataD;
JCE1 = Interpolation@JCE1DataD;

Plot@JCE1@ED, {E, 1, 4}, PlotRange -> All

```



```

y Graphics y

JCE2Pts = Table@{E, JCE2@E}, {E, 1.9, 4, 0.0047};
H Here I tabulate 2 values from Johnson and
Christy from their Interpolated Data in intervals of 0.1 eV L

Export@"JCInterpolatedData.txt", JCE2Pts, "Table";

h = 6.626 10^-34;
c = 2.998 10^8;
Energy@_D := h c 6.2415 10^18
10^-9
EnergyList = Table@Energy@ D, {D, 8, 200, 900, 1};

```



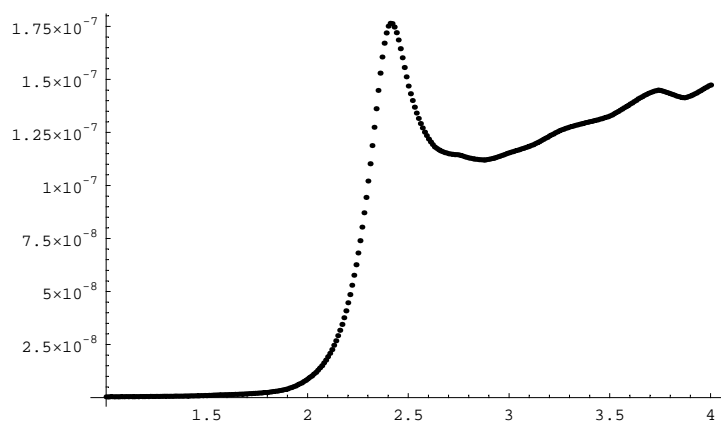
```

p = 5;
0 = h  $\frac{1.4 \cdot 10^8}{6 \cdot 10^{-7}}$  6.2415  $10^{18}$ ;

1@E_D := 1 -  $\frac{p^2}{E^2 + 0^2}$ ;
2@E_D :=  $\frac{p^2 \cdot 0^2}{E \cdot H E^2 + 0^2 L}$ ;
v0 =  $\frac{4}{3}$  H3  $10^{-9} L^3$ ;

@E_D :=  $9 \cdot v0 \cdot H1.33 L^{362} \frac{E}{c} \frac{JCE2@ED}{HJCE1@ED + 2 \cdot 1.33 L^2 + JCE2@ED^2}$ 
n = 1000  $10^{23}$ ;
Absorption@_D :=  $\frac{n @ D}{\text{Log@10D}}$ 
ListPlot@Table@8 , Absorption@ D<, 8 , 1, 4, 0.01<D, PlotRange AllD

```



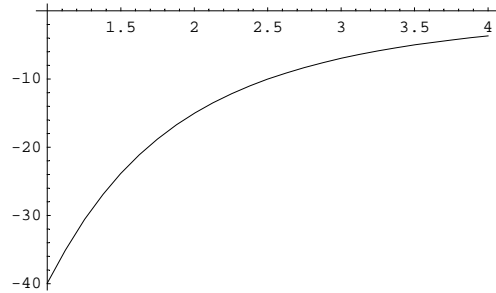
y Graphics y

```

1@2.4D
-10.8114

```

Plot@1@ED, 8E, 1, 4<D



y Graphics y

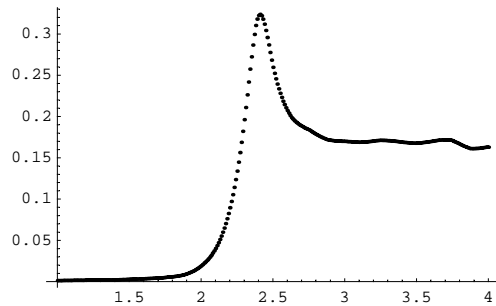
$v_0 = \frac{4}{3} H_3 \cdot 10^{-9} L^3$;

@_D := ~~JCE2@D~~
HJCE1@D + 2.66L² + JCE2@D²

n = 1000 10^{50} ;

Absorption@_D := ~~n@D~~
Log@10D

ListPlot@Table@8, @D<, 8, 1, 4, 0.01<D, PlotRange AllD



y Graphics y

JCE2@520D

JCE1@520D

4.39419×10^9

-3.30138×10^9

Energy@520D

2.38434

APPENDIX B

CPS - Kuhn Model d_0 Calculations

Au_Absorption_Generation_NPSize.nb

1

à Initialization Settings

à Calculations

```
JCE1 = Interpolation@JCE1DataD;
JCE2 = Interpolation@JCE2DataD;
1I = Interpolation@E1InterbandD;
2I = Interpolation@E2InterbandD;
1D = Interpolation@E1DrudeD;
2D = Interpolation@E2DrudeD;

Wavelength@E_D :=  $\frac{h c}{E}$  6.2415 1018

Energy@_D :=  $\frac{h c}{10^9}$  6.2415 1018

d = 6;
h = 6.626 10-34;
c = 2.998 108;
p = 8.89;

0 = h  $\frac{1.4 \cdot 10^8}{d \cdot 10^{-7}}$  6.2415 1018;

1@E_D := 1I@E_D -  $\frac{p^2}{E^2 + 0^2}$  + 1

2@E_D := 2I@E_D +  $\frac{p^2 \cdot 0^2}{E^2 + 0^2}$ 

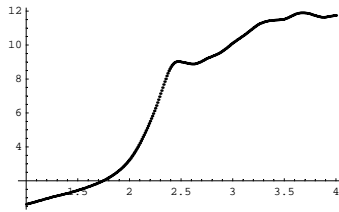
V0 =  $\frac{4}{3}$  H3 10-9 L3;

@E_D := 9 V0 H1.5 L3/2  $\frac{E}{c}$   $\frac{2@E_D}{H1@E_D + 2 \cdot 1.5 L^2 + 2@E_D^2}$ 

n = 1000 1031;

Absorption@E_D :=  $\frac{n @E_D}{\text{Log}[1.0]}$ 

ListPlot@Table@8E, Absorption@E_D<, 8E, 1, 4, 0.01<D, PlotRange AllD
```



à d0 Calculation

```
q = 0.4;
= 668;
n1 = 1.5;
n2 = 0.62;
```

$$d0 = \frac{2}{3} \left| \frac{1}{4} \frac{9 y^{10^4}}{n1} \left| \frac{4}{n1} \frac{d}{1 + 4 \frac{2@Energy@518DD}{Abs@1@Energy@518DDD}} \right| \frac{y^{10^4}}{q} \right| + \left| \frac{n2}{2} \frac{1}{n1} \left| 1 + \frac{1@Energy@518DD^2}{Abs@2@Energy@518DDD^2} \right| \frac{y^{10^4}}{y} \right| + \frac{1}{3} \left| \frac{1}{4} \frac{9 y^{10^4}}{n1} \left| \frac{4}{n1} \frac{d}{1 + 4 \frac{2@Energy@518DD}{Abs@1@Energy@518DDD}} \right| \frac{y^{10^4}}{q} \right| \left| \frac{n2}{2} \frac{1}{n1} \left| 1 + \frac{1@Energy@518DD^2}{Abs@2@Energy@518DDD^2} \right| \frac{y^{10^4}}{y} \right|$$

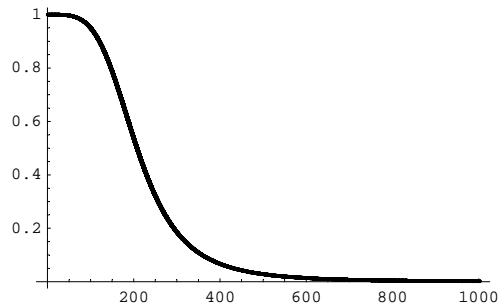
```
21.0108
```

$$\frac{1}{4} \left| \frac{9 y^{10^4}}{n1} \left| \frac{4}{n1} \frac{d}{1 + 4 \frac{2@Energy@518DD}{Abs@1@Energy@518DDD}} \right| \frac{y^{10^4}}{q} \right| \left| \frac{n2}{2} \frac{1}{n1} \left| 1 + \frac{1@Energy@518DD^2}{Abs@2@Energy@518DDD^2} \right| \frac{y^{10^4}}{y} \right|$$

```
19.7643
```

$$QEff@R_D := \frac{1}{1 + H \frac{y^{10^4}}{10^4} L^4}$$

```
ListPlot@Table@R, QEff@RD<, 8R, 0, 1000, 0.1<D, PlotRange AllD
```

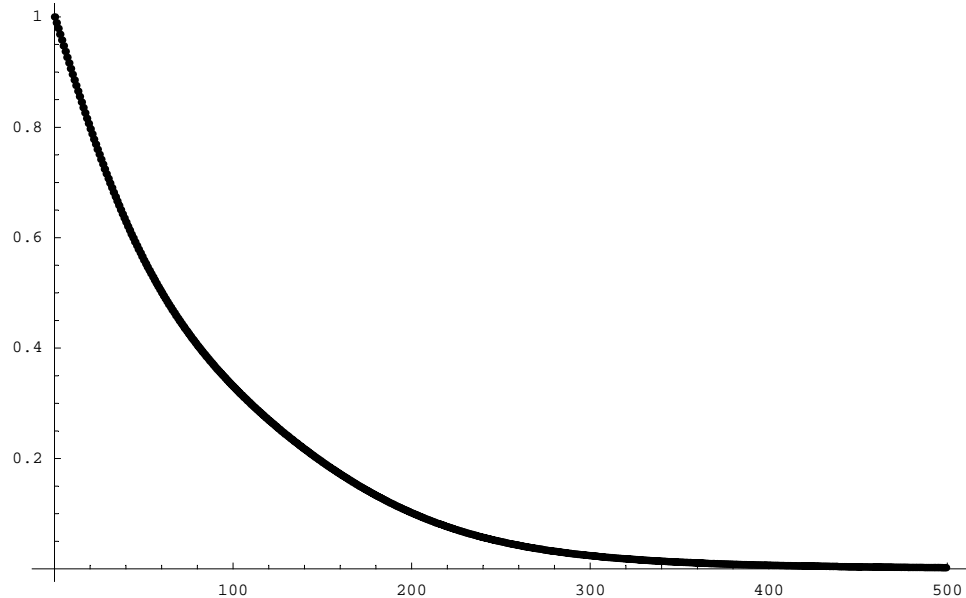


```
y Graphics y
```

```

Clear@dD;
h = 60;
Qeff@d_D :=  $\frac{2 \operatorname{ArcTan} @ \frac{h D}{800}}{2 \operatorname{ArcTan} @ \frac{h D}{800} + \frac{1}{1 + \frac{h^2 D^2}{80^2}}}$ 
ListPlot@Table@8d, Qeff@dD<, 8d, 0.01, 500, 1<D, PlotRange AllD

```



y Graphics y

```

QeffData = Table@8d, Qeff@dD<, 8d, 0.01, 500, 1<D;
Export@"Qeff_AngleIncluded.txt", QeffData, "Table"D
Qeff_AngleIncluded.txt

```

APPENDIX C

J-Overlap Integral and FRET R_0 Calculations

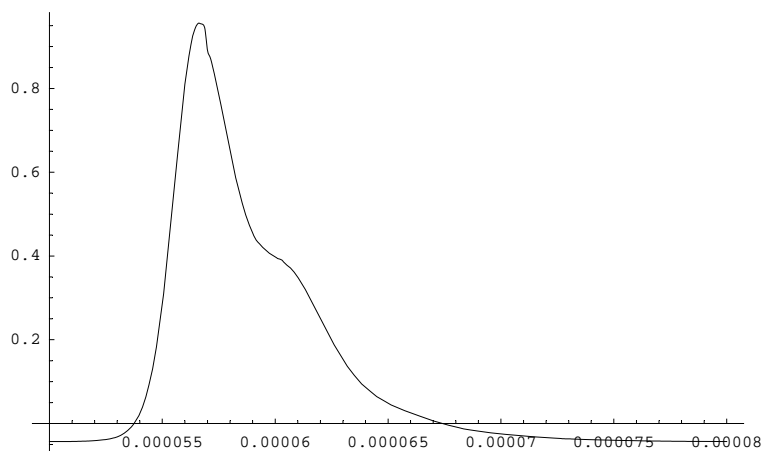
J-Overlap Integral.nb

1

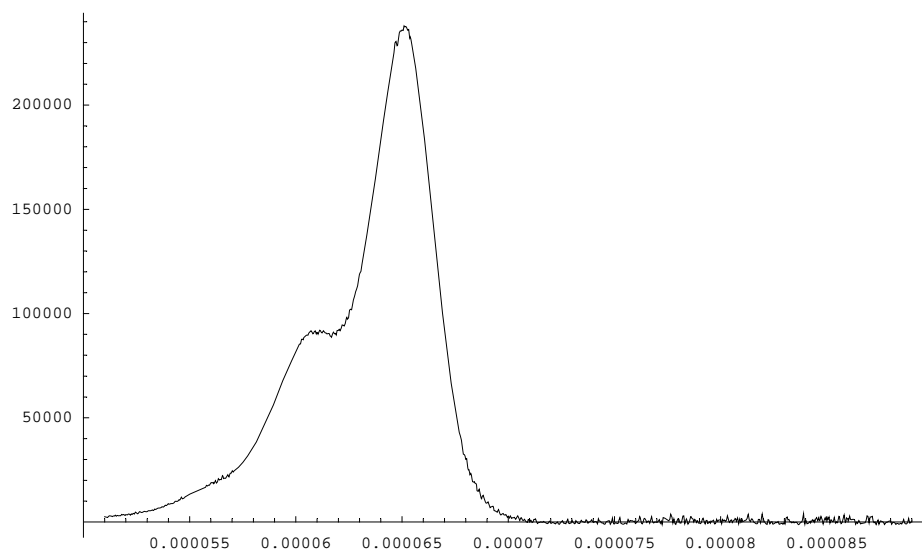
à Calculating R_0 for Cy3-AlexaFluor 647 FRET Pair

```
<< Statistics`DescriptiveStatistics`
SetDirectory@"F:\Travis\Research\RNA\HH Ribozyme\J-Overlap_Cy3-AF647"D;

Cy3PL1 = Import@"Cy3_PL.txt", "Table"D;
H This imports Cy3 PL data already in Intensity vs wavelength Hcml format L
Cy3PL2 = Interpolation@Table@{Cy3PL1[[All, 2DD], {x, 0.00005, 0.00008}, 8x, 1, Dimensions@Cy3PL1[[All, 2DD]]}
         Cy3PL1[[All, 2DD]] - Mean@Take@Cy3PL1[[All, 2DD], -10DD];
         Max@Cy3PL1D
H This Normalizes and background subtracts the PL Data L
Cy3 = Cy3PL1[[All, 1DD];
Cy3PLFin =
  Interpolation@Table@{Cy3[[x, 0.00005, 0.00008], {x, 0.00005, 0.00008}, 8x, 1, Dimensions@Cy3PL2[[All, 2DD]]},
  Plot@Cy3PLFin@ D, 8 , 0.000050, 0.00008<, PlotRange AllD;
```



```
AF647Abs1 = Interpolation@Import@"AF647_Abs.txt", "Table"DD;
H This imports the Absorption data in Extinction vs. Wavelength Hcml Format L
Plot@AF647Abs1@xD, 8x, 0.000051, 0.000089<, PlotRange AllD
```



y Graphics y

```
Overlap =
NIntegrate@Cy3PLFin@ D AF647Abs1@ D ^4, 8 , 0.000051, 0.000089<, PrecisionGoal 2Dê
NIntegrate@Cy3PLFin@ D, 8 , 0.000051, 0.0000850<, PrecisionGoal 3D
```

8.10349×10^{-13}

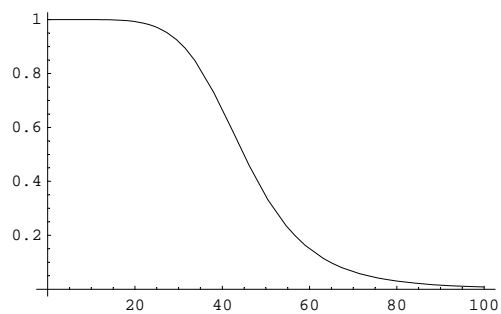
$R_0 = 9.79 \cdot 10^3 \cdot \frac{2}{3} \cdot \frac{1}{1.33^4} \cdot 0.054 \cdot \text{Overlap} \cdot 10^6$

H This calculates the Ro value in Angstroms L

44.9136

$QFRET@d_D := \frac{1}{1 + \left(\frac{d}{R_0}\right)^6}$

Plot@QFRET@dD, 8d, 0, 100<D



y Graphics y

Solve@QFRET@xD ~ 0.08, xD

88x -67.4777<, 8x -33.7389-58.4374 á<, 8x -33.7389+58.4374 á<,
8x 33.7389-58.4374 á<, 8x 33.7389+58.4374 á<, 8x 67.4777<<

QFRET@67.4777D

0.0800001

APPENDIX D

Dye Laser Alignment

General Requirements:

- Pump source should be vertically polarized beam coming into 702-dye laser. (The Vanguard is by default a vertically polarized laser, so keep that polarization going into the 702 dye laser.)
- Pump beam should saturate $\sim 80\%$ of the dye jet.
- Dye jet should be pumped at 40psi (when priming, this should be ~ 60 psi.)
- Dye reservoir should be cooled by 10°C water.



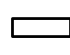
Alignment of dye-jet stream:

1. Dye tube from pump should be centered in holder, (adjusted by 2 sets of screws).
2. Nozzle in the interior of laser cavity should be at Brewster's angle relative to the incoming laser. A good guide to the eye on this is the translation screws on the tube holder. The angle is roughly the same as line drawn from set screw on right hand side through center of tube holder.

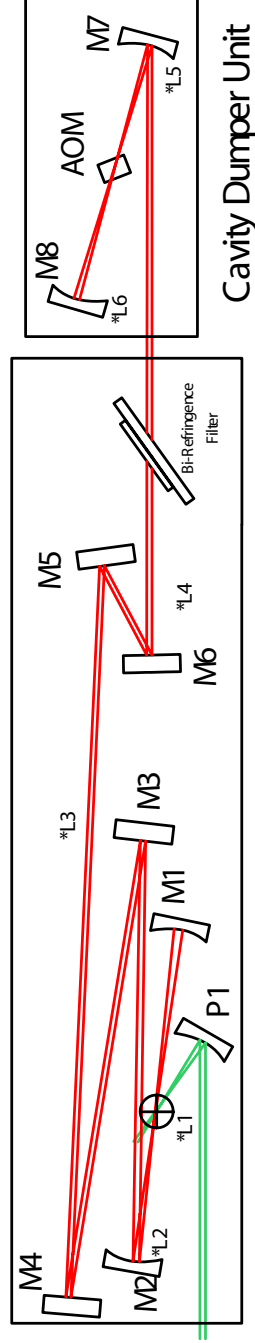
Beginning Alignment: Pump Laser into Dye Laser Cavity

1. Turn on the dye jet stream and cooler for the pump.
2. Measure the optical height of the aperture going into the dye laser on the front end and adjust the pump laser so that it is level on the same optical height. Then direct the pump laser into the dye cavity with precision-mount mirror.

3. Guide the pump beam in through hole in front of the dye laser and direct it to strike the pump mirror (P1). The pump mirror has a 50mm focal length and should focus right onto center of dye stream.
4. Adjust the dye stream (large knobs) to place the pump beam right in the very center of the jet. *NOTE: Dropping the intensity of the 532nm pump source by using an iris will greatly help in this alignment as the fluorescence is extremely bright!)
5. At this point, it is good to check the parallel alignment of the pump source into the dye laser. Do this by first dropping the intensity of the pump laser with an iris. Next, remove P1, M1, and M2 and then position the pump laser directly down the dye laser cavity by moving both the external mirror and the entire back end of the dye laser itself. The pump beam should go straight down the cavity. These should be small adjustments.
6. Cover the beam and replace all mirrors.
7. Check the alignment of the pump source into the dye jet stream again and adjust accordingly to make sure it is centered with large knobs.

-  Dye Jet-Stream
-  Focusing Mirror
-  Flat Mirror

- *L1 - Pump beam should hit top of the , P1 when entering 702. P1 should direct the focus directly into the center of the dye jet-stream.
- *L2 - The reflection from M1 should be big and round, focused right on top of the aperture for M2.
- *L3 - Beam's spot should be relatively tight and focused just above M3 as it goes down the cavity toward M5. There are 2 spots at this point which must overlap. 1 comes from the jet stream adjustment with M2, but should not be touched since this is already aligned. The other spot comes from M3. Adjust M3 to overlap these 2 spots exactly.
- *L4 - Alignment between M5 and M6 is largely unimportant since these mirrors are just for Z-adjustment, however changing the distance between M5 and M6 can be a convenient way of adjusting the cavity length later if the micrometer on the end of the cavity dumper doesn't give enough play.
- *L5 - The beam's spot from M6 should hit to the left of center on M7 to allow room for the diffracted beam on this mirror.
- *L6 - The beam's spot from M7 should hit to the left of center on M8 also to allow room for the diffracted beam on this mirror.



702-1 Dye Laser

Cavity Dumper Unit

chch

Alignment of Dye-Laser Cavity

1. Begin by removing all lossy-reflective surfaces not required for lasing, ie. the AOM crystal and the bi-refrarence plate.
2. Remove all mirrors and clean them with pure EtOH or MeOH using lint-free lens paper.
3. M1 and M2 should have 160mm length between them with M2 about 150mm from the dye jet stream.
4. M1 is collecting fluorescence from the dye and focusing it into M2. In the absence of lasing, you should see a large yellow spot appearing around the aperture in front of M2. Center this spot over the aperture. If this spot is not visible, adjust the vertical alignment of M1 until the round yellow spot appears near M2, and then center it over the aperture.
5. Just over the top of M1, using a card, find 2 yellow spots focusing down the cavity toward M3. Translate M2 forward and back slightly so that the focus of its spot is fairly tight, (do not make it too tight, back off a little from that.)
6. Next adjust the position of M1 using small knobs around the invar bar until the 2nd spot overlaps the spot from M2. Both spots should be overlapped, going down the center and should strike M3.
7. M3 is a flat mirror and should be positioned at the "D" position (for cavity-dumped mode) as marked on the invar bar.
8. Adjust the alignment of M3 so that it reflects the beams to the center of M4.
9. M4 is another flat mirror which sends the beam to M5, then M6 which finally sends it into the cavity dumper. (M5 and M6 are also both flat mirrors only used for z-adjustment to place the beam on axis with M8. M7 is an output coupler and therefore is not used in this configuration.)
10. Align M4 to place the spot in the center but near the top of M5.
11. Align M5 to place the spot in the center of M6.

12. Align M6 to place the spot onto the center left-hand side of M8.
13. Align M8 to place the spot onto the center left-hand side of M9.
14. While watching M4, (don't use a card - for obvious reasons - or at least it will be obvious when you try), align M9 so that the reflected spot coming back through the cavity overlaps the reflected spot from M3.
15. At this point, all mirrors should be more or less aligned with each other if all spots are overlapping and the cavity length is the last thing to adjust. Do this first by using the micrometer adjustment on the end of the cavity dumper unit.
16. If, after translating the cavity dumper throughout the entire range, there is still no lasing, translate M6 forward or backward (your guess is as good as mine, just be consistent and know which way you went.) and refocus the cavity starting from step [11](#).
17. Re-adjust the cavity length again with micrometer adjustment on cavity dumper unit.
18. You should notice that you are getting close to the lasing requirements when you see brief flashes of light. This is most noticeable in the large spot of light reflecting from the dye jet-stream onto the ceiling.
 - A side note: This beam reflecting off the dye jet-stream can be **very** helpful in understanding the mode quality of the laser. (A side-side note: There are actually two beams reflecting upward here, one from the front face and one from the back of the jet stream - so don't be alarmed by that.)
 - This spot for a perfectly aligned dye laser will be large, *structureless* and round. Any structures that look like clover leaves, donuts, circle halves, or George Bush mean that you have demons inside the laser causing it to do stupid things.
 - Playing with the large dye knobs which align the jet-stream relative to the pump laser are the best way to correct this, assuming the rest of the cavity is aligned properly.
 - EVERY time you align the laser, or even adjust the power, monitor this (these) ceiling spot(s)!

19. Once the laser has begun to lase, maximize the intensity to the eye by adjusting the cavity length and by using the large dye-stream adjustment knobs. Always watch the spot on the ceiling to make sure that it remains round and structureless.
20. At this point, replace the bi-refrident filter and readjust the cavity length to maximize intensity to the eye.
21. Finally, replace the AOM crystal at the Brewster angle as marked on both the crystal holder and the holder mount. Again, adjust the cavity length to get lasing.

APPENDIX E

Streak Camera Operation

Turning on the Computer and Lasers

1. If computer is not off when you start, it may need to be restarted in order to communicate with Streak Camera.
2. Turn on Hamamatsu Power Supply Unit C5680.
3. Turn on Camera Controller C4742-95.
4. Turn on Synchronous Delay Generator C4792-02.
5. Turn on Monochromator.
6. Turn on Computer.
7. While computer is booting up, turn on both the chiller and pump to the dye laser, making sure to get ~ 40 psi pressure when pump is in “Jet” mode.
8. Once the computer has entered Windows, double-click the “Vanguard” icon on the desktop.
9. Click “OK” to start the Vanguard laser control window.
10. Click and hold the large blue “On/Off” Button until the button turns red and the word “Emission” appears.
11. Click and hold the “Shutter” button until the square above it turns red. In about 30 seconds, the green laser should appear out of the Vanguard Laser.

12. Go around to the other side of the table and find the ThorLabs photodiode, located in front of the Hamamatsu pin photodiode. Turn this photodiode on with the switch in the back.
13. Once the photodiode is on, make sure that the seeded Vanguard 532nm laser is hitting the center of the photodiode. If the photodiode is working correctly, the BNC Universal Pulse Generator should have a blinking red light labeled “OVLRLP”. This is normal and good. If this light is not blinking, plug the photodiode into the oscilloscope and check to make sure it is aligned properly by adjusting its position. The peak height needs to be at least 300mV to trigger the BNC Pulse Generator. If there is still no signal out of the photodiode, the battery must be replaced with another 23A 12V battery.
14. The purpose of the BNC Pulse Generator is to drop the rep rate from 76MHz, which the 7200 Cavity Dumper cannot use, to 19MHz, which can be used. (38MHz, as it turns out, is unstable for the Pulse Generator - don’t know why.) The settings on the BNC Pulse Generator should be:
 - (a) Trigger: External 300mV.
 - (b) Timing: Delay 43ns, Width 13ns
 - (c) You can check the stability of the output by probing the “Pulse Out” with the oscilloscope. It should give you a rock-steady square wave operating at 19MHz. (Make sure to replace the cable going from “Pulse Out” on the Pulse Generator to the “38MHz IN” on the back of the 7200 Cavity Dumper when finished probing.)
15. Next, turn on the power to the Coherent 7200 Cavity Dumper.
16. Turn the power to the RF switch all the way up. Now the laser from the 702-Dye laser should be dumped out the back of the cavity.
17. Next, turn the Cavity Dumper to $\div N$ Mode. The default is 10, which means that if the BNC Pulse Generator is giving 19MHz, you now have 1.9MHz hitting the sample which is a pulse about every 500ns. Tune the $\div N$ number to give you whichever repetition rate you desire, (How long do you want between consecutive pulses in the pulse train? Keep in mind that the more you divide it, the lower the repetition rate, the greater the pulse power. This can be a good thing.)

Using the HPD-TA Software

1. Back on the desktop, double-click the “HPD-TA 32” icon to start the software which controls the Streak Camera.
2. Click “OK” in the window which appears to connect to all devices and setup the Streak Camera. If there are any errors before getting into the software, turn off the Vanguard and restart the computer. Next time you start up, everything should work correctly.
3. Once inside the HPD-TA software, go into “Live” mode by clicking the camera icon on the tool bar. Click ”Live” on the small window that pops up to turn on the CCD.
 - NOTE: ALWAYS watch what is happening to the CCD because this is what is happening to your MCP and Streak Tube. If at any time you see RED, this is BAD. Follow the instructions below and back off if you ever see anything RED appearing on the screen.
4. On the 4792-01 Control window, change the “Trigger Mode” from Internal Trigger (default) to Dump Mode.
5. On the C5680 Control window, change the MODE from “Focus” (default) to “Operate.” This starts the streak tube operating to give a time range as designated by the box above MODE. When you do this, a green light on the back of the Streak Camera should come on under the “Trig’d” sign. If this light does not come on, or comes on flashing, then you are having trigger problems. Probe both the ThorLabs photodiode and the Hamamatsu pin photodiode to make sure both are responding correctly. Adjust the positions of each accordingly if need be.
6. It is best to start off at a time window that will allow you to easily see the signal at the rep rate of the cavity dumped laser. Change the Streak Time to $\approx 200\text{-}500\text{ns}$.
7. *MAKING SURE THAT THE STREAK CAMERA SHUTTER IS CLOSED IN THE SOFTWARE*, place a scattering sample in the sample holder (I’ve been using CdO in MeOH.) See that your laser light is being scattered and refocused across the slit of the monochromator. All directions after this assume decent alignment of collection and focusing optics.

8. Make sure the MCP Gain is set to zero.
9. Still on the C5680 Control window, click SHUTTER from “Closed” to “Open.”
10. On the Chromex 500is Control window, set the wavelength to match (in the ballpark), the wavelength of your laser, (560nm-620nm).
11. Also on the Chromex window, change the slit value from 0 to 10 μ m. This opens the slit and this is the first time you should see anything on the screen.
12. If you don’t see anything on the CCD in Live mode immediately, click the * - asterisk button on the menu bar above. This automatically sets the LUT (Look Up Tables) to adjust for the brightest signal coming into the CCD.
13. If you still don’t see anything, adjust the monitor so that you can see it across the laser table, and go to the Cavity Dumper Controller and begin clicking the “Delay” toggle switch down (-). Do this 1-10 times. If still you don’t see any signal on the screen then first check and make sure all of your settings are correct, (1394ORCA: Live Mode, C4792-01: Dump Mode, C5680: Operate Mode; 200-500ns Time Range; Shutter Open, Chromex: Wavelength (560-620nm); Slit=10).
14. If all of these are correct, then either open the slit width up, (shouldn’t have to go above 50 μ m) or change the MCP Gain setting to 10 and find your laser pulse by playing with the Delay on the Cavity Dumper. Again, MAKE SURE TO PROTECT THE CAMERA AND CCD AT ALL COSTS.
15. Once you’ve located the laser pulse, move it to the top of the screen by clicking Delay on the Cavity Dumper.
16. At this point, if your desired Time Range is 20 ns or less, then go straight to the 20 ns time window in the software, and again find the laser pulse by using the Delay Toggle on the Cavity Dumper. (The 20 ns window is the smallest window you can use and still find the pulse using this course delay switch, which delays the pulse by 13 ns per toggle. Think about this, it makes sense.)
17. From here on in, you will need to use the software delays.

18. Starting at the 20ns range, use the C4792-01 window, “Dly1 DumpMode” to delay the laser pulse up the screen. Do this by holding “Shift” and hitting the “UP” arrow until the laser pulse has gotten near the top.
19. You can use the “Dly2 DumpMode” in the same manner for fine adjustment. This Delay has only about an 11ns range, so you must already be close to the total delay desired before using this delay.
 - TRICK: Because the delay on the cavity dumper gives 13ns per click downward, if you cannot get the pulse quite to the top of the screen using Dly2, then reset Dly2 to zero and click downward once on the cavity dumper delay toggle, (saves you 2ns). Now begin to use Dly2 again and you will have much more room.
20. Once you’ve zoomed in very close to the laser pulse, ie. 20ns-1ns windows, you may notice that the laser pulse(s) starts looking funky. Any pulses separated by 13ns are possibly being leaked by the cavity dumper. These can be adjusted by using the “Fine Delay” knob on the Cavity Dumper. Use Fine Delay to center the Cavity Dumper’s window over the peak that you desire while monitoring the streak camera in Live mode.
21. If the peak looks like closely-spaced peaks near or overlapping each other on the screen, these can often times be adjusted using the “Level” knobs on the C4792 Delay Generator. While watching the monitor, adjust the “Level” knobs under “Mode-Lock Clock” and “External Trigger”. The pulse(s) should change and sharpen up on the screen. If you still cannot get them sharp, then probe both photodiodes (ThorLabs and Hamamatsu) across the oscilloscope to make sure that they are triggering correctly.
22. When the laser pulse is sharp and at the top of the screen for the desired time range window, you are ready to take a streak image of your sample.

Measuring the lifetime of a sample

1. *Before* placing the sample in the sample holder, close the slits, turn down the gain, and think about the following:
 - (a) What wavelength will the sample absorb? (You can only excite from 560-630nm in the visible, or from ~285-310nm in the UV.)

- (b) What wavelength must the monochromator be centered at to view the photoluminescence?
 - (c) How much power are you applying to the sample? (You most likely want powers in the μW , which means that for the visible wavelengths, ie high powers from the dye laser, you will need a LARGE amount of neutral density to attenuate the beam power before exciting the sample.)
 - (d) If you are exciting in the visible, do you have an appropriate filter to reject the laser line?
2. After considering all of the above, make sure that they *happen* before trying to see your sample and take a lifetime.
 3. With your sample in the cuvette holder, the monochromator centered at the correct wavelength to see photoluminescence, and the laser power attenuated to appropriate powers, put the Streak Camera software into “Live” mode. Open the slits on the monochromator to between 10 - 100 μm and put the gain at 63, (the maximum gain possible.)
 4. You should see flashes of light on the CCD, scattered around the central wavelength of your sample, (this takes some getting used to, especially for weak-emitting samples.)
 5. If there is any need to adjust the focus of the optics to maximize signal, now is a good time to do it, assuming there is decent signal coming from the sample.
 - Note: The UV takes a slightly different path to the sample than does the visible. This means if you focused onto your visible laser line, when you place in a sample to be excited in the UV it may need some *fine* adjustment of the focusing optic in particular.
 6. If there is decent signal coming from the sample, then click “Freeze” on the “Live” mode window, and then choose the “Photon Counting” tab.
 7. Choose the number of Frames you would like to collect in order to get the desired signal to noise, (if you choose a large number of frames you can always stop the collection early. Alternatively, if you choose a low number of frames, you can click the “Clear

on Start up” box and, without changing anything about the system, begin photon counting again on top of your current data without deleting your previous run.)

8. To start a run, click the button ”Count”. At this point, you may sit back and enjoy your favorite vice for up to a couple hours. (Although I would suggest starting another project!) If it is a weakly emitting sample, a lifetime can take hours to collect.
9. When a lifetime has been collected, you can save not only the image file, but also a certain profile over the desired wavelength range by clicking “Data” and then “MX” (where “X” is the number of the channel storing your profile data.) This brings up a window with tabulated ASCII data which may be copied and saved into a text file using NotePad or any other text-based program.
10. Now go fit the data and write the paper!

REFERENCES

- [1] Brus, L. E. *Journal of Chemical Physics* **1984**, *80*, 4403-4409. [1](#)
- [2] Nguyen, H. L.; Howard, L. E. M.; Giblin, S. R.; Tanner, B. K.; Terry, I.; Hughes, A. K.; Ross, I. M.; Serres, A.; Burckstummer, H.; Evans, J. S. O. *Journal of Materials Chemistry* **2005**, *15*, 5136-5143. [1](#)
- [3] Hanif, K. M.; Meulenberg, R. W.; Strouse, G. F. *Journal of the American Chemical Society* **2002**, *124*, 11495-11502. [1](#)
- [4] Nayfeh, M. H.; Eurell, T. E.; Braun, P. V.; Gelfand, V.; Yu, W. M. *Biophysical Journal* **2004**, *86*, 149a-149a. [1](#)
- [5] Smith, T. L.; Witt, A. N. *Astrophysical Journal* **2002**, *565*, 304-318. [1](#)
- [6] Kim, S.; Lim, Y. T.; Soltesz, E. G.; De Grand, A. M.; Lee, J.; Nakayama, A.; Parker, J. A.; Mihaljevic, T.; Laurence, R. G.; Dor, D. M.; Cohn, L. H.; Bawendi, M. G.; Frangioni, J. V. *Nature Biotechnology* **2004**, *22*, 93-97. [1](#), [5.1](#), [7.1](#)
- [7] Wu, X. Y.; Liu, H. J.; Liu, J. Q.; Haley, K. N.; Treadway, J. A.; Larson, J. P.; Ge, N. F.; Peale, F.; Bruchez, M. P. *Nature Biotechnology* **2003**, *21*, 41-46. [1](#), [5.1](#), [7.1](#)
- [8] Plank, C.; Schillinger, U.; Scherer, F.; Bergemann, C.; Remy, J. S.; Krotz, F.; Anton, M.; Lausier, J.; Rosenecker, J. *Biological Chemistry* **2003**, *384*, 737-747. [1](#)
- [9] Lavine, M.; Vinson, V.; Coontz, R. *Science* **2005**, *310*, 1131-1131. [1](#)
- [10] Xu, X. H. N.; Brownlow, W. J.; Kyriacou, S. V.; Wan, Q.; Viola, J. J. *Biochemistry* **2004**, *43*, 10400-10413. [1](#)
- [11] Voura, E. B.; Jaiswal, J. K.; Mattoussi, H.; Simon, S. M. *Nature Medicine* **2004**, *10*, 993-998. [1](#)
- [12] Kreibig, U.; Genzel, L. *Surface Science* **1985**, *156*, 678-700. [1](#), [2.3](#), [2.3](#), [2.4](#), [3.4.1](#)
- [13] Alvarez, M. M.; Khoury, J. T.; Schaaff, T. G.; Shafigullin, M. N.; Vezmar, I.; Whetten, R. L. *Journal of Physical Chemistry B* **1997**, *101*, 3706-3712. [1](#), [2.3](#), [2.3](#), [2.3](#), [2.3](#), [2.4](#), [3.4.1](#), [4.1](#)

- [14] Demtröder, W. *Laser Spectroscopy*; 2003. [2.2](#), [2.2](#), [2.3](#), [2.2](#)
- [15] Lewis, G. N.; Kasha, M. *Journal of the American Chemical Society* **1945**, 67, 994. [2.2](#), [2.2](#), [3.4.2](#)
- [16] Strickler, S. J.; Berg, R. A. *Journal of Chemical Physics* **1962**, 37, 814-822. [2.2](#), [2.2](#), [2.2](#)
- [17] Craig, D.; Thirunamachandran, T. *Molecular Quantum Electrodynamics*; 1984. [2.2](#), [2.2](#), [3.4.1](#)
- [18] Moskovits, M. *Reviews of Modern Physics* **1985**, 57, 783-826. [2.3](#), [2.4](#), [4.3.2](#)
- [19] Lakowicz, J. R. *Analytical Biochemistry* **2005**, 337, 171-194. [2.3](#), [3.1](#), [4.3.2](#)
- [20] Link, S.; El-Sayed, M. A. *Annual Review of Physical Chemistry* **2003**, 54, 331-366. [2.3](#), [2.3](#), [2.3](#)
- [21] Link, S.; El-Sayed, M. A. *Journal of Physical Chemistry B* **1999**, 103, 8410-8426. [2.3](#), [4.1](#), [4.2.1](#)
- [22] Logunov, S. L.; Ahmadi, T. S.; El-Sayed, M. A.; Khoury, J. T.; Whetten, R. L. *Journal of Physical Chemistry B* **1997**, 101, 3713-3719. [2.3](#), [3.1](#), [5.3.2](#)
- [23] Mie, G. *Annalen Der Physik* **1908**, 25, 377-445. [2.3](#)
- [24] Johnson, P. B.; Christy, R. W. *Physical Review B* **1972**, 6, 4370-4379. [2.3](#), [2.3](#), [2.4](#), [3.4.1](#)
- [25] Hövel, H.; Fritz, S.; Hilger, A.; Kreibig, U.; Vollmer, M. *Physical Review B* **1993**, 48, 18178-18188. [2.3](#), [2.3](#), [2.3](#), [2.4](#), [3.4.1](#), [4.1](#)
- [26] Drexhage, K. H.; Fleck, M.; Kuhn, H.; Schafer, F. P.; Sperling, W. *Berichte Der Bunsen-Gesellschaft Fur Physikalische Chemie* **1966**, 70, 1179. [2.4](#)
- [27] Drexhage, K. H. *Journal of the Optical Society of America* **1970**, 60, 1541. [2.4](#)
- [28] Drexhage, K. H.; Kuhn, H.; Schafer, F. P. *Berichte Der Bunsen-Gesellschaft Fur Physikalische Chemie* **1968**, 72, 329. [2.4](#)
- [29] Chance, R.; Prock, A.; Silbey, R. *Advances in Chemical Physics* **1978**, 60, 1-65. [2.4](#), [3.1](#), [3.4.1](#), [4.3.4](#), [4.3.4](#), [6.1](#)
- [30] Gersten, J.; Nitzan, A. *Journal of Chemical Physics* **1981**, 75, 1139-1152. [2.4](#), [3.4.1](#), [3.4.1](#)
- [31] Chang, R. L. *Optics Communications* **2005**, 249, 329-337. [2.4](#), [3.4.1](#)
- [32] Ruppin, R. *Journal of Chemical Physics* **1982**, 76, 1681-1684. [2.4](#), [3.1](#), [3.4.1](#), [3.4.1](#)
- [33] Chew, H. *Journal of Chemical Physics* **1987**, 87, 1355-1360. [2.4](#), [3.4.1](#)

- [34] Leung, P. T. *Physical Review B* **1990**, 42, 7622-7625. [2.4](#), [3.4.1](#)
- [35] Persson, B. N. J.; Lang, N. D. *Physical Review B* **1982**, 26, 5409-5415. [2.4](#), [2.4](#), [3.1](#), [3.4.1](#), [4.3.4](#), [5.3.2](#), [6.1](#)
- [36] Dulkeith, E.; Morteani, A. C.; Niedereichholz, T.; Klar, T. A.; Feldmann, J.; Levi, S. A.; van Veggel, F. C. J. M.; Reinhoudt, D. N.; Moller, M.; Gittins, D. I. *Physical Review Letters* **2002**, 89, 203002-1. [2.4](#), [3.4.1](#)
- [37] Dulkeith, E.; Ringler, M.; Klar, T. A.; Feldmann, J.; Javier, A. M.; Parak, W. J. *Nano Letters* **2005**, 5, 585-589. [2.4](#), [3.1](#), [3.4.1](#), [3.4.2](#)
- [38] Persson, B. N. J. *Solid State Communications* **1978**, 27, 417-421. [2.4](#), [3.4.1](#)
- [39] Persson, B. N. J. *Surface Science* **1993**, 281, 153-162. [2.4](#), [3.4.1](#)
- [40] Alivisatos, A. P.; Waldeck, D. H.; Harris, C. B. *Journal of Chemical Physics* **1985**, 82, 541-547. [2.4](#), [3.4.1](#)
- [41] Lorrain, P.; Corson, D. *Electromagnetic Fields and Waves*; 1970. [2.4](#)
- [42] Yun, C. S.; Javier, A.; Jennings, T.; Fisher, M.; Hira, S.; Peterson, S.; Hopkins, B.; Reich, N. O.; Strouse, G. F. *Journal of the American Chemical Society* **2005**, 127, 3115-3119. [3.1](#), [5.1](#), [6.1](#)
- [43] Thomas, K. G.; Kamat, P. V. *Journal of the American Chemical Society* **2000**, 122, 2655-2656. [3.1](#)
- [44] Worthing, P. T.; Amos, R. M.; Barnes, W. L. *Physical Review A* **1999**, 59, 865-872. [3.1](#)
- [45] Kalkman, J.; Kuipers, L.; Polman, A.; Gersen, H. *Applied Physics Letters* **2005**, 86, 041113-1 - 041113-3. [3.1](#)
- [46] Weare, W. W.; Reed, S. M.; Warner, M. G.; Hutchison, J. E. *Journal of the American Chemical Society* **2000**, 122, 12890-12891. [3.2.1](#), [6.2](#)
- [47] Hays, J. B.; Magar, M. E.; Zimm, B. H. *Biopolymers* **1969**, 8, 531. [3.3](#)
- [48] Kuhn, H. *Journal of Chemical Physics* **1970**, 53, 101. [3.4.1](#), [4.3.4](#), [4.3.4](#), [6.1](#)
- [49] Gersten, J. I.; Nitzan, A. *Chemical Physics Letters* **1984**, 104, 31-37. [3.4.1](#), [4.3.3](#)
- [50] Gersten, J. I.; Nitzan, A. *Surface Science* **1985**, 158, 165-189. [3.4.1](#)
- [51] Turro, N. J. *Modern Molecular Photochemistry*; University Science Books 1991. [3.4.2](#)
- [52] Smith, B. A.; Zhang, J. Z.; Giebel, U.; Schmid, G. *Chemical Physics Letters* **1997**, 270, 139-144. [4.1](#), [5.3.2](#)
- [53] Slot, J.; Geuze, H. *European Journal of Cell Biology* **1985**, 38, 87-93. [4.2.1](#)

- [54] Jin, R. C.; Wu, G. S.; Li, Z.; Mirkin, C. A.; Schatz, G. C. *Journal of the American Chemical Society* **2003**, *125*, 1643-1654. [4.3](#)
- [55] Storhoff, J. J.; Lazarides, A. A.; Mucic, R. C.; Mirkin, C. A.; Letsinger, R. L.; Schatz, G. C. *Journal of the American Chemical Society* **2000**, *122*, 4640-4650. [4.3](#)
- [56] Georganopoulou, D. G.; Chang, L.; Nam, J. M.; Thaxton, C. S.; Mufson, E. J.; Klein, W. L.; Mirkin, C. A. *Proceedings of the National Academy of Sciences of the United States of America* **2005**, *102*, 2273-2276. [4.3](#)
- [57] Sonnichsen, C.; Reinhard, B. M.; Liphard, J.; Alivisatos, A. P. *Nature Biotechnology* **2005**, *23*, 741-745. [4.3](#)
- [58] Fleischmann, M.; Hendra, P. J.; Mcquillan, A. J. *Chemical Physics Letters* **1974**, *26*, 163-166. [4.3.2](#)
- [59] Krasser, W.; Kettler, U.; Bechthold, P. S. *Chemical Physics Letters* **1982**, *86*, 223-227. [4.3.2](#)
- [60] Talley, C. E.; Jackson, J. B.; Oubre, C.; Grady, N. K.; Hollars, C. W.; Lane, S. M.; Huser, T. R.; Nordlander, P.; Halas, N. J. *Nano Letters* **2005**, *5*, 1569-1574. [4.3.2](#)
- [61] Laurent, G.; Felidj, N.; Truong, S. L.; Aubard, J.; Levi, G.; Krenn, J. R.; Hohenau, A.; Leitner, A.; Aussenegg, F. R. *Nano Letters* **2005**, *5*, 253-258. [4.3.2](#)
- [62] Kho, K. W.; Shen, Z. X.; Zeng, H. C.; Soo, K. C.; Olivo, M. *Analytical Chemistry* **2005**, *77*, 7462-7471. [4.3.2](#)
- [63] Kim, K.; Lee, H. S. *Journal of Physical Chemistry B* **2005**, *109*, 18929-18934. [4.3.2](#)
- [64] Zhang, J.; Lakowicz, J. R. *Journal of Physical Chemistry B* **2005**, *109*, 8701-8706. [4.3.2](#)
- [65] Malicka, J.; Gryczynski, I.; Gryczynski, Z.; Lakowicz, J. R. *Analytical Biochemistry* **2003**, *315*, 57-66. [4.3.2](#)
- [66] Malicka, J.; Gryczynski, I.; Lakowicz, J. R. *Biopolymers* **2004**, *74*, 263-271. [4.3.2](#)
- [67] Aslan, K.; Gryczynski, I.; Malicka, J.; Matveeva, E.; Lakowicz, J. R.; Geddes, C. D. *Current Opinion in Biotechnology* **2005**, *16*, 55-62. [4.3.2](#)
- [68] Franzen, S.; Folmer, J. C. W.; Glomm, W. R.; O'Neal, R. *Journal of Physical Chemistry A* **2002**, *106*, 6533-6540. [4.3.2](#), [4.3.3](#)
- [69] Hao, E.; Schatz, G. C. *Journal of Chemical Physics* **2004**, *120*, 357-366. [4.3.3](#)
- [70] Gersten, J. I.; Nitzan, A. *Physical Review B* **1984**, *29*, 3852-3862. [4.3.3](#)
- [71] Michalet, X.; Pinaud, F. F.; Bentolila, L. A.; Tsay, J. M.; Doose, S.; Li, J. J.; Sundaresan, G.; Wu, A. M.; Gambhir, S. S.; Weiss, S. *Science* **2005**, *307*, 538-544. [5.1](#), [7.1](#)

- [72] Gao, X. H.; Yang, L. L.; Petros, J. A.; Marshal, F. F.; Simons, J. W.; Nie, S. M. *Current Opinion in Biotechnology* **2005**, *16*, 63-72. [5.1](#), [7.1](#)
- [73] Akerman, M. E.; Chan, W. C. W.; Laakkonen, P.; Bhatia, S. N.; Ruoslahti, E. *Proceedings of the National Academy of Sciences of the United States of America* **2002**, *99*, 12617-12621. [5.1](#), [7.1](#)
- [74] Su, X. L.; Li, Y. B. *Analytical Chemistry* **2004**, *76*, 4806-4810. [5.1](#)
- [75] Tran, P. T.; Goldman, E. R.; Anderson, G. P.; Mauro, J. M.; Mattoussi, H. *Physica Status Solidi B-Basic Research* **2002**, *229*, 427-432. [5.1](#)
- [76] Kim, J. H.; Morikis, D.; Ozkan, M. *Sensors and Actuators B-Chemical* **2004**, *102*, 315-319. [5.1](#)
- [77] Dubertret, B.; Calame, M.; Libchaber, A. J. *Nature Biotechnology* **2001**, *19*, 365-370. [5.1](#)
- [78] Stark, B. C.; Kole, R.; Bowman, E. J.; Altman, S. *Proceedings of the National Academy of Sciences of the United States of America* **1978**, *75*, 3717-3721. [5.1](#)
- [79] Cech, T. R. *Science* **1987**, *236*, 1532-1539. [5.1](#)
- [80] Grabowski, P. J.; Zaug, A. J.; Cech, T. R. *Cell* **1981**, *23*, 467-476. [5.1](#)
- [81] Bramlage, B.; Luzi, E.; Eckstein, F. *Trends in Biotechnology* **1998**, *16*, 434-438. [5.1](#)
- [82] Weizscker, F. v.; Wieland, S.; Kck, J.; Offensperger, W.; Offensperger, S.; Moradpour, D.; Blum, H. E. *Hepatology* **1997**, *26*, 251-255. [5.1](#)
- [83] Uhlenbeck, O. C. *RNA* **1995**, *1*, 4-6. [5.1](#)
- [84] Forster, A. C.; Symons, R. H. *Cell* **1987**, *49*, 211-220. [5.1](#)
- [85] Scott, W. G.; Murray, J. B.; Arnold, J. R. P.; Stoddard, B. L.; Klug, A. *Science* **1996**, *274*, 2065-2069. [5.1](#)
- [86] Scott, W. G.; Finch, J. T.; Grenfell, R.; Fogg, J.; Smith, T.; Gait, M. J.; Klug, A. *Journal of Molecular Biology* **1995**, *250*, 327-332. [5.1](#)
- [87] Bassi, G. S.; Murchie, A. I. H.; Walter, F.; Clegg, R. M.; Lilley, D. M. J. *Embo Journal* **1997**, *16*, 7481-7489. [5.1](#)
- [88] Perkins, T. A.; Wolf, D. E.; Goodchild, J. *Biochemistry* **1996**, *35*, 16370-16377. [5.1](#)
- [89] Tuschl, T.; Gohlke, C.; Jovin, T. M.; Westhof, E.; Eckstein, F. *Science* **1994**, *266*, 785-789. [5.1](#)
- [90] Bassi, G. S.; Mollegaard, N. E.; Murchie, A. I. H.; Lilley, D. M. J. *Biochemistry* **1999**, *38*, 3345-3354. [5.3.2](#), [5.3.2](#), [6.3.1](#)

- [91] Bassi, G. S.; Mollegaard, N. E.; Murchie, A. I. H.; Vonkitzing, E.; Lilley, D. M. J. *Nature Structural Biology* **1995**, 2, 45-55. [5.3.2](#), [6.3.1](#)
- [92] Penedo, J. C.; Wilson, T. J.; Jayasena, S. D.; Khvorova, A.; Lilley, D. M. J. *RNA* **2004**, 10, 880-888. [5.3.3](#)
- [93] Stage-Zimmermann, T. K.; Uhlenbeck, O. C. *RNA* **1998**, 4, 875-889. [5.3.3](#), [5.3.4](#), [5.3.4](#), [5.3.4](#)
- [94] Scott, W. G.; Klug, A. *Trends in Biochemical Sciences* **1996**, 21, 220-224. [5.3.3](#)
- [95] Sawata, S.; Komiyama, M.; Taira, K. *Journal of the American Chemical Society* **1995**, 117, 2357-2358. [5.3.3](#)
- [96] Dahm, S. C.; Derrick, W. B.; Uhlenbeck, O. C. *Biochemistry* **1993**, 32, 13040-13045. [5.3.3](#)
- [97] Fedor, M. J.; Uhlenbeck, O. C. *Biochemistry* **1992**, 31, 12042-12054. [5.3.4](#)
- [98] Corry, B.; Rigby, P.; Liu, Z. W.; Martinac, B. *Biophysical Journal* **2005**, 89, L49-L51. [6.1](#)
- [99] Wang, D.; Geva, E. *Journal of Physical Chemistry B* **2005**, 109, 1626-1634. [6.1](#)
- [100] Turner, B.; Melcher, S. E.; Wilson, T. J.; Norman, D. G.; Lilley, D. M. J. *Rna-a Publication of the Rna Society* **2005**, 11, 1192-1200. [6.1](#)
- [101] Wozniak, A. K.; Nottrott, S.; Kuhn-Holsken, E.; Schroder, G. F.; Grubmuller, H.; Luhrmann, R.; Seidel, C. A. M.; Oesterhelt, F. *Rna-a Publication of the Rna Society* **2005**, 11, 1545-1554. [6.1](#)
- [102] Lissandron, V.; Terrin, A.; Collini, M.; D'alfonso, L.; Chirico, G.; Pantano, S.; Zaccolo, M. *Journal of Molecular Biology* **2005**, 354, 546-555. [6.1](#)
- [103] Jennings, T.; Schlatterer, J.; Greenbaum, N.; Strouse, G. *Nano Letters* **2006**, 00, 00. [6.1](#)
- [104] Jennings, T.; Singh, M.; Strouse, G. *Journal of the American Chemical Society* **2006**, 00, 00. [6.1](#)
- [105] Cumberland, S. L.; Hanif, K. M.; Javier, A.; Khitrov, G. A.; Strouse, G. F.; Woessner, S. M.; Yun, C. S. *Chemistry of Materials* **2002**, 14, 1576-1584. [7.2.1](#)
- [106] Dance, I. G.; Choy, A.; Scudder, M. L. *Journal of the American Chemical Society* **1984**, 106, 6285-6295. [7.2.1](#)
- [107] Li, J. J.; Wang, Y. A.; Guo, W. Z.; Keay, J. C.; Mishima, T. D.; Johnson, M. B.; Peng, X. G. *Journal of the American Chemical Society* **2003**, 125, 12567-12575. [7.2.2](#)

- [108] Zhong, X. H.; Feng, Y. Y.; Knoll, W.; Han, M. Y. *Journal of the American Chemical Society* **2003**, *125*, 13559-13563. [7.3.1](#)
- [109] Zhong, X. H.; Han, M. Y.; Dong, Z. L.; White, T. J.; Knoll, W. *Journal of the American Chemical Society* **2003**, *125*, 8589-8594. [7.3.1](#)
- [110] Hines, M. A.; Guyot-Sionnest, P. *Journal of Physical Chemistry* **1996**, *100*, 468-471. [7.3.1](#)
- [111] Lide, D. R. *CRC Handbook of Chemistry and Physics*; CRC Press: Boca Raton, 82 ed.; 2002. [7.3.2](#)
- [112] Chen, X. B.; Lou, Y. B.; Samia, A. C.; Burda, C. *Nano Letters* **2003**, *3*, 799-803. [7.3.2](#), [7.3.3](#)
- [113] Klimov, V. I.; Mikhailovsky, A. A.; Xu, S.; Malko, A.; Hollingsworth, J. A.; Leatherdale, C. A.; Eisler, H. J.; Bawendi, M. G. *Science* **2000**, *290*, 314-317. [7.3.3](#)
- [114] Cherniavskaya, O.; Chen, L. W.; Islam, M. A.; Brus, L. *Nano Letters* **2003**, *3*, 497-501. [7.3.3](#)
- [115] Javier, A.; Magana, D.; Jennings, T.; Strouse, G. F. *Applied Physics Letters* **2003**, *83*, 1423-1425. [7.3.3](#)
- [116] Empedocles, S. A.; Bawendi, M. G. *Science* **1997**, *278*, 2114-2117. [7.3.3](#)
- [117] Empedocles, S. A.; Neuhauser, R.; Shimizu, K.; Bawendi, M. G. *Advanced Materials* **1999**, *11*, 1243-1256. [7.3.3](#)
- [118] Barnes, M. D.; Krstic, P. S.; Kumar, P.; Mehta, A.; Wells, J. C. *Physical Review B* **2005**, *71*, 241303. [7.3.3](#)

BIOGRAPHICAL SKETCH

Education

- Florida State University, Tallahassee, Florida, Ph.D. in Physical Chemistry, January 2006. Thesis: *Nanomaterials: Synthesis, Characterization, and their Bio-Integration*.
- University of California, Santa Barbara, Ph.D. Candidate Physical Materials Chemistry,¹ July 2001 - December 2004.
- Pepperdine University, Malibu, California, B.S. in Chemistry, May, 2001.

Appointments

- Graduate Researcher - Florida State University2004-2006
- Graduate Researcher - University of California, Santa Barbara.....2001-2004
- Aerospace Corporation, Consultant (Nanomaterials).....2001-2002
- Aerospace Corporation, Research Scientist (Bio-Nano Technology).....1998-2001

Skills

- Computers
 - *Mathematica* Programming
 - Graphics (Flash, Dreamweaver, Illustrator, Photoshop, InDesign, Premiere Pro)
 - L^AT_EX 2_ε
- Spectroscopy

¹Faculty advisor transferred to Florida State University from UCSB in 2004

- Absorption
- Photoluminescence / Photoluminescence Excitation
- Picosecond Transient Photoluminescence
- Dye-Laser Alignment
- Synthesis
 - Quantum Dot Synthesis (CdSe, InP, CdS, ZnSe)
 - Metal Nanoparticle Synthesis (Au, Co)
 - DNA / RNA Synthesis - specialty base labeling
- Bio-Nano Conjugation
 - Nanoparticle DNA/RNA conjugation
 - Nanoparticle Protein conjugation
- Transmission Electron Microscopy
 - Nanomaterials
 - Bio-Nanomaterial Conjugates

Publications

1. “*NSET Molecular Beacon Analysis of Hammerhead RNA Substrate Binding and Catalysis*” T.L. Jennings, J.C. Schlatterer, N.L. Greenbaum, G.F. Strouse, submitted to *Nano Letters*, 2005.
2. “*Fluorescent Lifetime Quenching Near $d=1.5$ nm Gold Nanoparticles: Probing NSET Validity*” T.L. Jennings, M.P. Singh, G.F. Strouse, submitted to *JACS* 2005.
3. “*Hammerhead Structural Triangulation using Small Gold Nanoparticles*” T.L. Jennings, M.P. Singh, J.C. Schlatterer, N.L. Greenbaum, G.F. Strouse, *In Preparation*.
4. “*Nanometal Surface Energy Transfer in Optical Rulers, Breaking the FRET Barrier*” C.S. Yun, A. Javier, T. Jennings, M. Fisher, S. Hira, S. Peterson, B. Hopkins, N.O. Reich, and G.F. Strouse, *J. Am. Chem. Soc.*, **127**(9), 3115-3119, (2005).
5. “*Compressive and Tensile Stress in Colloidal CdSe Semiconductor Quantum Dots*” R.W. Meulenberg, T. Jennings, G.F. Strouse, *Phys. Rev. B.*, **70**, 235311, (2004).

6. "Fluorescence and Atomic Force Microscopy Studies of Polyelectrolyte, CdSe Nanoparticle Heterostructures" A.D. Ranasinghe, G.M. Lowman, E.L. Orazem, M.A. Summers, J.A. Gerbec, T.L. Jennings, G.F. Strouse, S.K. Buratto, *Polymeric Materials Science and Engineering*, **90**, 443, (2004).
7. "Nanosecond Exciton Recombination Dynamics in Colloidal CdSe Quantum Dots Under Ambient Conditions" A. Javier, D. Magana, T. Jennings, G.F. Strouse, *Applied Physics Letters*, **83**, 1423, (2003).
8. "Development of Quantum Dot Reporters for Immunoassay Applications" D.M. Speckman, T.L. Jennings, S.D. LaLumondiere, S.C. Moss, *MRS Proceedings*, **676**, Y3.6.1-Y3.6.6. (2002).
9. "Quenching Phenomena in Water-Soluble CdSe/ZnS Quantum Dots" D.M. Speckman, T.L. Jennings, S.D. LaLumondiere, S.C. Moss, *Materials Research Society Symposium Proceedings*, **704**, 269-274, (2002).
10. "Biodetection Using Fluorescent Quantum Dots" D.M. Speckman, T.L. Jennings, S.D. LaLumondiere, C.M. Klimcak, S.C. Moss, G.L. Loper, S.M. Beck, *Proceedings of SPIE*, **4745**, 136-143, (2002).

Meeting Presentations

1. Oral Presentation: "NanoMaterials: Hammerheading a New Frontier" T.L. Jennings, J.C. Schlatterer, N.L. Greenbaum, G.F. Strouse, MRS Fall Meeting, Boston, Nov. 28 - Dec. 2, 2005.
2. Poster Presentation: "NanoMaterials: Hammerheading a New Frontier" T.L. Jennings, J.C. Schlatterer, N.L. Greenbaum, G.F. Strouse, SPIE Conference Paper 6009-24, Biomedical Optics, Boston, Oct. 2005.
3. Poster Presentation: "NanoMaterials: Hammerheading a New Frontier" T.L. Jennings, J.C. Schlatterer, N.L. Greenbaum, G.F. Strouse, American Chemical Society National Meeting, Paper # 899581, August, 2005.

4. Oral Presentation: “*Bio-Nanomaterials as Molecular Rulers: Application of Nanoparticles for Distance Measurements in Proteo-Nucleic Systems*” T.L. Jennings, G.F. Strouse, N.O. Reich, S. Peterson, American Chemical Society National Meeting Paper 759-INOR, August, 2004.
5. Poster: “*Transient Photophysical Comparison of Core and Core-Shell Quantum Dot Materials*” T.L. Jennings, A. Javier, D. Neuman, G.F. Strouse, Graduate Seminar, UCSB, April 2003.
6. Oral Presentation: “*Photophysical Comparison of Core and Core-Shell Quantum Dot Materials*” T.L. Jennings, A. Javier, G.F. Strouse, Southern California Inorganic Photochemistry Conference (SCIP), Catalina Island, CA, September 2002.
7. Oral Presentation: “*Development of Miniature Multipathogen Biosensors Based on Core/Shell Nanocrystals*” D.M. Speckman, T.L. Jennings, C.M. Klimcak, S.D. LaLumondiere, S.C. Moss, S.M. Beck, G.L. Loper, Gordon Research Conference on Clusters, Nanocrystals, and Nanostructures, New London, CT, July 2001.
8. Oral Presentation: “*Development of New Fluorescent Labels for Miniature Biosensor Systems*” D.M. Speckman, T.L. Jennings, S.D. LaLumondiere, C.M. Klimcak, S.C. Moss, G.L. Loper, S.M. Beck, MASINT Biological Warfare Science and Technology Symposium, Ft. Walton Beach, FL, February 2001.

Affiliations

- SPIE - The International Society for Optical Engineering
- MRS - Materials Research Society
- ACS - The American Chemical Society